

# Cosmological applications of gravitational lensing

## Dissertation

zur Erlangung des akademischen Grades  
Doktor der Naturwissenschaften (Dr. rer. nat.)  
in der Wissenschaftsdisziplin Astrophysik

eingereicht an der  
Mathematisch-Naturwissenschaftlichen Fakultät  
der Universität Potsdam

von

Robert W. Schmidt

geboren am 28. April 1972  
in London, Großbritannien

Potsdam, im März 2000



# Abstract

In this thesis we use the gravitational lensing effect as a tool to tackle two rather different cosmological topics: the nature of the dark matter in galaxy halos, and the rotation of the universe. Firstly, we study the microlensing effect in the gravitational lens systems Q0957+561 and Q2237+0305. In these systems the light from the quasar shines directly through the lensing galaxy. Due to the relative motion of the quasar, the lensing galaxy, and the observer compact objects in the galaxy or galaxy halo cause brightness fluctuations of the light from the background quasar. We compare light curve data from a monitoring program of the double quasar Q0957+561 at the 3.5 m telescope at Apache Point Observatory from 1995 to 1998 (Colley, Kundić & Turner [34]) with numerical simulations to test whether the halo of the lensing galaxy consists of massive compact objects (MACHOs). This test was first proposed by Gott [62]. We can exclude MACHO masses from  $10^{-6} M_{\odot}$  up to  $10^{-2} M_{\odot}$  for quasar sizes of less than  $3 \times 10^{14} h_{60}^{-1/2}$  cm if the MACHOs make up at least 50% of the dark halo. Secondly, we present new light curve data for the gravitationally lensed quadruple quasar Q2237+0305 taken at the 3.5 m telescope at Apache Point Observatory from June 1995 to January 1998. Although the images were taken under variable, often poor seeing conditions and with coarse pixel sampling, photometry is possible for the two brighter quasar images A and B with the help from HST observations. We find independent evidence for a brightness peak in image A of 0.4 to 0.5 mag with a duration of at least 100 days, which indicates that microlensing has taken place in the lensing galaxy. Finally, we use the weak gravitational lensing effect to put limits on a class of Gödel-type rotating cosmologies described by Korotky & Obukhov [100]. In weak lensing studies the shapes of thousands of background galaxies are measured and averaged to reveal coherent gravitational distortions of the galaxy shapes by foreground matter distributions, or by the large-scale structure of space-time itself. We calculate the predicted shear as a function of redshift in Gödel-type rotating cosmologies and compare this to the upper limit on cosmic shear  $\gamma_{\text{limit}} \approx 0.04$  from weak lensing studies. We find that Gödel-type models cannot have larger rotations than  $\omega \approx H_0 = 6.1 \times 10^{-11} h_{60} \text{ year}^{-1}$  if this shear limit is valid for the whole sky.



# Abstract

In dieser Arbeit benutze ich den Gravitationslinseneffekt als ein Werkzeug, um zwei recht unterschiedliche kosmologische Fragestellungen zu bearbeiten: die Natur der dunklen Materie in Galaxienhalos und die Rotation des Universums. Zuerst untersuche ich den Mikrolinseneffekt in den Gravitationslinsensystemen Q0957+561 und Q2237+0305. In diesen Systemen scheint das Licht eines Quasars durch die Linsengalaxie hindurch. Aufgrund der Relativbewegung zwischen Quasar, Linsengalaxie und Beobachter verursachen kompakte Objekte innerhalb der Galaxie oder dem Galaxienhalo Helligkeitsfluktuationen des Hintergrundquasars. Ich vergleiche die am 3.5m Teleskop des Apache Point Observatory zwischen 1995 und 1998 gewonnene Lichtkurve des Doppelquasars Q0957+561 (Colley, Kundić & Turner [34]) mit numerischen Simulationen, um zu untersuchen, ob der Halo der Linsengalaxie aus massiven kompakten Objekten (MACHOs) besteht. Dieser Test wurde zuerst von Gott [62] vorgeschlagen. Ich kann MACHO-Massen von  $10^{-6} M_{\odot}$  bis zu  $10^{-2} M_{\odot}$  ausschließen, sofern der Quasar kleiner ist als  $3 \times 10^{14} h_{60}^{-1/2}$  cm und MACHOs mehr als 50% des dunklen Halos ausmachen. Im zweiten Teil der Arbeit stelle ich neue Beobachtungsdaten für den Vierfachquasar Q2237+0305 vor, die am 3.5m Teleskop des Apache Point Observatory zwischen Juni 1995 und Januar 1998 gewonnen wurden. Obwohl die Daten bei veränderlichen, oft schlechten Seeing Bedingungen und grober Pixelauflösung aufgenommen wurden, ist die Photometrie der beiden helleren Quasarbilder A und B mit Hilfe von HST-Beobachtungen möglich. Ich finde ein Helligkeitsmaximum in Bild A mit einer Amplitude von 0.4 bis 0.5 mag und einer Dauer von wenigstens 100 Tagen. Dies zeigt, daß in der Linsengalaxie der Mikrolinseneffekt stattgefunden hat. Im abschließenden Teil der Arbeit benutze ich dann den schwachen Gravitationslinseneffekt, um Grenzen für eine Klasse von rotierenden Kosmologien vom Gödel-Typ zu ermitteln, die von Korotky & Obukhov [100] beschrieben wurde. In Studien des schwachen Linseneffektes werden die Formen von tausenden von Hintergrundgalaxien vermessen und gemittelt. Dabei werden kohärente Verzerrungen der Galaxienformen gemessen, die von Massenverteilungen im Vordergrund oder von der großräumigen Struktur der Raumzeit selbst verursacht werden. Ich berechne die vorhergesagte Scherung als Funktion der Rotverschiebung in rotierenden Kosmologien vom Gödel-Typ und vergleiche diese mit der oberen Grenze für die kosmische Scherung  $\gamma_{\text{limit}} \approx 0.04$ , die in Studien des schwachen Linseneffektes gewonnen wurde. Dieser Vergleich zeigt, daß Modelle vom Gödel-Typ keine größeren Rotationen als  $\omega \approx H_0 = 6.1 \times 10^{-11} h_{60} \text{ year}^{-1}$  haben können, wenn die Grenze für die kosmische Scherung für den ganzen Himmel gilt.



# Contents

<b>1</b>	<b>Cosmology and dark matter</b>	<b>1</b>
1.1	Introduction . . . . .	1
1.2	The standard cosmological model . . . . .	2
1.3	Dark matter . . . . .	3
<b>2</b>	<b>Gravitational lensing</b>	<b>6</b>
2.1	The deflection angle . . . . .	6
2.2	Observations . . . . .	8
2.2.1	Strong and weak lensing . . . . .	8
2.2.2	Microlensing . . . . .	9
2.3	Distances and redshifts in cosmology . . . . .	10
2.4	Single plane lensing . . . . .	13
2.4.1	Lens equation . . . . .	13
2.4.2	Magnification . . . . .	15
2.4.3	The point mass lens . . . . .	16
2.4.4	Compact objects in the light path . . . . .	17
2.4.5	Critical lines and caustics . . . . .	17
2.5	Lensing in inhomogeneous or anisotropic universes . . . . .	18
<b>3</b>	<b>Limits on MACHOs from microlensing in Q0957+561</b>	<b>21</b>
3.1	Halo dark matter = MACHOs? . . . . .	21
3.2	MACHOs in other galaxies . . . . .	22
3.3	Limits from microlensing . . . . .	23
3.3.1	Q2237+0305: The Einstein cross . . . . .	23
3.3.2	Q0957+561 . . . . .	23
3.4	Q0957+561: Mass models and time-delay . . . . .	24
3.5	Observations and simulations . . . . .	26
3.5.1	The Apache Point Observatory Q0957+561 light curve . . . . .	27
3.5.2	Simulating microlensing light curves . . . . .	30
3.5.3	MACHO mass and quasar size . . . . .	32
3.5.4	Light curve logistics . . . . .	34
3.6	Results . . . . .	35
3.7	Discussion and conclusion . . . . .	41

<b>4</b>	<b>Independent evidence for Microlensing in Q2237+0305</b>	<b>42</b>
4.1	Microlensing in Q2237+0305 . . . . .	42
4.2	Q2237+0305 observations at Apache Point Observatory . . . . .	44
4.3	Data reduction pipeline . . . . .	48
4.4	Results, interpretation and prospects . . . . .	56
<b>5</b>	<b>Limits on universal rotation from weak lensing</b>	<b>60</b>
5.1	Birefringence of the polarization of radio sources . . . . .	60
5.2	Cosmic rotation . . . . .	61
5.3	Limits on cosmic rotation . . . . .	62
5.4	Weak lensing and cosmic shear . . . . .	63
5.5	Lensing limits on cosmic shear . . . . .	64
5.6	Rotating universes without CMB anisotropy . . . . .	66
5.7	Method . . . . .	68
5.8	Affine parameter-redshift relation . . . . .	69
5.9	Parameter space . . . . .	71
5.10	Model zoo and results . . . . .	73
5.11	Conclusion . . . . .	79
<b>6</b>	<b>Summary and Outlook</b>	<b>81</b>



# Chapter 1

## Cosmology and dark matter

### 1.1 Introduction

Two rather different questions have lead to this thesis: 1. Are galaxy halos made up of massive, compact objects? 2. Is the universe rotating? In fact, the questions are so different that it is difficult to discuss them in a single breath. But it is remarkable that they can be tackled with the same tool: gravitational lensing.

“Gravitational lensing” is a term that is used for the deflection of light by massive bodies and the associated phenomena. Light deflection was first detected when the positions of stars near the solar limb during a solar eclipse in 1919 were observed to have slightly shifted as compared to their positions on the night sky. This measurement provided strong evidence in support of Albert Einstein’s theory of general relativity. Even before more examples became known, the gravitational lensing effect inspired theorists as to the potential it would have for astrophysics and especially cosmology<sup>1</sup>. Since the first gravitational lens with multiple images was found in 1979 by Walsh, Carswell & Weymann [189], the subject has boomed enormously. Gravitational lensing has become a versatile tool for cosmology and astrophysics in general.

This thesis aims at exploiting this potential in two respects: Firstly, in chapters 3 and 4 we will analyze the light from distant quasars that passes through foreground galaxies. The quasar light is used as a “scanning beam” to test whether any compact objects can be found in the galaxies by their lensing, or magnifying, effect. Secondly, we use the shapes of distant galaxies as scanning beams. Recent studies have shown that their shapes are preserved with only very little distortion on the way to us. A curious class of cosmological models where the universe rotates around the observer that are generalizations of a model that was first developed by Kurt Gödel can be tested by such a direct analysis of the distortion of light beams. This will be done in chapter 5.

Before we embark on the detailed studies outlined here, the remainder of this chapter will be dedicated to introducing the standard cosmological models, with a short introduction of the main players – dark matter and cosmological constant. In chapter 2 we describe the formalism of gravitational lensing.

---

<sup>1</sup>This story can be read in the book by Schneider, Ehlers & Falco [170, pages 3-9].

## 1.2 The standard cosmological model<sup>2</sup>

The space-time of our universe is governed by the field equations of general relativity. If the universe is homogeneous and isotropic it has to have a time-dependent but spatially uniform curvature and the field equations dictate the dynamics.

In the standard cosmological model, the universe began about 15 billion years ago and it has been expanding since. The curvature of the universe depends on the dimensionless density parameter

$$\Omega = \frac{\rho}{\rho_{\text{crit}}} \quad (1.1)$$

that describes the density of the universe  $\rho$  in terms of a critical density

$$\rho_{\text{crit}} = \frac{3 H_0^2}{8\pi G} = 6.8 \times 10^{-30} \text{ g cm}^{-3} h_{60}^2. \quad (1.2)$$

A universe with zero curvature has the critical density. In this expression,  $G$  is the gravitational constant, and  $H_0$  is the so-called Hubble constant. The Hubble constant is a measure for the current expansion rate of the universe. Its inverse is proportional to the age  $t_0$  of the universe

$$t_0 \sim H_0^{-1}. \quad (1.3)$$

All distances in the universe scale with  $c/H_0$ , where  $c$  is the speed of light, so that the Hubble constant is a measure for the size of the universe. In this thesis, all quantities will be given in terms of a Hubble constant of  $60 \text{ km s}^{-1} \text{ Mpc}^{-1}$ , scaled with  $h_{60} = H_0/60 \text{ km s}^{-1} \text{ Mpc}^{-1}$ . This value emerges from studies of the gravitational lens effect [105] (with an uncertainty of at least 10%), and is close to values derived from Hubble Space Telescope observations of Cepheids in the Virgo galaxy cluster [119].

Positive curvature ( $\Omega > 1$ ) corresponds to a closed universe that will eventually contract again. Negative curvature ( $\Omega < 1$ ) corresponds to an open universe that will always expand. In addition to the density in matter,  $\Omega_m$ , a term called the cosmological constant  $\Omega_\Lambda$  can be added to the field equations so that  $\Omega = \Omega_m + \Omega_\Lambda$ .  $\Omega_\Lambda$  corresponds to a vacuum-energy with the peculiar equation of state  $p = -\rho c^2$ , where  $p$  is the pressure,  $\rho$  the density and  $c$  the speed of light. In general, the matter and vacuum energy densities vary with time, but a flat universe with  $\Omega = 1$  stays flat. In the following  $\Omega_m$  and  $\Omega_\Lambda$  refer to the current values. Whenever we use definite values for these quantities in this thesis, we use  $\Omega = 1$  and  $\Lambda = 0$ .

In the standard cosmological picture, the universe expanded from a hot and dense state where most of the mass was contained in radiation in thermal equilibrium, with an equation of state  $p = \rho c^2/3$ . With the expansion, the universe cooled down. When the energy density in relativistic particles dropped below the density of the rest masses of hydrogen and helium, the universe became matter-dominated with an equation of state  $p \ll \rho c^2$  (a universe with this equation of state is sometimes referred as a ‘‘dust’’-universe, although the actual matter content of the

---

<sup>2</sup>This section is a brief sketch of the basics of cosmology. It is intended to introduce the fundamental notions and definitions, but not as a thorough introduction. For this purpose, see for example, Berry [15] or Peebles [134].

universe, especially at the early epochs, is not dust). After the temperature of the expanding universe had dropped to about 3000-4000 K, the free electrons were captured by atoms and the universe became abruptly optically thin. The remnant photons from the hot early phase continued to cool while the universe expanded. This radiation remnant of the hot early phase of the universe was discovered as a microwave background radiation in the 60s [134, page 131] with a temperature of 2.7 K. This radiation is now known as the cosmic microwave background (CMB). It is isotropic to such a high degree that the COBE satellite only detected temperature anisotropies of one part in  $10^5$  on a scale of  $\approx 10$  degrees [179].

In recent analyses of the CMB anisotropy on scales of a degree and below, structures have been detected that are interpreted as the results of acoustic oscillations in the photon-baryon liquid in the early universe. Since the maximum size of these oscillations is constrained by the sound speed in the medium times the age of the universe at the epoch of the decoupling of radiation from matter (“sound horizon”) [77], it is possible to constrain  $\Omega$  with these observations to be definitely greater than 0.3, and not unlikely close to one [66, 80, 177, 184].

The cosmological constant acts as an accelerating or decelerating term in the field equations, so that it has a stretching or compressing effect on large distances in the universe, as compared to the  $\Omega_\Lambda = 0$  case. It seems that this effect has also recently been detected by two teams that have used high-redshift supernovae and a sophisticated method [152] to determine the absolute magnitude, and thus the distance, of these objects from the supernova light curves. These groups find that their data are inconsistent with the case of no cosmological constant. They find a relation between  $\Omega_m$  and  $\Omega_\Lambda$  that predicts for  $\Omega = 1$  that the universe is accelerating with  $\Omega_\Lambda \approx 0.7 \pm 0.1$  [56, 137] ( $1 \sigma$  error bar).

However, so far the only evidence for  $\Omega_\Lambda$  that seems to convince a large majority of the community comes from the supernovae, so that a check is necessary. Limits from gravitational lensing, for example, constrain  $\Omega_\Lambda$  in a flat universe to be smaller than 0.66 [114, 97] (at  $3 \sigma$ ). Bartelmann et al. [12] even concluded that  $\Omega_\Lambda = 0$  from the frequency of gravitationally lensed arcs in galaxy clusters, although these constraints can be weakened if larger error bars are assigned to the observed arc counts (Bartelmann 1998, priv. comm.).

Numerical simulations of structure formation exclude a universe with  $\Omega_m = 1$  and no cosmological constant: it was found, for example, that galaxy clusters would be much more abundant than observed [151, page 18], the velocity dispersion of galaxies around the local group would be factor of three too high [16], and we would expect many more wide-separation gravitational lenses than observed [191]. Fan et al. [50] directly constrain  $\Omega_m$  from the evolution of the abundance of galaxy clusters and find  $\Omega_m = 0.3 \pm 0.1$  ( $1 \sigma$ ).

## 1.3 Dark matter

From the last section, it seems that we have evidence that some 30 percent of the universe is made up from matter. It is now natural to ask what kind of matter this is.

In the 30s, Zwicky [224] and Smith [178] measured the velocities of galaxies in the Coma and Virgo clusters of galaxies. By estimating the mass necessary to gravitationally bind the galaxies given their velocities, they found that about two orders of magnitude more mass was needed than

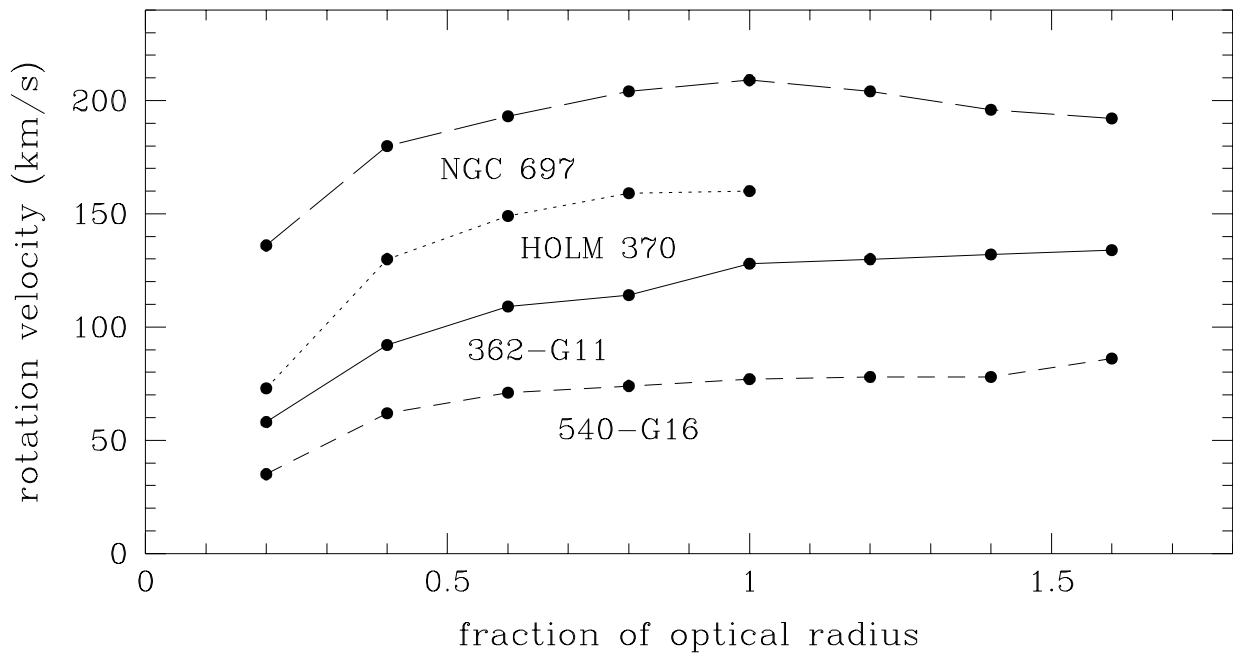


Figure 1.1: Galaxy rotation curves. Rotation curves from the collection by Persic & Salucci [138] are shown for the galaxies NGC 697 (long dashed), Holm 370 (dotted), 362-G11 (solid) and 540-G16 (short dashed). The velocities have been determined at the positions of the data points using the  $H\alpha$  line. We have connected the points for visualization. The curves are normalized to the optical radius of the galaxies.

there was luminous mass in the galaxies. The missing mass is now known as “dark matter”. Between 10 and 30 percent [25] of this matter, depending on the cluster at hand, was later found to be hot plasma that is dense enough to be detected by its thermal X-ray Bremsstrahlung. The total masses of the galaxy clusters determined under the assumption of hydrostatic equilibrium and by measuring the temperature of the cluster gas from its X-ray spectrum [144] also indicated that the clusters contain more mass than their galaxy and gas content [25]. The case for dark matter has become rather solid with the discovery of giant arcs and weak distortions of background galaxies in several galaxy clusters, which betray the presence of the dark matter by its gravitational lensing effect [115, 13].

A different kind of evidence for dark matter can be found in the rotation curves of galaxies. In galaxy rotation curves the rotational velocity is measured as a function of the separation from the galaxy centre. It was known since the 70s that rotation curves remain flat even beyond the visible matter [155, 156]. As an example in Fig. 1.1 four rotation curves from Persic & Salucci [138] are shown. The curves were obtained from spectra of the galaxies by measuring the wavelength of the  $H\alpha$ -line as a function of the separation from the galaxy centre. The rotation curves indicate that the mass in galaxies is more spread out than the light because rotation curves deduced from the luminous matter would drop much quicker. We can illustrate this in the simplest case of

a spherically symmetric mass distribution. The density  $\rho(r)$  as a function of the radius  $r$  can be determined from the orbital velocity  $v(r)$  around the mass  $M(r) = v^2 r / G$ , where  $G$  is the gravitational constant, enclosed in the sphere with radius  $r$ :

$$\rho(r) = \frac{1}{4\pi r^2} \frac{\partial}{\partial r} M(r) = \frac{v^2}{4\pi G r^2}. \quad (1.4)$$

For a constant velocity  $v$ , the density drops as  $1/r^2$ . The observed light in galaxies drops much faster. An often used model for disks of spiral galaxies is an exponential profile [134, page 46]. As a solution for this puzzle, Ostriker et al. [129] and Einasto et al. [45] suggested that galaxies are surrounded by large halos of dark matter that dominate the total mass of the galaxies.

Besides leading to rotation curves that look similar to the observed ones, dark galaxy halos provide an explanation for another puzzle that emerged from numerical simulations of rotating self-gravitating disks: In disks with a flat rotation curve where the random stellar motions are small compared to the circular motion, a bar-like instability forms and reshapes the disk with a much higher velocity dispersion in only a few rotations of the disk (for example [75], [17, pp. 372]). While this bar instability provided a beautiful explanation for the observed phenomenon of bars in spiral galaxies, the same instability made it difficult to explain the bare existence of many spiral galaxies because their random stellar motions are small. Ostriker & Peebles [128] then found that it was possible to stabilize such a disk by adding surrounding halos of dark matter.

A large number of possible candidates for the dark matter has been put forward in recent years, reviews are given, for example, by Bahcall [9] and Raffelt [142]). The candidates can broadly be divided into “elementary particle” candidates (such as neutrinos, axions or weakly interacting massive particles (WIMPs)) and “astrophysical” candidates (such as black holes, brown dwarfs, “Jupiters”, comets). Not much progress has been made to date in identifying the elusive dark matter despite major efforts in many directions. In fact, a new branch of physics established itself – “astro-particle physics” – that is dedicated to the solution of the dark matter problem.

In chapters 3 and 4 we will study two distant quasars that shine through a foreground galaxy with a known high surface density of matter at the positions of the quasars. By analyzing the long-term behaviour of the flux from the quasars, we will obtain limits on the masses of objects in the galaxy halos since they would gravitationally magnify the light from the quasars. Firstly, however, we introduce the necessary concepts of the gravitational lensing effect.

# Chapter 2

## Gravitational lensing

### 2.1 The deflection angle

A remarkable consequence of Einstein's theory of general relativity is that light rays are deflected by gravity. In 1915 Einstein [47] calculated the deflection angle  $\hat{\alpha}$  of a light ray with an impact parameter  $R$  by a body with mass  $M$  from his field equations and obtained

$$\hat{\alpha} = \frac{4GM}{c^2 R}. \quad (2.1)$$

It had already been suspected before that light could be deflected by gravity, but under different assumptions. It was known from the results of free fall experiments, the most influential being the ones by Galileo Galilei [54], that all bodies fall at the same speed when released from rest. In 1804 Soldner [180] treated a light ray as a particle and predicted that light would be deflected by masses by half the value given by eq. (2.1). The Soldner angle was rederived by Einstein in 1911 [46] by realising that the pace of clocks depends on the position in a gravitational potential and by deriving an effective refractive index for the space around masses from this.<sup>1</sup> The true deflection angle is twice the Soldner angle because in general relativity space is also curved.

Einstein's formula (2.1) for the deflection angle predicts that a light ray which tangentially grazes the surface of the Sun is deflected by  $1.7''$ . This result was confirmed in 1919 when the apparent angular shift of stars close to the limb of the sun was measured during a total solar eclipse [38]. This was immediately regarded as compelling evidence in support of general relativity and it was the first observed example of "gravitational lensing". This deflection angle has since been repeatedly confirmed with high-precision VLBI measurements in the radio regime, see for example [154].

In Fig. 2.1, the light deflection due to lens galaxy between an observer and a light source is illustrated. In the frame of the observer, the wavefront propagates slower in the gravitational potential of the galaxy than outside. The central part lags behind, and the wavefronts on both

---

<sup>1</sup>Which half of (2.1) did Einstein derive? Liebscher (1997, priv. comm.) brought to my attention that Einstein's calculation is mathematically identical to using the Hamilton-Jacobi formalism and Newton's theory of gravitation. One could say that using a new interpretation, Einstein rederived in 1911 "the same" half of (2.1) as Soldner.

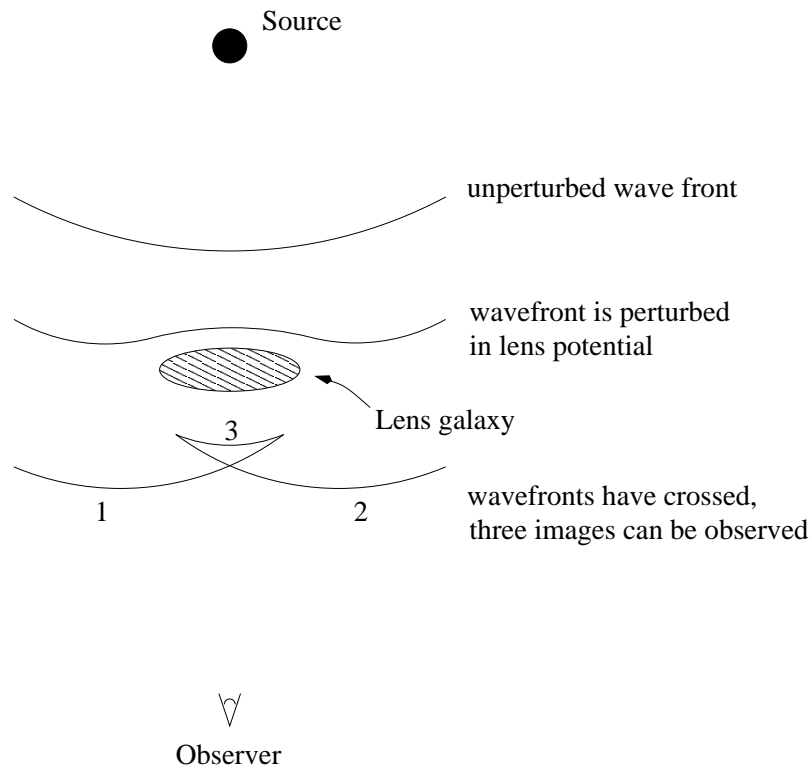


Figure 2.1: Wavefront propagation in a galaxy potential.

sides of the galaxy may even cross if the potential well of the galaxy is massive enough. If the observer is close enough to the optical axis defined by source and galaxy centre, three images of the same source may be seen: two images from the wavefronts on either side, and a very weak (highly demagnified) image in the middle coming from a wavefront that developed when the other two parts of the wavefront crossed. Exactly on the optical axis, the source would even appear as a so-called Einstein ring. The gravitational potential of the galaxy acts as a medium with varying refractive index. The observer would see the three images at positions on the sky that are shifted with respect to the original source position without a lens. The light deflection from the straight path is given by Einstein's formula (2.1). In observed lensing systems, the galaxy is normally not circularly symmetric. In this case, five different wavefronts can arrive at an observer close to the optical axis, of which four images are observed while the fifth is usually too faint to be detected.

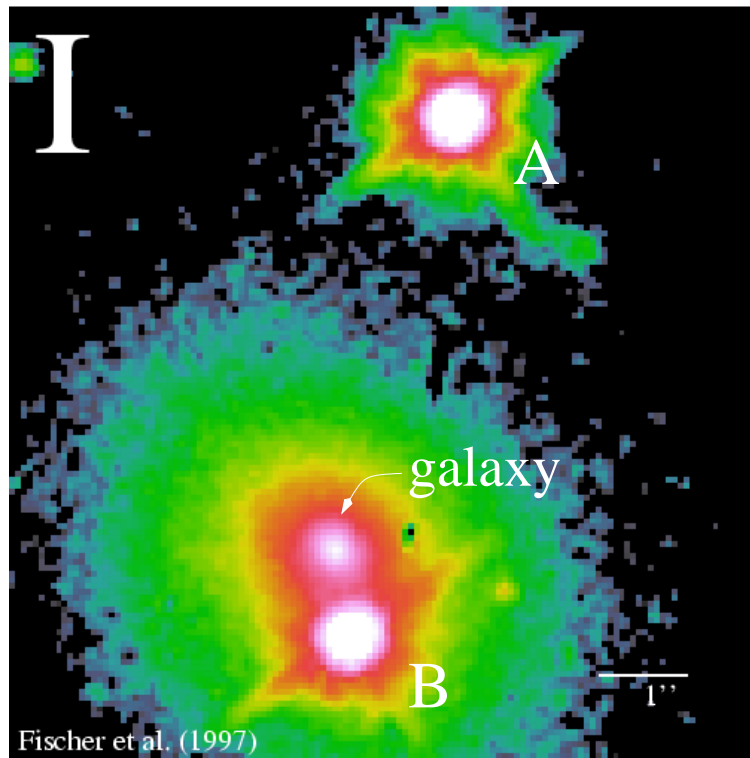


Figure 2.2: The gravitational lens system Q0957+561 as observed with Hubble Space Telescope in the *I*-band. The two quasar images A and B are seen through the lensing galaxy. This picture by Fischer et al. [52] was made available online by the CASTLES Survey [29].

## 2.2 Observations

### 2.2.1 Strong and weak lensing

The first gravitational lens Q0957+561 was discovered in 1979 by Walsh, Carswell & Weymann [189] during a search for optical counterparts of quasar candidate radio sources (see Fig. 2.2). In this lens, two images of a distant  $R \approx 17.0$  quasar are observed  $6.1''$  apart around an elliptical galaxy that is the central galaxy of a galaxy cluster. We will have a close look at this system in chapter 3. Since 1979, a number of multiply imaged lens systems have been found; a comprehensive collection of observational facts and theoretical models has been made available online by Kochanek et al. as the CASTLES survey [29]. In their table, 48 certain and 6 insecure cases of multiply imaged quasars or galaxies (which are even seen as a ring in cases of very good alignment) are given. These lenses all have image separations of the order of arcseconds and are thought to be caused by single galaxies or by galaxies with a perturbation from some other galaxy or galaxy cluster. For most systems theoretical lens model are published or at least available on the CASTLES web site.

For some time, it had not been possible to find the lens in some of the multiple imaged quasar



systems (for example the clover leaf H1413+117). This led to speculations about the existence of “dark galaxies” [88, 72] that are only seen by the effect of their mass. Owing mostly to infrared imaging with NICMOS on the Hubble Space telescope, however, several of the missing lenses have been found, such as in the case of the clover leaf [96] and 10 other lenses in the CLASS lens sample [85]. Jackson et al. [85] find 10 lens galaxies out of 10 radio-selected gravitational lenses and conclude that the “dark lens” hypothesis is probably ruled out unless the dark galaxies are very massive with a sharp cut-off towards lower masses. Since some of the binary quasars mentioned above are also not thought to be gravitational lenses anymore, it seems that dark galaxies are probably not needed to explain multiply imaged systems.

In rich galaxy clusters multiple images with even larger image separations of  $\approx 30''$  of background galaxies have been observed. Some of the images are distorted by the cluster into giant arcs and counter-arcs of up to some  $15''$  length. Moreover, the background galaxies behind the cluster are weakly distorted by the gravitational potential of the cluster. This was first detected in 1990 [183] and has become one of the most booming subjects of gravitational lensing. In many galaxy clusters the gravitational lensing signal of the dark matter was detected, it has become possible to map the dark matter distribution in galaxy clusters. Such studies provide an important confirmation of mass determinations from velocity dispersion studies and X-ray analyses, although the mass predictions do not always agree. The study of the weak distortions of background galaxies is known as “weak lensing”, although even the dark matter in the cores of galaxy clusters with multiple images (the “strong lensing” regime) can be mapped. It has also been possible to detect the gravitational lensing effect of the large scale structure of the universe with this effect around quasars [174], and even filaments between massive galaxy clusters [33]. The history and most recent advances in this field is well covered by the recent reviews by Mellier [115] and Bartelmann & Schneider [13].

### 2.2.2 Microlensing

In another extreme, image splitting at the microarcsecond level from the lensing effect of stars or other compact objects cannot be resolved by current telescopes yet. This so-called “microlensing” can be observed as a flux variation of the background object because the lensing mass also magnifies the background object. Two kinds of microlensing are known: (1) Microlensing of stars by compact objects in our own galaxy, and (2) microlensing of background quasars by compact objects in *other* galaxies.

About 300 high-amplification events due to microlensing of stars in the Galaxy and in the Magellanic Clouds have now been recorded in extensive monitoring programs of several million stars [2, 4, 8, 185]. The microlensing can be observed as a highly symmetric achromatic flux variation of the background star due to the passing of a compact object near the line of sight (see Fig. 3.1). In the direction of the Large Magellanic Cloud (LMC) between 13 and 17 events were observed, depending on the choice of detection criteria [5]. There are even candidates for microlensing of stars in the Andromeda galaxy [40, 41, 7] (which is likely to have a factor of 10 higher optical depth than the LMC).

In this thesis, we are concerned with the second kind of microlensing. Curiously, it was the first kind to be discovered (by four years): in 1989 Irwin et al. [81] announced the detection of

a brightness variation of one of the four images of the quadruply imaged quasar Q2237+0305 (see Fig. 2.3). In this system, two lensing effects need to be considered separately: the quasar is situated almost directly behind the centre of a spiral galaxy. During the Center for Astrophysics (CfA) redshift survey, the quasar was discovered since its spectrum was superimposed on the galaxy spectrum [78]. Due to this special geometry, the quasar is quadruply imaged by the gravitational potential of the spiral galaxy, so that four images are observed. The microlensing then takes place in the light paths of each individual quasar image.

Chang & Refsdal [31] had already predicted in 1979 that due to the high surface mass density in systems with multiple gravitationally lensed images, “star disturbances” in the light path should cause strong brightness fluctuations due to the relative motion of observer, lensing galaxy and quasar. The quasar image light paths essentially glide through the galaxy like scanning beams. In such systems, the microlensing effect is caused the whole ensemble of compact objects near the light path. The effect is highly nonlinear, so that the effect of single objects is rather small [195]. Continued monitoring has shown that the four images of quasar Q2237+0305 all show strong, independent flux variations [39, 125]. More recent data by the OGLE group [209] show that the four quasar images in this system “perform” what can be called “roller coaster” (Wambsganss, July 1999) variations with amplitudes of more than a magnitude. Other cases of microlensing in multiply imaged quasars have also been reported, for example, in the clover leaf H1413+117 [150] and in the already mentioned double quasar Q0957+561 [157].

In chapters 3 and 4 the microlensing properties of the double quasar Q0957+561 and the quadruple quasar Q2237+0305 will be studied using numerical microlensing simulations and new observational data. The relevant literature will also be discussed in detail in these chapters.

## 2.3 Distances and redshifts in cosmology

In a gravitational lens system, the distances to the source and the gravitational lens play an important role. In the standard cosmological model, distances are calculated by integrating over the line element  $ds$  in the so called Robertson-Walker metric:

$$ds^2 = c^2 dt^2 - R^2(t) \left[ \frac{dr^2}{1 - kr^2} + r^2 (d\theta^2 + \sin^2\theta d\phi^2) \right]. \quad (2.2)$$

It is the metric of a space with spatially constant but time-dependent curvature  $K(t) = k/R(t)^2$ , where  $k$  is  $+1$ ,  $0$  or  $-1$  and  $R(t)$  is the curvature radius that scales the spatial part of the metric.  $r$ ,  $\theta$  and  $\phi$  are the spherical coordinates,  $t$  is the time and  $c$  the speed of light. In chapter 5, we discuss limits on a generalization of the  $k = 0$  Robertson-Walker metric, but in chapters 3 and 4 we only work with the Robertson-Walker metric.

If light is emitted it also expands with the universe, so that light with a wavelength  $\lambda_e$  from a distant source that has been emitted at the time  $t_e$  is redshifted by the expansion of the universe and has the wavelength  $\lambda_0$  when it is observed at the time  $t_0$ . This is expressed by the redshift  $z$ :

$$1 + z = \frac{\lambda_0}{\lambda_e} = \frac{R(t_0)}{R(t_e)}. \quad (2.3)$$

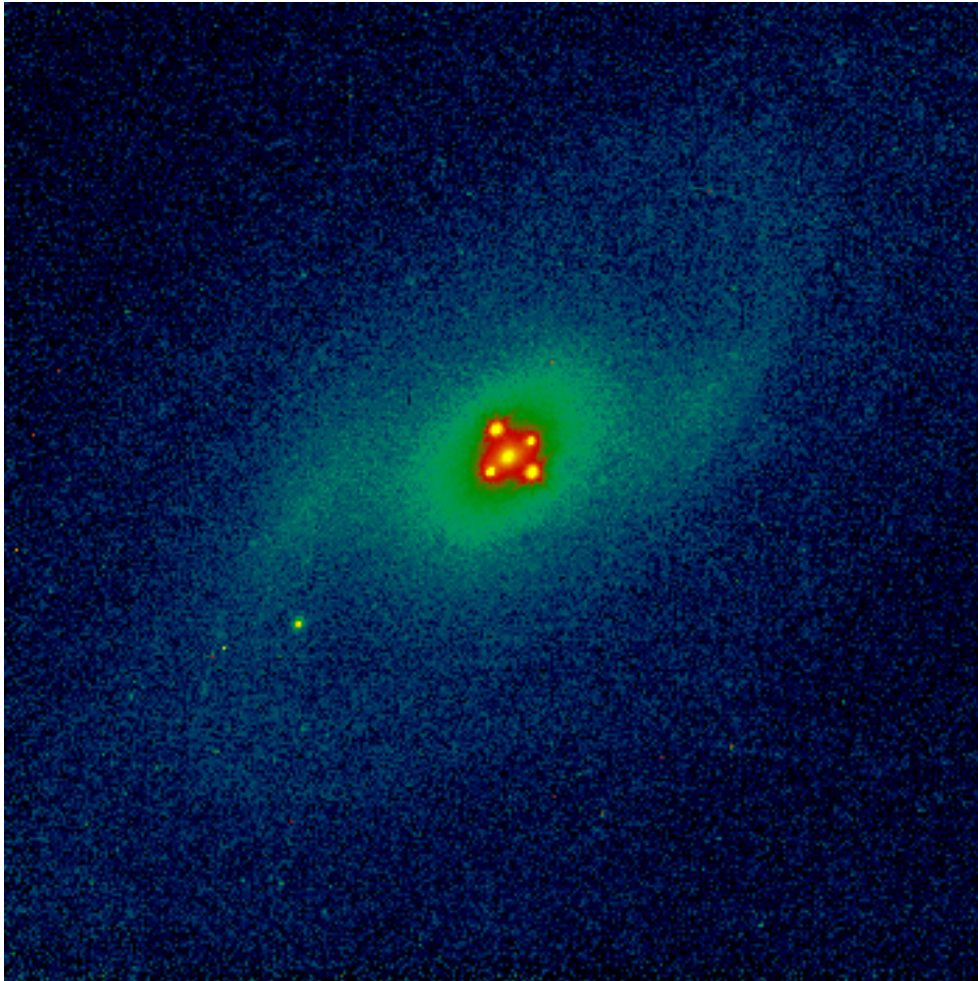


Figure 2.3: The gravitational lens system Q2237+0305 observed with Hubble Space Telescope in the  $V$ -band. In the centre of the spiral galaxy, four images of the same background quasar are seen situated around the bright galaxy core. The separation of the images from the galaxy core is  $\approx 0.9$  arcsec. The image data were retrieved from the Hubble Space Telescope Archive and were original proposed by Westphal [201].

The redshift  $z$  can be used to denote the time of emission  $t_e$  and is also often used as a measure of the distance of the source. There are several ways one can calculate distances with the Robertson-Walker metric. For the use in gravitational lensing, the relation between the separation of two sources that subtends a specific angle and the distance of the objects needs to be equal to the Euclidean formula:

$$\text{separation} = \text{angle} \times \text{distance}. \quad (2.4)$$

Distances for which this relation holds are called angular-diameter distances. The angular-diameter distances will be given here and throughout this thesis only for a homogeneous  $\Omega = 1$ ,  $\Lambda = 0$  universe, for more general universes they can be looked up or calculated with the relations in [170, page 141] or [94]. In gravitational lensing the quantities that depend on the cosmology are summed up in the normalization of the lensing masses (as shown in eq. (2.14)). The angular-diameter distance of a source at a redshift of  $z$  is given as a solution of the Dyer-Roeder equation ([44],[170, page 142]):

$$D = \frac{2}{(1+z)^2} \frac{c}{H_0} (1+z - \sqrt{1+z}). \quad (2.5)$$

The angular-diameter distance between two objects at redshifts  $z_1$  and  $z_2$ ,  $z_1 \leq z_2$ , along the same line of sight is given by:

$$D_{12} = \frac{2c}{H_0} (1+z_1) [R_1(z_2) R_2(z_1) - R_1(z_1) R_2(z_2)], \quad (2.6)$$

where

$$R_1(z) = \frac{1}{1+z} \quad \text{and} \quad (2.7)$$

$$R_2(z) = \frac{\sqrt{1+z}}{(1+z)^2}, \quad (2.8)$$

so that in general  $D_{12} \neq D_2 - D_1$ . The measured flux from a source in an expanding universe is reduced compared to a static Euclidean space since in the expanding universe fewer photons with less energy arrive at the detector in a given time. If the total flux of a source is to be calculated, one has to use the corrected luminosity distance  $D_L$  to calculate the area of the hypersphere the luminosity of the source is passing through.  $D_L$  is equal to  $(1+z)^2$  times the angular-diameter distance.

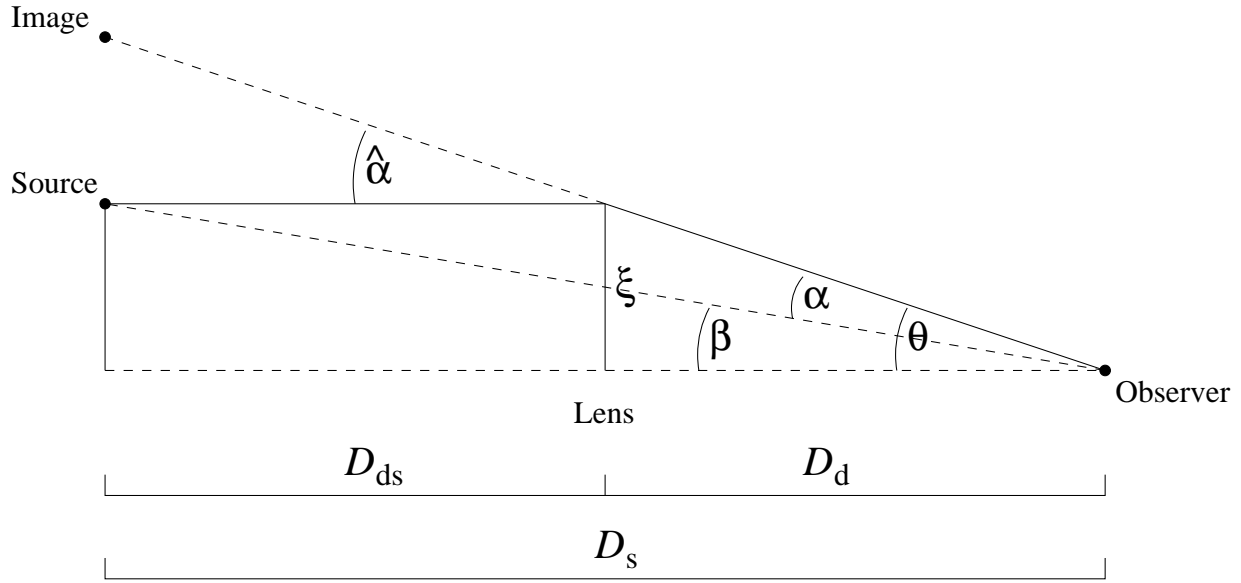


Figure 2.4: Diagram of a gravitational lens system. Explanation of symbols is given in the text. Reproduced with slight modifications from [120].

## 2.4 Single plane lensing<sup>2</sup>

### 2.4.1 Lens equation

The geometry of a typical gravitational lens system with a single lens is shown in Figure 2.4. A light ray from the source is deflected by the gravitational lens at the distance  $D_d$  from the observer by the angle  $\hat{\alpha}$ , so that it is observed at the angle  $\theta$ . Without the lens it would have been observed at  $\beta$ . In lensing situations like this, the extent of the lens in the direction of the optical axis is usually much smaller than the distances between observer and lens  $D_d$ , and between lens and source  $D_{ds}$ . It can be assumed that the lens is thin when compared with the whole light path. The mass distribution of the lens can be replaced by the projected surface mass distribution on a plane, called the lens plane. The gravitational effect of the lens can be calculated by integrating over the surface elements  $d^2\xi$  with the surface mass density  $\Sigma$  in the lens plane using Einstein's result from eq. (2.1) for the individual deflection angles. The deflection angle  $\vec{\alpha}$  at the position  $\vec{\xi}$  is thus given by the following generalization of (2.1) for an extended mass distribution:

$$\vec{\alpha}(\vec{\xi}) = \frac{4G}{c^2} \int \frac{(\vec{\xi} - \vec{\xi}') \Sigma(\vec{\xi}')}{|\vec{\xi} - \vec{\xi}'|^2} d^2\xi'. \quad (2.9)$$

<sup>2</sup>Many derivations in this section follow the lecture notes by Narayan & Bartelmann [120].

For  $n$  point masses  $m_i$  at positions  $\vec{\xi}_i$  one has to use delta functions

$$\Sigma(\vec{\xi}) = \sum_{i=1}^n m_i \delta^2(\vec{\xi} - \vec{\xi}_i), \quad (2.10)$$

where  $\delta^2$  is the 2-dimensional delta-function. The plane parallel to the lens plane at the distance  $D_s$  of the source from the observer is called the source plane. In general, the angles in Figure 2.4 are vectors since the deflection is not necessarily always radial. In the case of small angles it is

$$\vec{\theta} D_s = \vec{\beta} D_s + \vec{\alpha} D_{ds}. \quad (2.11)$$

The small-angle approximation is valid in the known cases of gravitational lensing, even in galaxy clusters the deflection angles are only of the order of 30 arcsec. By introducing the reduced deflection angle  $\vec{\alpha}$  that is seen by the observer

$$\vec{\alpha} = \frac{D_{ds}}{D_s} \vec{\alpha} \quad (2.12)$$

one obtains the lens equation:

$$\vec{\beta} = \vec{\theta} - \vec{\alpha}(\vec{\theta}). \quad (2.13)$$

This is the fundamental equation of gravitational lensing. It relates the source position  $\vec{\beta}$  with the image position  $\vec{\theta}$  and the deflection angle  $\vec{\alpha}$ . It is nonlinear in general, so it may have multiple image solutions  $\vec{\theta}$  for a given source position  $\vec{\beta}$  and deflection field  $\vec{\alpha}(\vec{\theta})$ . It also holds in curved spacetimes as long as the distances  $D_d$ ,  $D_s$  and  $D_{ds}$  are defined to be angular-diameter distances.

The lens equation can also be expressed by Fermat's principle. If one defines the critical surface density

$$\Sigma_{\text{crit}} = \frac{c^2}{4\pi G} \frac{D_s}{D_d D_{ds}} \quad (2.14)$$

and the convergence

$$\kappa = \Sigma / \Sigma_{\text{crit}}, \quad (2.15)$$

one can write the deflection potential  $\psi$  as

$$\psi(\vec{\theta}) = \frac{1}{\pi} \int \kappa(\vec{\theta}') \ln |\vec{\theta} - \vec{\theta}'| d^2\theta'. \quad (2.16)$$

Since  $\vec{\nabla} \ln |\vec{\theta}| = \frac{\vec{\theta}}{|\vec{\theta}|^2}$ , it follows from the definitions of Fig. 2.4 and eqs. (2.9) and (2.12) that

$$\vec{\alpha} = \vec{\nabla} \psi. \quad (2.17)$$

The time-delay function can then be defined by

$$t(\vec{\theta}) = \frac{1+z_d}{c} \frac{D_d D_s}{D_{ds}} \left[ \frac{1}{2} (\vec{\theta} - \vec{\beta})^2 - \psi(\vec{\theta}) \right], \quad (2.18)$$

where  $z_d$  is the redshift of the lens [170, page 146]. This function describes the time-delay due to the longer lightpath and the gravity field of the lens as compared to the unperturbed light travel time. It follows from the lens equation (2.13) that  $\vec{\nabla} t(\vec{\theta}) = 0$ ; the images lie at the extrema of the time delay function [20, 171]. Also, since the angular-diameter distances for known redshifts scale with the Hubble constant  $H_0$ , the measurement of a time-delay between the images of a multiple image gravitational lens system determines the Hubble constant if one has a theoretical model  $\psi(\vec{\theta})$  for the system [146]. Furthermore, since  $\Delta \ln |\vec{\theta}| = 2\pi\delta^2(\vec{\theta})$ , it follows from eq. (2.16) that

$$\Delta \psi = 2\kappa. \quad (2.19)$$

The deflection potential  $\psi$  and deflection field  $\vec{\alpha}$  can be found by solving the 2-dimensional Poisson equation (2.19).

### 2.4.2 Magnification

The local properties of the lens mapping (2.13) can be studied with the Jacobi matrix  $A_{\vec{\beta}}$ :

$$A_{\vec{\beta}} = \frac{\partial \vec{\beta}}{\partial \vec{\theta}} = \left( \delta_{ij} - \frac{\partial \alpha_i(\vec{\theta})}{\partial \theta_j} \right) = M^{-1}. \quad (2.20)$$

The images are magnified by the ratio between the solid angles of the image and the source. Since gravitational lensing preserves surface brightness due to Liouville's theorem [170, page 116], the image fluxes are magnified by this ratio; the magnification  $\mu$  is given by the determinant of the magnification matrix  $M$ :

$$\mu = \det M = \frac{1}{\det A_{\vec{\beta}}}. \quad (2.21)$$

Formally negative magnification means a mirror-inversion of the image with respect to the source. The Jacobi matrix can be written as the sum of a convergence and a shear matrix. Using the abbreviation  $\psi_{,ij} = \partial^2 \psi / \partial \theta_i \partial \theta_j$  and eq. (2.19), the convergence can be written  $\kappa = \frac{1}{2}(\psi_{,11} + \psi_{,22})$ . If one also defines the shear magnitude  $\gamma$  and orientation  $\varphi$  by setting  $\gamma \cos 2\varphi = \frac{1}{2}(\psi_{,11} - \psi_{,22})$  and  $\gamma \sin 2\varphi = \psi_{,12} = \psi_{,21}$  and using eq. (2.17) one obtains:

$$A_{\vec{\beta}} = \begin{pmatrix} 1 - \kappa & 0 \\ 0 & 1 - \kappa \end{pmatrix} - \gamma \begin{pmatrix} \cos 2\varphi & \sin 2\varphi \\ \sin 2\varphi & -\cos 2\varphi \end{pmatrix}. \quad (2.22)$$

Using eq. (2.21), the magnification  $\mu$  at a position with convergence  $\kappa$  and shear  $\gamma$  is given by

$$\mu = \frac{1}{(1 - \kappa)^2 - \gamma^2}. \quad (2.23)$$

A circular source is elliptically distorted to an axis ratio  $\left(\frac{1+\gamma}{1-\gamma}\right)$  by the shear, the major axis lying along the direction of  $\phi$ , while the convergence changes the scale of both axes. Since  $\kappa$  and  $\gamma$  are derived from the same potential, it is possible (up to an integration constant) to determine the surface mass density in galaxy clusters from the analysis of the deformations of background galaxies behind galaxy clusters [90, 115, 13].

### 2.4.3 The point mass lens

For a point mass  $M$ , the deflection angle is directed towards the mass, and one finds from eqs. (2.1), (2.12) and (2.13) that for the impact parameter  $R = \theta D_d$

$$\beta(\theta) = \theta - \frac{D_{ds}}{D_d D_s} \frac{4GM}{c^2 \theta}. \quad (2.24)$$

If  $\beta = 0$  for a source directly on the optical axis, it is imaged as a ring with the radius

$$\theta_E = \left[ \frac{4GM}{c^2} \frac{D_{ds}}{D_d D_s} \right]^{1/2}, \quad (2.25)$$

$\theta_E$  is called the Einstein radius. The lens equation for the point mass lens (2.24) can thus be written  $\beta = \theta - \frac{\theta_E^2}{\theta}$ . A point mass lens will always produce two images at the positions of the solution of the quadratic eq. (2.24)

$$\theta_{\pm} = \frac{1}{2} \left( \beta \pm \sqrt{\beta^2 + 4\theta_E^2} \right) \quad (2.26)$$

with a separation  $\sqrt{\beta^2 + 4\theta_E^2}$ . The magnification  $\mu$  of the images is given by the ratio of the surface elements  $\mu = \frac{\theta}{\beta} \frac{d\theta}{d\beta}$ :

$$\mu_{\pm} = \left[ 1 - \left( \frac{\theta_E}{\theta_{\pm}} \right)^4 \right]^{-1}. \quad (2.27)$$

Sources within the Einstein ring are strongly magnified, whereas for large  $\beta$ , one image appears highly demagnified near the source and the other appears undisturbed at  $\theta \approx \beta$ .

The magnification curve for a star that passes behind a point lens can be obtained by adding up the two magnifications from eq. (2.27). If we introduce  $u = \beta/\theta_E$  for the impact parameter, it follows<sup>3</sup>

$$\mu_{\pm} = \frac{\theta_{\pm}^4}{(\theta_{\pm}^2 + \theta_E^2)(\theta_{\pm}^2 - \theta_E^2)} = \frac{1}{2} \pm \frac{2 + u^2}{2u\sqrt{u^2 + 4}}, \quad (2.28)$$

so that the total magnification is ([63] lists the complete derivation history of this well-known relation)

$$\mu = \mu_+ - \mu_- = \frac{2 + u^2}{u\sqrt{u^2 + 4}}. \quad (2.29)$$

The second magnification term  $\mu_-$  is subtracted since it is formally negative because the image is mirror-inverted. In Figure 3.1, eq. (2.29) is illustrated by showing the total magnification of a source that passes within 0.2 Einstein radii behind a point lens as a function of the separation from the point of closest approach.

<sup>3</sup>It is helpful to use the relations  $\theta_{\pm}^2 - \theta_E^2 = \beta\theta_{\pm}$  and  $\theta_{\pm}^2 + \theta_E^2 = \pm\theta_{\pm}\sqrt{\beta^2 + 4}$ .



### 2.4.4 Compact objects in the light path

In chapters 3 and 4 we will study the light from a quasar that shines through a galaxy that acts as a gravitational lens. The quasar light bundle is magnified and sheared, and additionally “microlensed” by the stars or other compact objects in the galaxy. This situation is usually modelled by using two components for the convergence in the galaxy:

$$\kappa = \kappa_* + \kappa_c. \quad (2.30)$$

$\kappa_*$  denotes the convergence from compact objects, and  $\kappa_c$  in smooth, continuous matter (to describe elementary particles, for example). By treating the effect of  $\kappa_*$  from the  $N$  compact objects with masses  $M_i$  exactly according to (2.1) and (2.12), we obtain from eqs. (2.20) and (2.22) for deviations in the source plane  $d\vec{\beta}$  from deviations  $d\vec{\theta}$  from centre of the quasar image (orienting the shear without loss of generality horizontally) [131, 92]

$$d\vec{\beta} = \begin{pmatrix} 1 - \kappa_c - \gamma & 0 \\ 0 & 1 - \kappa_c + \gamma \end{pmatrix} d\vec{\theta} + \frac{D_{ds}}{D_d D_s} \frac{4G}{c^2} \sum_{i=1}^N \frac{M_i (d\vec{\theta} - d\vec{\theta}_i)}{|d\vec{\theta} - d\vec{\theta}_i|^2}. \quad (2.31)$$

This is the fundamental equation used in microlensing studies. By rescaling<sup>4</sup>  $\theta' = \theta/\theta_0$  and  $\beta' = \beta/(\theta_0(1 - \kappa_c))$ , with  $\theta_0 = \sqrt{\frac{4GM_\odot}{c^2|1 - \kappa_c|} \frac{D_{ds}}{D_d D_s}}$ , and defining the reduced shear

$$g = \frac{\gamma}{1 - \kappa_c}, \quad (2.32)$$

the equation can be normalized so that constant factors vanish

$$d\vec{\beta}' = \begin{pmatrix} 1 - g & 0 \\ 0 & 1 + g \end{pmatrix} d\vec{\theta}' + \text{sign} \left( \frac{1}{1 - \kappa_c} \right) \sum_{i=1}^N \frac{m_i (d\vec{\theta}' - d\vec{\theta}'_i)}{|d\vec{\theta}' - d\vec{\theta}'_i|^2}. \quad (2.33)$$

The masses of the compact objects  $m_i$  are now given in units of solar masses  $M_\odot$ . It can be seen that for overcritical  $\kappa_c = \frac{\Sigma_c}{\Sigma_{\text{crit}}} > 1$ , the compact objects formally have a repulsive effect. In the primed coordinate system, various combinations of  $\gamma$  and  $\kappa_c$  form a family parametrized by the reduced shear  $g$ .

### 2.4.5 Critical lines and caustics

It was shown in Sect. 2.4.1 that the gravitationally lensed images lie at the extrema of the time-delay function (2.18). Moving the source in the source plane will change the positions of these extrema and, hence, the image positions. In the unperturbed case far from a nonsingular lens with no discontinuities, only one image is visible. In the case of point mass lenses, we have shown in Sect. 2.4.3 that there are always two images, of which one is strongly demagnified for a source far from the lens. In an ensemble of point masses there will also be one strongly demagnified additional image close to each lens for a source far from the ensemble. When the source is

---

<sup>4</sup> $\theta_0$  is the Einstein radius (2.25) of a star with an additional sheet of constant surface mass density  $\kappa_c$ . In the following, we will nevertheless use the definition (2.25) for the Einstein radius  $\theta_E$  unless otherwise noted.

moved closer to the lens (or lens ensemble), a pair of images will be created at a saddle point of the time delay function. This point may be located through the vanishing of the determinant of the curvature matrix of the time-delay function [20].

The curvature matrix of the time-delay function  $t_{,ij}$  is, except for a constant factor, equal to the Jacobi matrix  $A_{\vec{\beta}}$  defined in eq. (2.20), so that the so-called “critical line” where image pairs are created can be found when the determinant of  $A_{\vec{\beta}}$  vanishes.

If the critical lines are mapped onto the source plane via the lens equation (2.13), one obtains the so-called “caustics”. These lines hence separate zones of different image multiplicity of the background source. Since  $\det A_{\vec{\beta}}$  vanishes on the caustics, the magnification  $\mu$  (eq. 2.21) is formally infinite on these lines. In practice, the magnification will just be very high because real sources are sufficiently extended<sup>5</sup>.

An example for a critical line and caustic structure is given in Figure 2.5. The figure shows the critical curve and caustics of two  $1 M_{\odot}$  lenses on the x-axis with a separation of 1.8 Einstein radii (only here according to the definition of the Einstein radius with a constant sheet of matter in Footnote 4 on page 4) with an additional sheet of smooth matter  $\kappa_c$  and a (horizontal) shear  $\gamma$ . The resulting reduced shear is  $g = \frac{\gamma}{1-\kappa_c} = -0.5$  (this configuration was first described in [175]).

From this figure it can be taken how much more complex gravitational microlensing becomes in the case of several compact objects lenses, an additional shear and possible smooth matter term. Whereas in the case of a single lens a smooth magnification curve as shown in Fig. 3.1 results, we would expect several strong magnification jumps as the source crosses the different caustics of the right panel of Fig. 2.5. This is another way of illustrating the highly nonlinear character of microlensing. The plot was produced using the analytical formula from Witt [205, page 65].

## 2.5 Lensing in inhomogeneous or anisotropic universes

The last section described the gravitational lens effect due to a single lens. If we wish to include the effect of density inhomogeneities due to the large scale structure of the universe, we have to use the equation of geodesic deviation for the transverse separation  $\vec{\xi}$  between neighbouring rays in a light bundle ([170, page 110],[13, page 118])

$$\frac{d^2 \vec{\xi}}{d\lambda^2} = \mathcal{T} \vec{\xi}, \quad (2.34)$$

where  $\mathcal{T}$  is the optical tidal matrix which describes the influence of the space-time curvature on the light path. For the standard cosmology,  $\mathcal{T}$  is proportional to the unity matrix, so there is no shear effect. When a spatially varying potential due to density inhomogeneities is introduced,  $\mathcal{T}$  becomes a more complicated, but still symmetric matrix.

The light deflection due to mass inhomogeneities can be found from the difference between  $\vec{\xi}$  in a universe with and without density inhomogeneities. In the approximation of small inhomogeneities (compared to the Hubble volume) with small Newtonian potentials  $\Phi \ll c^2$ , and small

<sup>5</sup>Even for point sources the magnification is not infinite because the geometrical optics description fails near critical curves. A wave optics description leads to a finite magnification [126],[170, page 217].

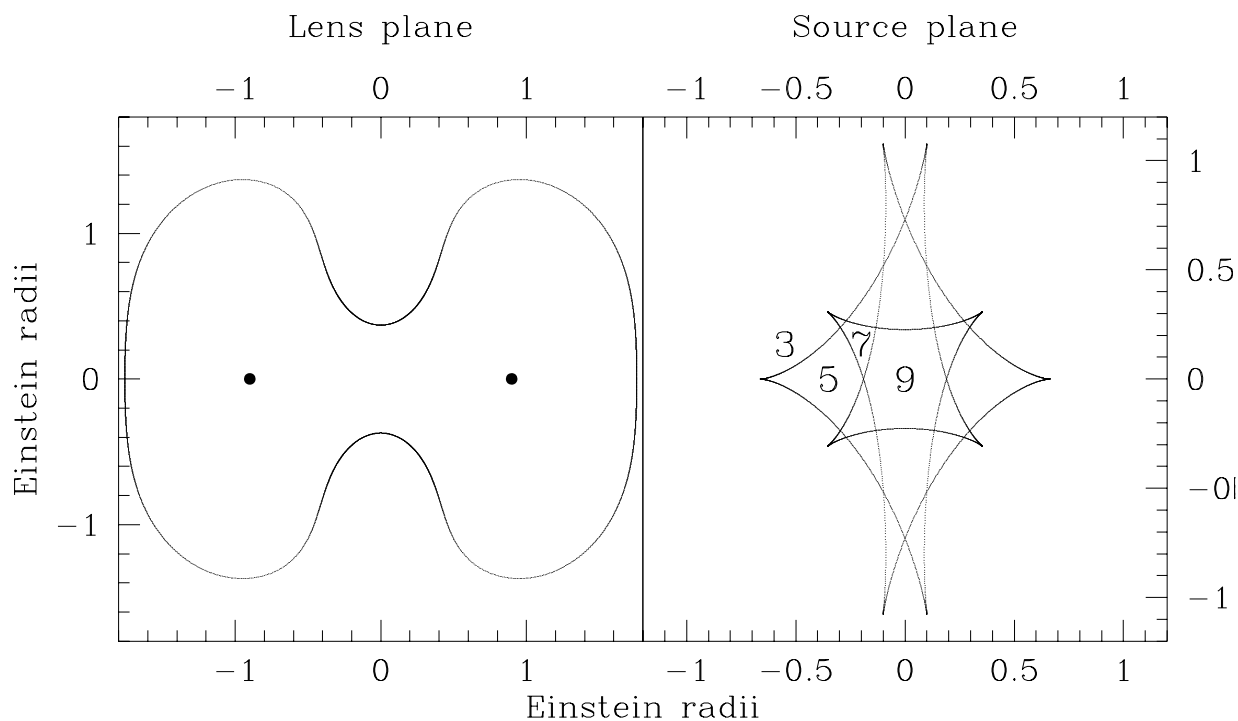


Figure 2.5: Critical line (lens plane) and caustics (source plane) of a system of two point masses with external shear  $\gamma$  and an additional constant sheet of matter  $\kappa_c$ . The point masses of  $1 M_\odot$  are located at the marked points in the left panel at  $+0.9$  and  $-0.9$  Einstein radii on the x-axis. The reduced shear is aligned horizontally with a magnitude  $g = \frac{\gamma}{1-\kappa_c} = -0.5$ . The numbers in the right panel indicate image multiplicities in a few regions of the source plane, the multiplicities in other regions are accordingly. The Einstein radius measure in this figure was defined in Footnote 4 on page 17 and includes the effect of the constant sheet of matter.

deflection angles, one obtains in a flat universe an integral over the transverse derivatives of the Newtonian potential [13, page 122]

$$\vec{\alpha}(\vec{\theta}, w) = \frac{2}{c^2} \int_0^w dw' \left(1 - \frac{w'}{w}\right) \nabla_{\perp} \Phi(w' \vec{\theta}, w'), \quad (2.35)$$

where  $\Phi(w \vec{\theta}, w)$  describes the Newtonian potential at the angular-distance  $w$  for a ray of the light bundle that encloses an angle  $\vec{\theta}$  with the central ray. In an open or closed universe, the integral kernel  $(1 - \frac{w'}{w})$  of (2.35) will be more complicated (the full relations are given in [13]).

The deflection of light rays can only be measured relative to another light ray because absolute deflections cannot be observed. The distortion of the light bundle, however, is observable (eq. (2.20)). In space-times with more general metrics, eq. (2.34) still holds and can be solved by inserting the corresponding  $\mathcal{T}$  [176]. Relations for  $\mathcal{T}$  are given in chapter 5 (Sect. 5.7) where (2.34) is solved to determine image distortions in a cosmological model with universal rotation.

# Chapter 3

## Limits on MACHOs from microlensing in the double quasar Q0957+561

### 3.1 Halo dark matter = MACHOs?

In this chapter, we study a particular candidate for dark matter: massive, compact objects that could populate the halos of galaxies. Alluding to the dark matter candidate WIMP (“weakly interacting massive particle”), Kim Griest [63] coined the acronym MACHO (“massive astrophysical compact halo object”) for these objects, which we will frequently use here.

A direct test to prove or reject the possibility that the halo of the Milky Way consists of dark, compact objects was proposed by Paczyński [132] by making use of gravitational microlensing: If the brightness of at least a million stars in the Large Magellanic Cloud (LMC) could be regularly measured, at any given time about one of them should be significantly magnified due to a halo object passing in front of it and focussing the light rays to the observer. The light curve of the affected background star should show a very characteristic and achromatic behaviour (see Fig 3.1 and eq. (2.29)). Soon after Paczyński’s paper, various groups started big observational programs to investigate this promising possibility. The first microlensing events were found in 1993 by Alcock et al. [4] and Aubourg et al. [8]. The most recent results from a sample of 13 to 17 events (depending on the criteria chosen for the classification as an microlensing event) indicate that some 20% of the dark matter in the Milky Way halo may consist of such objects (Alcock et al. [5]). The likely masses of the microlenses are very dependent on the model of the galaxy halo, but generally of the order of a few tenth of a solar mass. This is higher than originally suggested for the “prime candidate” brown dwarfs, but the uncertainty of this mass determination is large. Moreover, Alcock et al. also consider that the events could also have been caused by microlensing objects in the halo of the Large Magellanic Cloud (LMC). The events then would not tell us anything about the galaxy halo. The latter interpretation was initiated by Sahu [159] and Wu [210] and has recently been supported by the fact that in the one microlensing event where the location of the microlens is known [3] it is not situated in the galaxy halo, but in the SMC (Small Magellanic Cloud, which is also studied by the MACHO collaboration [4]). The biggest difficulty of these programs is that the fraction of background stars that are significantly

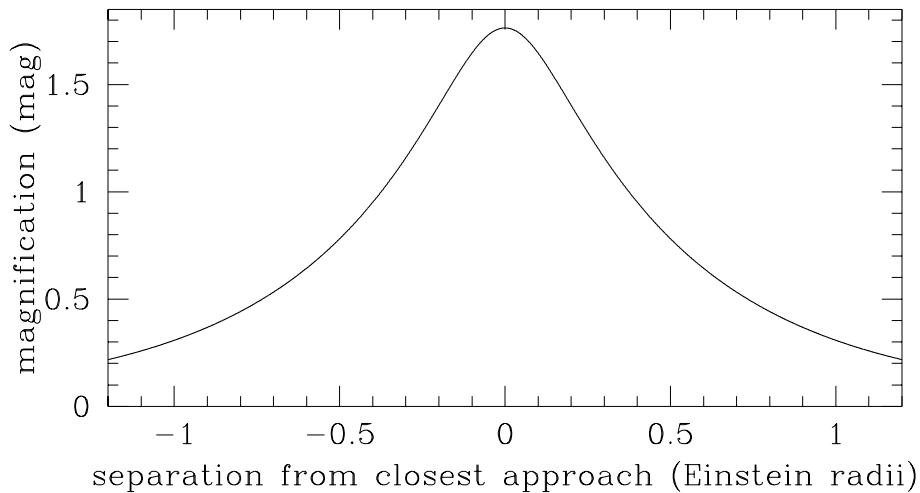


Figure 3.1: Magnification (in magnitudes) of a star at a distance of 15 kpc that is lensed by a point mass lens of  $0.1 M_{\odot}$  that passes in linear motion halfway to the star with an impact parameter of 0.2 Einstein radii (0.05 mas). The x-axis is the distance from the point of closest approach in Einstein radii  $\theta_E \approx 0.23$  mas.

affected by microlensing, the so-called “optical depth” [188, 121], towards the LMC is less than  $10^{-6}$ , so that millions of stars have to be continuously monitored to see this effect.

## 3.2 MACHOs in other galaxies

Already in 1981, Gott [62] proposed to use gravitational lensing in a very different optical depth regime to test whether halos of *other* galaxies are made of compact objects: the light bundles from a multiply imaged quasar pass through a lensing galaxy and its dark halo on their way to the observer. The distances involved here are about five orders of magnitude larger than in the microlensing searches towards the LMC (Gigaparsec rather than some 55 kpc), and the optical depths involved are six orders of magnitude higher, of order unity. These light bundles probe the graininess of the galaxy halo: if the dark matter there consists of some kind of elementary particles, the light bundles should be unaffected; if it is made of compact astrophysical objects, the light bundles can probe it. The measured brightnesses of the quasar images should vary as a function of time due to the changing relative positions between lens, source, and observer (Chang & Refsdal [31]). The optical depth in these cases is high enough to basically cause fluctuations of the measured flux of a quasar image all the time.

Since quasars are intrinsically variable as well, it is not trivial to decide whether an observed variability is intrinsic or microlensing-induced [71, 36, 73]. With normal quasars, it had so far only been possible to derive limits from quasar variability on the contribution of compact objects to the density of the universe [172, 37].

In the case of a multiply imaged quasar, however, the intrinsic fluctuations should show up

coherently in all images – with a certain time delay – whereas the microlensing changes occur uncorrelated in the various images. Once well-sampled light curves of two (or more) quasar images are obtained and the time delay  $\Delta t$  (due to the different light paths of different light bundles) as well as the magnitude difference  $\Delta m$  (due to the different magnifications of the quasar images by the galaxy and cluster gravitational potential) are known, one can shift the two light curves in time and magnitude by the appropriate amounts  $\Delta t$  and  $\Delta m$  and subtract them from each other. All remaining fluctuations in the “difference light curve” must be due to microlensing. In particular, if the difference light curve is flat, this indicates that there was no microlensing going on during the period of observation.

### 3.3 Limits from microlensing

#### 3.3.1 Q2237+0305: The Einstein cross

As mentioned in Sect. 2.2.2, microlensing was first detected in the quadruple quasar Q2237+0305 (see Fig. 2.3) by Irwin et al. [81]. A single peak in the light curve of image A of less than 100 days duration and  $\gtrsim 0.2$  mag amplitude was observed in 1988. In this system, the predicted delay between the images is of the order of hours [169], so that the variations should have shown up in all quasar images at the same time, if the variability was intrinsic to the quasar. Wambsganss et al. [194] as well as Webster et al. [198] found an upper limit on the size of the continuum emission region of the quasar around  $10^{15}$  cm for lens masses around few tenths of a solar mass.

Webster et al. [198] also noted discrepancies in different theoretical models of the system of a factor 2 between the surface mass densities  $\kappa$  and shear  $\gamma$  at the quasar images. They concluded that this would inhibit strong conclusions on the microlensing objects. Rather, they proposed to measure  $\kappa$  and  $\gamma$  from microlensing statistics of a longer light curve. Witt & Mao [207] noted further that the microlensing properties depend on the direction of the shear with respect to the motion of the quasar through the caustic pattern of compact objects in the lens galaxy. In 1996, Lewis & Irwin [109] compared the Q2237+0305 light curve with numerical simulations and found the masses of the compact microlensing objects to be in the range from  $0.1M_{\odot}$  up to  $10.0M_{\odot}$ .

Since 1989, many more microlensing variations were reported in this system. We present the microlensing history of this system including new microlensing evidence from the Apache Point Observatory Monitoring program in the years 1995-97 and a discussion of the recent results from the OGLE group in chapter 4.

#### 3.3.2 Q0957+561

The gravitationally lensed double quasar Q0957+561 has now been monitored for almost two decades by many groups (see, for example, Schild & Thomson [162]). In this system, the time-delay between the two quasar images is about 417 days, so that microlensing variations are harder to spot than in Q2237+0305, where the time-delay is only several hours. In addition, there was no agreement on the value of the time-delay of Q0957+561 for some 15 years.

In the optical regime, the time-delay is now widely accepted [105, 127, 165]. Schild [163] finds indications for microlensing in his  $\approx 15$  years of optical data on the system which can be produced by stars around a solar mass, in particular a strong drop in the difference light curve of 0.4 mag in the early 80s. In their analysis of the larger data set, Pelt et al. [135] do not find evidence for microlensing variations on short time scales. We will present an analysis which is based on [168], but which includes data of full four years of observations at Apache Point Observatory [34]. An additional improvement is a more realistic use of simulated microlensing light curves (isolated data points rather than continuous sampling of the simulated curve).

Regarding the Q0957+561 time-delay estimates from radio data, there is a puzzling dependence of the time-delay on the frequency [65]. The determined time-delay from about 18 years of light curve data in the 6 cm wave band differs significantly from the optically determined time-delay. The time-delay from their about 7.5 years of data in the 4 cm wave band is consistent with the optical time-delay at about  $2\sigma$ . It is possible that this puzzle could be solved by an effect that was noted by Yonehara [222]. He found that if the intrinsic fluctuations of an sufficiently extended source happen uncorrelated at several spots on the quasar, the time-delay would depend on the spot position because a single time-delay of a lens system is exactly valid only for a point source. If the frequency of the emitted radiation  $\nu$  would correlate with the distance  $r$  from the source centre,  $\nu \sim 1/r$  (or some power of  $r$ ), this could cause a proportionality between the time-delay and the frequency of the radiation. From his calculations, however, it seems that the source would need to have a size of the order of kpc, and not pc, for this effect to be significant, which seems almost a factor 1000 too large. In chapter 4, we will discuss in more detail possible implications of microlensing observations for the source. In this chapter, we will restrict ourselves to the simple model of a Gaussian profile for the quasar brightness distribution.

### 3.4 Q0957+561: Mass models and time-delay

Q0957+561 ( $z = 1.41$ ) is lensed by a galaxy at a redshift of  $z = 0.36$  (see Figure 2.2), which is the central galaxy of a cluster of galaxies. The galaxy cluster has also been detected in X-rays [32] and in a weak lensing study [52]. In the radio regime, two jets are detected that come from the quasar [60, 61]. In addition, several “features” like an arc, possibly consisting of two elongated images of the same object, and small galaxies, two of which may also be multiple images, were discovered with the Hubble Space Telescope around the quasar and provide more constraints on the lensing model [14].

Such complex optical and radio structure places strong constraints on theoretical models for the lens, so that complex models have been developed for this system (Falco et al. [49], Grogin & Narayan [64], Barkana et al. [10], Chae [30]). For our study, we need values for the surface mass density and the local shear at the positions of the quasar images from the models. We use the model by Falco et al. [49] because it seems that there has not been sufficient change in the models to warrant an update of the parameters relevant for microlensing (Falco 1999, priv. comm.). A quantity that is often used to quantify the success of a model to fit the observables  $p_i$



with their observational uncertainties  $\sigma_i$  is the so-called reduced  $\chi^2$ :

$$\bar{\chi}^2 = \frac{1}{\text{DOF}} \sum_i \left( \frac{p_{i,\text{model}} - p_{i,\text{observed}}}{\sigma_i} \right)^2, \quad (3.1)$$

where DOF, the number of degrees of freedom, is defined as the number of constraints minus the number of free parameters of the model (the bar denotes the division by DOF). All current lensing models of Q0957+561 have  $\bar{\chi}^2 \gtrsim 5$ . Ideally, one would want a model with  $\bar{\chi}^2 \approx 1$ . In the case of Q0957+561, however, the models still seem to have great difficulties, even after the reanalysis of the Garrett et al. radio data [57] by Barkana et al. [10], to explain the details of the two radio jets and the mapping between them [30, table 6]. Barkana et al. [10] note that this could either be due to substructure in the lensing galaxy [113], or due to the effects of superluminal motions in the jet (the images were analyzed using observations from the same day, possibly neglecting positional uncertainties of 0.1 mas that could be introduced by the time-delay of  $\approx 417$  days between the light paths of the two images).

The convergence  $\kappa$  (defined in eq. (2.15)) of the lensing galaxy in the Falco et al. [49] model is represented by an approximation of the so-called King model [95]:

$$\kappa(\theta) = \frac{\Sigma}{\Sigma_{\text{crit}}} = \frac{D_{\text{ds}} \sigma_v^2}{D_s c^2} \left[ \frac{30.75}{\sqrt{\theta_c^2 + 1.334 \theta^2}} - \frac{12.75}{\sqrt{\theta_c^2 + 0.335 \theta^2}} \right]. \quad (3.2)$$

$\Sigma_{\text{crit}}$  can be calculated from eq. (2.14):

$$\Sigma_{\text{crit}} = 0.55 h_{60} \text{ g/cm}^2 = 2.6 \times 10^9 M_{\odot}/\text{kpc}^2. \quad (3.3)$$

The mass distribution (3.2) is circularly symmetric. Falco et al. fitted the velocity dispersion as  $\sigma_v = 390 \pm 4$  km/s, and the core radius as  $\theta_c = 2.9 \pm 0.1$  arcsec (see Fig. 3.2). In addition, their model contained a point mass in the galaxy centre of  $1.1 \times 10^{11} M_{\odot}$ , and an external shear component from the surrounding galaxy cluster with a magnitude of  $0.30 \pm 0.01$  with a position angle of  $63.3 \pm 0.6$  degrees (measured from north through east). With the relations from Sect. 2.4.2, the shear  $\gamma$  at the image position (the tidal field due to the matter outside the beam) can also be calculated from eq. (3.2). We adopt values for the convergence of  $\kappa_A = 0.32$  for image A and  $\kappa_B = 1.17$  for image B, for the local shear at the image positions we used  $\gamma_A = 0.18$  and  $\gamma_B = 0.83$ , respectively (Falco 1997, priv. comm.)<sup>1</sup>

In 1997, Kundic et al. [105] presented the results of two years of well sampled monitoring observations of Q0957+561 with the Apache Point Observatory. With their  $g$ -band data, they confirmed the value of  $\Delta t = 417 \pm 3$  days for the time delay between the two lensed light paths and a best value for the magnitude offset between the (time-corrected) quasar fluxes of

$$\Delta m_{AB} := \langle m_A(t) - m_B(t + \Delta t) \rangle = 0.118 \text{ mag}. \quad (3.4)$$

<sup>1</sup>Chae (2000, priv. comm.) obtains  $\kappa_A = 0.56$ ,  $\kappa_B = 1.17$ ,  $\gamma_A = 0.14$  and  $\gamma_B = 0.5$  with additional shear contributions from the cluster of  $\gamma'_A = 0.09$  and  $\gamma'_B = 0.1$  for his best fit model in [30]. This gives a feeling for the accuracy that can be reached with current theoretical models. If the Chae model would be a more correct representation of the mass distribution of the lens, we would overestimate  $\kappa_A$  and underestimate  $\gamma_B$ . We have experimented with Chae's values and found, however, that this difference is not big enough to significantly influence our results.

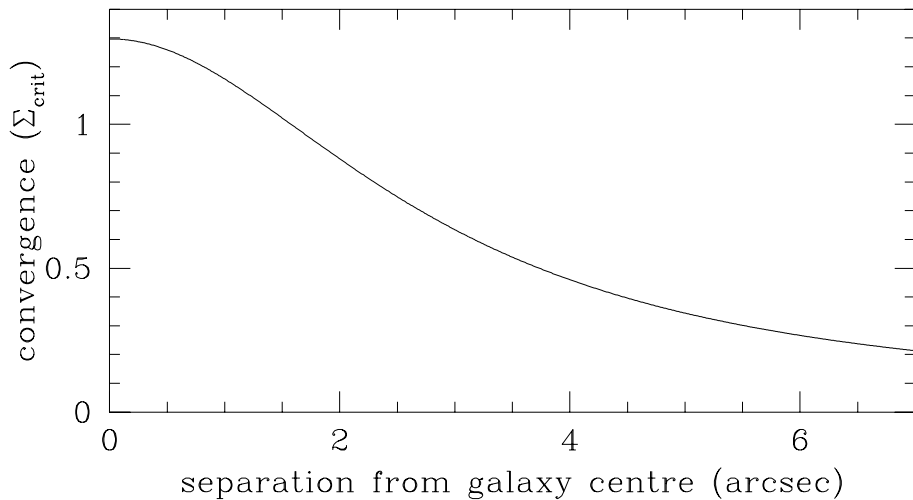


Figure 3.2: Radial profile of the convergence of the circularly symmetric Falco et al. [49] model for lensing galaxy in the Q0957+561 gravitational lens system. The two quasar images A and B have separations of  $\theta_A = 5.2''$  and  $\theta_B = 1.03''$  from the galaxy centre. The projected separations are  $26.4 h_{60}^{-1}$  kpc for image A and  $5.2 h_{60}^{-1}$  kpc for image B.

Their value for the time-delay was also confirmed by other groups [127, 165] ([127] only partly) with independent observations for these observing seasons<sup>2</sup>. With both the time delay established and mass models being available for the lens, the double quasar Q0957+561 can hence be used as a test for massive halo objects by comparison of the light curves of images A and B. We will use a slightly different value than Kundić et al. [105] for the magnitude correction  $\Delta m_{AB}$  (see Sect. 3.5.1) which was found in the reanalysis of the Apache Point data by Colley, Turner & Kundic [34], but it is still in agreement with the Kundic et al. value within the error bars.

We use Q0957+561 as a MACHO test tool by simulating the microlensing effect numerically for MACHOs of different masses. We analyze the resulting microlensed light curves and show how often microlensing-induced changes of certain amplitudes are to be expected for certain MACHO masses. Finally, we compare our numerical simulations with the most recent four-year data set from the Apache Point Monitoring program of Q0957+561 reported by Colley et al. [34], which contains two more years of data than reported in Kundic et al. [105]. Using this data set, we constrain the MACHO masses in the lensing galaxy and its dark halo.

### 3.5 Observations and simulations

We first briefly present the data set on the quasar Q0957+561 which we use. We then define the relevant numbers and parameters and illustrate how the microlensing light curve depends on the

<sup>2</sup>The correct time-delay had already been measured before. In the data of Vanderriest et al. [187] of 1989, for example, there was a similarly sharp magnitude change as the drop detected by APO in 1995. Then, however, there were still two competing time-delays of 1.1 and 1.5 years.

MACHO masses and the quasar size. Finally, the numerical technique is described which we employ to produce the microlensing light curves and to analyze them.

### 3.5.1 The Apache Point Observatory Q0957+561 light curve

In the upper panels of Fig. 3.3, the  $g$ -band light curves of quasar images A (red, between 1995 and 1997), and B (blue, between 1996 and 1998) are shown. In order to quantitatively estimate the effects of microlensing on the light curves of Q0957+561 A and B, we determined the “difference light curve” between the two quasar images by linearly interpolating the light curves. Only the procedure to interpolate image B is described here, for image A it is analogous. First, the light curve of image B is flux-corrected and time shifted

$$m_B(t) \rightarrow m'_B(t) = m_B(t + \Delta t) + \Delta m_{AB} \quad (3.5)$$

$\Delta m_{AB}$  is the magnitude correction. In the case of the Apache Point data, Colley et al. [34] give 0.125 mag in 1995 and 1997, but 0.158 mag in 1996. They explain that the different 1996 value is probably due to the realluminization of the mirror at the end of 1996, so that it became sensitive at the frequency of an emission line of the quasar [34].  $m'_B$  is then subtracted from the light curve of image A:

$$\Delta m(t) = m_A(t) - m'_B(t). \quad (3.6)$$

$\Delta m(t)$  is a measure for the deviation between the two light curves as a function of time. Since the light curve had been sampled only for discrete points in time, we have to interpolate between the two closest points of light curve B before and after the instant of time in which a point of light curve A had been determined (or vice versa):

$$m'_B(t_j) = c_i m'_B(t_i) + c_k m'_B(t_k), \quad (3.7)$$

where  $c_i = (t_k - t_j)/(t_k - t_i)$  and  $c_i + c_k = 1$  and  $t_i < t_j < t_k$ ;  $t_j$  indicates the time at which data was taken for image A, and  $t_i, t_k$  are the closest times before and after  $t_i$  for which data exists for image B. The difference light curve is defined as:

$$\Delta m(t_j) = m_A(t_j) - m'_B(t_j). \quad (3.8)$$

The measurement uncertainties  $\sigma(t_j)$  were added quadratically for each combined pair of data during interpolation and subtraction. The resulting difference light curves produced by interpolating either image A or B are shown in the three bottom panels of Fig. 3.3. The two difference light curves look rather similar.

We use 66 observations of image A and 81 observations of image B out of the 144 available observations from December 1994 to June 1998 since we have to restrict ourselves to the 343 days of “overlap” between the image A light curve and the time-shifted image B light curve. For simplicity, we will denote the three epochs of the difference light curve as the 1995, 1996 and 1997 epochs in the following. In detail, we have 160 data days coverage in 1995, 123 days in 1996 and 60 days in 1997.

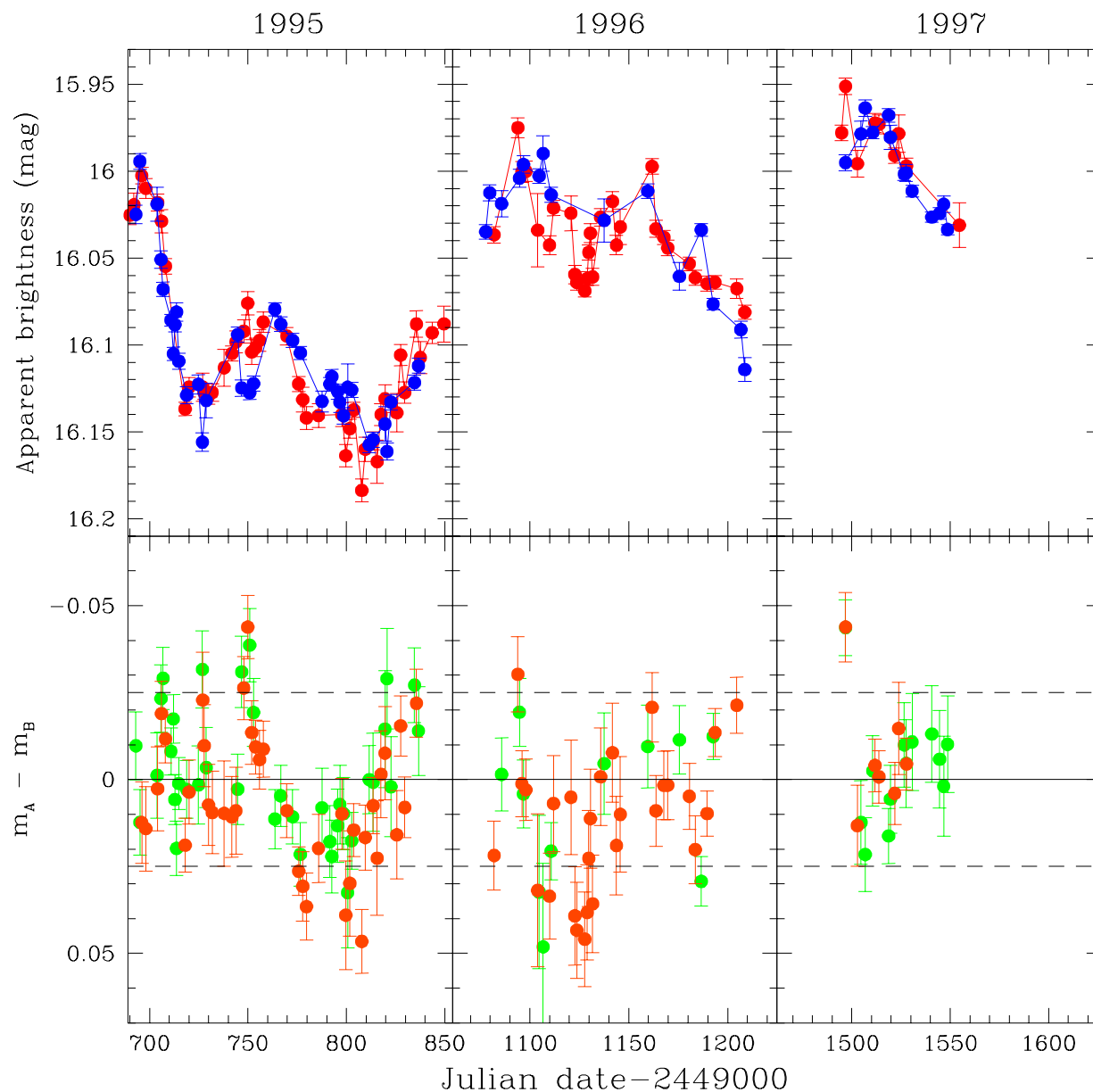


Figure 3.3: Light curve (upper panels) and difference light curve (lower panels) of the two images A (red) and B (blue) of the double quasar Q0957+561 in the  $g$ -band. The Julian dates show the days in 1995 (left panel), 1996 (middle panel) and 1997 (right panel) at which image A was observed. The data points of image B were obtained between 1996 and 1998, but have been shifted here in time by 417 days, and by 0.125 mag (1995,1997) and 0.158 mag (1996) in magnitude. The difference light curves were produced by linearly interpolating either image A (green points) or image B (orange points). To guide the eye, dashed lines are drawn at differences of +0.025 mag and -0.025 mag. We have only included data points that were interpolated. The light curve data were kindly made available to us by Ed Turner prior to publication. We only show the light curve where there is “overlap” between the data points of image A and the shifted data points of image B. The full Q0957+561 Apache Point Observatory light curve of both images from 1995 to 1998 with detailed information about the observations will be published by Colley, Turner & Kundić [34].

The time axis in Fig. 3.3 corresponds to the observing dates of image A. We detect no variation in the difference light curve with an amplitude greater than  $\approx 0.05 \pm 0.01$  in all three epochs.<sup>3</sup> There is also no systematic gradient apparent in the data, which would be the signature of a long term microlensing event, produced, for example, by a relatively massive MACHO.

The small variance can be quantified. We determine a  $\chi^2$  between the difference light curve and a horizontal line (corresponding to the hypothesis: no detectable microlensing-induced changes within the measurement uncertainties) defined by [140, pp. 660]:

$$\chi^2 = \frac{1}{N-1} \sum_{j=1}^N \frac{\Delta m^2(t_j)}{\sigma^2(t_j)}. \quad (3.9)$$

$N$  is the number of data points of the difference light curve. This  $\chi^2$ -value measures the goodness of representing the data with  $\Delta m = 0$ . We obtain  $\chi^2 = 1.8$  or  $\chi^2 = 1.9$ , depending on which of the image light curves was interpolated. Since ideally  $\chi^2$  would be one, this is an indication of the marginally significant deviations between the light curves of the two images, for example, around the days 750, 800, 1106 or 1490. In the second  $\chi^2$  value, the group of points around day 1125 also counts to this, but is likely to be just an interpolation effect since the values for images A and B agree rather well at the borders of the interpolation interval. The scatter of the data point between days 800 and 850 could even suggest that the error bars are perhaps a bit underestimated. In the first epoch of the Apache Point data [105], there is also a small peak seen around day 750 [105, 168]. It was seen by Schild [164] as well with independent data taken at a different observatory. This peak is also seen in the newly reduced Apache Point Observatory data [34] discussed here. It might be argued that the even smaller error bars in Fig. 3.3 now reveal a caustic crossing of the quasar. For such an event, a sudden jump in magnitude with following depression period is expected.

If real, such variations could be interpreted as small-amplitude microlensing events that betray the presence of compact objects with small masses in the light path. Such events would be rather exciting and could provide valuable information on the masses of possible objects in the halo of the lensing galaxy. By looking at the sequence of data points in Fig. 3.3, it is also possible to imagine weak trends in the difference light curve. Since we cannot prove with these data that any peaks or trends are real, we will argue that we do not detect any microlensing changes  $\Delta m_{\max} - \Delta m_{\min}$  higher than  $0.05 \pm 0.01$  mag in all three epochs. This way we include the possibility of such events, but we do not draw conclusions from them alone. In this context it can be seen that simulated microlensing light curves need to be sampled at the points where observational data are available because the observations might miss the days with higher magnifications.

---

<sup>3</sup>The amplitudes and the error bars are somewhat taken “by-eye”. For Gaussian fluctuations, one could use the full width at half maximum (FWHM) of the distribution of  $\Delta m(t_j)$  as an amplitude. Then, the expression  $\frac{1}{N-1} \sum_{j=1}^N \frac{\Delta m^2(t_j)}{\sigma^2}$  should be  $\approx 1$ , where  $\sigma$  is the standard deviation of the distribution of  $\Delta m(t_j)$  [140, pp. 660]. The expression is equal to unity for a FWHM of  $2.35 \times \sigma \approx 0.05$  for all three epochs. This is the value we use. The uncertainty of this amplitude is 0.01 mag, as determined by the error bars of the quasar photometry.

### 3.5.2 Simulating microlensing light curves

The exact shape of a microlensed quasar light curve depends on

- the masses of the MACHOs
- the size of the optical continuum emitting region of the quasar
- the direction of the projected relative velocity vector between lens and source and
- the projected relative positions of the MACHOs.

We do not and cannot know the exact positions of individual MACHOs in the lensing galaxy. Hence we will not be able to predict or explain an individual microlensed quasar light curve (as in the case of microlensing of stars in Magellanic Clouds). However, we can determine and analyze microlensed light curves in a statistical sense. In particular, we investigate here the distribution of total magnification variations.

We first determine the two-dimensional magnification variations due to microlensing at different positions in the source plane with Joachim Wambsganss' [190] ray-shooting code; light rays are followed backwards through an arrangement of MACHOs randomly distributed in a plane at the position of the lensing galaxy (see Fig. 2.4 on page 13 for a visualization of lens and source planes), with convergence and shear as given by the lensing model by Falco et al. [49] (see Sect. 3.4). The density of the deflected light rays in a plane at the position of the quasar corresponds to the relative magnification at this position [190].

In our simulations, we always use MACHOs with identical masses. We do not use more elaborate or realistic<sup>4</sup> mass distributions because they usually have a steep enough slope that most of the mass is contained in objects near the lower cut-off. In simulations with Salpeter-like mass functions [160], where the fraction  $dp$  of masses in a certain mass range  $dm$  is distributed as

$$dp \sim m^{-2.35} dm \quad (3.10)$$

between  $0.1 M_{\odot}$  and  $1.0 M_{\odot}$ , Lewis & Irwin [109] have found that the results of microlensing simulations are similar to those with all objects identical to the mean mass.

In our simulations we follow approximately  $10^{10}$  light rays and collect them in the source plane in an array of 2048 by 2048 pixels. This array is called “magnification pattern”. Parts of such patterns are shown in Fig. 3.4 in the three panels on the left. The three patterns all have the same physical side length (in lens and source plane), and contain roughly the same mass, but were generated with three different masses of the compact objects. In all three magnification patterns in Fig. 3.4 the quasar brightness profile was represented by a Gaussian with  $\sigma = 3 \times 10^{13}$  cm. The prominent features in the patterns are the caustics.

---

<sup>4</sup>In their PhD theses on microlensing, Wambsganss [190] and Witt [205] showed that no preferred, generally accepted, “true” mass function had been determined then. In April 1998, Stanke (priv. comm.) also finds that there is no single preferred mass function of stars. In the Trapezium cluster the mass function has a peak at  $0.3 M_{\odot}$ , but in other regions it is uncertain whether the mass functions have such a peak [161]. It is possible that there is no single mass function, but that it depends on the environment (Orion, Ophiuchus, Trapezium cluster, etc.).

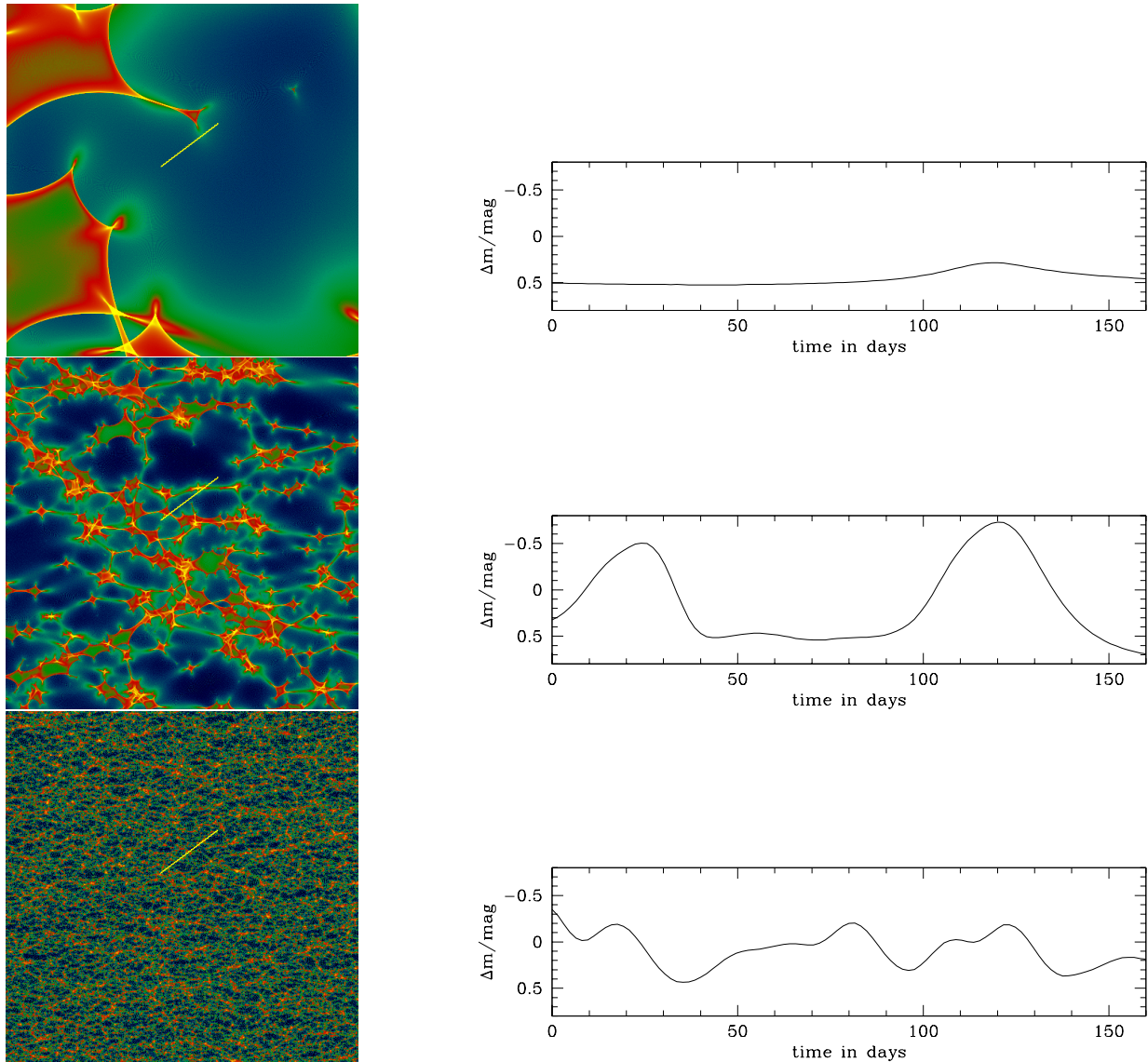


Figure 3.4: Magnification patterns and light curves for different MACHO masses. The three microlensing light curves on the right are simulated by evaluating the magnifications along the yellow tracks in the three magnification patterns on the left. The track length is chosen in such a way that it corresponds to a 160 day light curve of Q0957+561, such as the one observed at Apache Point Observatory in 1995, for an assumed transverse velocity of the quasar across the magnification pattern of  $v_t = 600 \text{ km s}^{-1}$ . The magnification patterns are colour-coded from yellow (high magnification) to blue (demagnification) and have side lengths of 4 Einstein radii (top), 40 Einstein radii (middle) and 400 Einstein radii (bottom), so that the (fixed) track length corresponds to MACHO masses of  $10^{-3} M_{\odot}$  (top),  $10^{-5} M_{\odot}$  (middle) and  $10^{-7} M_{\odot}$  (bottom). The quasar size (eq. (3.14)) is  $3 \times 10^{13} h_{60}^{-1/2} \text{ cm}$ .

The short straight yellow lines in the magnification patterns in Fig. 3.4 correspond to paths of the quasar through the quasar plane; we simulate microlensing light curves by evaluating the magnification along linear tracks across the magnification patterns [92, 190] with a physical length  $L$ , equal to the length the quasar traverses in the 865 day time span of the observed difference light curve shown in the bottom panels of Fig. 3.3. The light curves that result from the cuts through the magnification patterns in Fig. 3.4 are shown in the three panels on the right. It can be seen that the magnitude changes are strongest when the quasar comes close to or crosses caustic lines. In order to mind the gaps between the difference light curve data points, we mimic the observations more closely by only using points on the tracks across the magnification patterns that correspond to days where we have points in our difference light curve (Fig. 3.3).

For the length  $L$  of the cuts we need an estimate for the effective transverse velocity  $v_t$  of the source across the magnification pattern. The effective transverse velocity  $v_t$  is the sum of the projected motions of the source  $v_s$ , the lensing galaxy  $v_d$  and the observer  $v_{\text{obs}}$  according to the formula [92]

$$\begin{aligned} v_t &= \frac{1}{1+z_s} v_s - \frac{1}{1+z_d} \frac{D_s}{D_d} v_d + \frac{1}{1+z_d} \frac{D_{\text{ds}}}{D_d} v_{\text{obs}} \\ &= 0.41 v_s - 1.03 v_d + 0.62 v_{\text{obs}}, \end{aligned} \quad (3.11)$$

where in the last line the values for Q0957+561 in the standard  $\Omega = 1$ ,  $\Lambda = 0$  cosmological model we use throughout this thesis (Sect. 2.3) were inserted. Following Witt & Mao [207], who did this calculation for the quadruple quasar Q2237+0305, we can estimate  $v_{\text{obs}}$  and  $v_d$  (without taking the transverse component) from local observations, but  $v_s$  will remain an unknown. For the sun's motion relative to the cosmic microwave background radiation they used the result by Kogut et al. [98], who obtained  $369.5 \pm 3.0 \text{ km s}^{-1}$  in the direction defined by the Galactic coordinates  $l = 264.4 \pm 0.3$ ,  $b = 48.4 \pm 0.5$ . The angle between the sun's motion and Q0957+561 is  $64.6^\circ$ , so that we get  $\approx 330 \text{ km s}^{-1}$  for the transverse component of the sun's motion relative to the microwave background. The peculiar velocity of the lensing galaxy is much more uncertain, typical values range from 100-400  $\text{km s}^{-1}$  (Witt & Mao quote Mould et al. [118], Tormen et al. [181] and references therein). From these values, we obtain transverse velocities up to  $v_t = 600 \text{ km s}^{-1}$ .

By assuming this projected quasar velocity relative to the magnification pattern the length  $L$  that is traversed by the quasar in 865 days is given by

$$L = 600 \text{ km s}^{-1} \times 865 \text{ days} = 4.5 \times 10^{15} \text{ cm}. \quad (3.12)$$

We have neglected any motion of the MACHOs relative to each other. Since velocities of stars in galaxies are in general smaller than galaxy velocities, this effect cannot dominate the bulk velocities. It merely slightly increases the value of the effective transverse velocity of the quasar [104, 192].

### 3.5.3 MACHO mass and quasar size

We analyzed magnification patterns for both quasar images. We considered three cases: all the surface mass density is contained in MACHOs, 50% is contained in MACHOs, or 25% is con-



tained in MACHOs. For each of these mass fractions, magnification patterns of varying physical side lengths of 16, 160 and 1600 Einstein radii were considered. In addition, we used three different realizations of the magnification patterns for each set of parameters in order to estimate the statistics. In total, 54 different magnification patterns were produced for these calculations.

From eq. (2.25), the Einstein radius in the case of Q0957+561 is

$$r_E = 4.8 \times 10^{16} \sqrt{\frac{M}{M_\odot}} h_{60}^{-1/2} \text{ cm} = 1.5 \times 10^{-2} \sqrt{\frac{M}{M_\odot}} h_{60}^{-1/2} \text{ pc} \quad (3.13)$$

From this expression, one can see that a single magnification pattern can be used to simulate light curves for various MACHO masses because the physical length scales with the square root of the mass of the MACHOs<sup>5</sup>; the fixed length the quasar traverses in the source plane translates into different numbers of pixels for different MACHO masses and pattern sizes. The only limitation we have for the investigation of various microlensing masses is the dynamic range of the magnification pattern, which in our case is an array of 2048 by 2048 pixels. To simulate the duration of all three observing epochs, we used four different track lengths of 16, 50, 159 and 502 pixels, corresponding to the track length (3.12) for different MACHO masses, which were then evaluated at the points corresponding to the data points in the difference light curve. With these light curves, we were able to simulate three orders of magnitude of MACHO masses with one pattern. With the three different side lengths, however, it was possible to investigate the effects of MACHO masses  $M$  ranging from  $10^{-7}M_\odot$  up to  $1M_\odot$  (in steps of factor 10). Due to the “overlap” we were able to check some masses on magnification patterns with different side lengths and hence cross-check the results.

It follows from these considerations that the quasar traverses more (fewer) characteristic lengths of the magnification pattern for smaller (larger) MACHO masses in each of the three observations epochs we have data for. This implies that the light curve is more (less) variable for smaller (larger) MACHO masses, so that one can derive limits on the MACHO masses from the microlensing variability. This is illustrated for three different mass scales in Fig. 3.4; the variability of the microlensing light curves increases strongly with decreasing MACHO mass. Qualitatively one can take from the magnification patterns in Fig. 3.4 that the probability of observing no microlensing variation during the 1995 epoch is practically zero for  $10^{-7}M_\odot$  MACHOs (bottom panel) whereas for the  $10^{-3}M_\odot$  MACHOs (top panel) this is not unlikely. These qualitative statements will be quantified in the next section.

The size of the optical continuum region of the quasar, which will be called “quasar size” in the following, has an impact on the shape of a light curve. For extended objects the total magnification can be calculated as a weighted mean of the magnifications at many points in the source plane. In practice, the effect of the source size can be accounted for by convolving the two-dimensional magnification pattern with an appropriate source profile. Sharp features

---

<sup>5</sup>An easy way to understand this “scaling argument” without invoking the concept of an “Einstein radius” is as follows: Consider a certain region in the source plane. Suppose that we know the surface mass density of the MACHOs in the lens plane. Let us raise the mass of all MACHOs by a factor  $q$ . If the surface mass density is kept constant in the lens plane, this corresponds to blowing up the length scale of the distribution of MACHOs by a factor  $\sqrt{q}$ . Since the deflection angle is proportional to the mass and inversely proportional to the distance to the lens, the magnification pattern in the source plane is thus also blown up by the same factor of  $\sqrt{q}$ .

in the magnification pattern – especially the line-like caustics – are thus smoothed out by the brightness profile of the quasar. The magnitude changes during caustic crossings can be very abrupt for small sources ( $\lesssim 0.01$  Einstein radii), but become smooth for larger sources. The amplitude (smaller for large sources) and the duration (longer for large sources) of variations in a microlensing light curve hence depends on the source size [193].

We adopted a circular Gaussian profile for the surface brightness profile  $i(\theta)$  of the quasar, where the source size is defined by the Gaussian width  $\sigma_Q$ :

$$i(\theta) \sim e^{-\frac{\theta^2}{2\sigma_Q^2}}. \quad (3.14)$$

Each of the 54 magnification patterns was convolved with this surface brightness profile with source sizes ranging from  $\sigma_Q = 10^{14} h_{60}^{-1/2}$  cm up to  $\sigma_Q = 3 \times 10^{15} h_{60}^{-1/2}$  cm (in steps of  $\sqrt{10}$ ). These quasar sizes are smaller than or of the order of one light day, which is the upper limit on the quasar size that was obtained from the analysis of the microlensing variations of Q2237+0305 for lens masses around a few tenths of a solar mass [194, 198, 207] (Sect. 3.3.1). The case for even larger quasar sizes and smaller MACHO masses was examined by Refsdal & Stabell [147, 148] and Haugan [67].

From eq. (3.13) it can also be taken that all our results for MACHO masses may be scaled quadratically with  $v_{600} = v_t/600 \text{ kms}^{-1}$  for various values  $v_t$  of the transverse source velocity because the scale of the magnification pattern is proportional to the square root of the MACHO masses. Similarly, the source sizes scale linearly with  $v_{600}$ .

### 3.5.4 Light curve logistics

For each set of the two parameters MACHO mass  $m$  and quasar size  $\sigma_Q$ , and for each of the two quasar images A and B, we analyzed 100 000 randomly chosen linear tracks across the magnification patterns at the points that correspond to the dates in the difference light curve in Fig. 3.3 where we have observations. The same tracks were used for different source sizes.

We combine the tracks from both quasar images under the assumption that there is no correlation between the variations in the images: for each quasar image and light curve we determined the difference between the highest and the lowest point of the light curve  $\Delta m_{\max} - \Delta m_{\min}$  that would have been observed given the sampling of the observations. We call this quantity the total magnitude variation of the light curve. We then combine the probability distributions of the total magnitude variations in each image statistically to yield a joint probability distribution of the total magnitude variations in the observed difference light curve of Q0957+561.

For the simulated light curves, we can calculate for each observing epoch the probability  $p_{>d}$  of observing a total variation greater than or equal to some value  $d$  for each analyzed parameter pair of MACHO mass and quasar size. As an example, in Fig. 3.5 the integrated probability distributions  $p_{>d}$  for the 1995 epoch are shown for MACHOs of mass  $10^{-1}M_\odot$  and  $10^{-5}M_\odot$ . In these plots, it is assumed that the quasar has a size of  $2 \times 10^{14} h_{60}^{-1/2}$  cm and that the halo mass is completely made up of MACHOs. Three lines are shown per plot; the distributions for images A and B alone, as well as the joint probability distribution

$$p_{>d,AB} = 1 - (1 - p_{>d,A})(1 - p_{>d,B}) \quad (3.15)$$

where at least one quasar image has a total variation greater than  $d$ . One can see that much stronger microlensing variations are expected for small MACHO masses than for large masses on these short time scales.

We approximate the probability to observe a total variation greater than  $d \pm \Delta d$  mag from the average  $\bar{p}_{>d}$  of the three probabilities  $p_{>d-\Delta d}$ ,  $p_{>d}$ , and  $p_{>d+\Delta d}$ . We write for three probabilities  $p_i$

$$\bar{p}_{>d} = \frac{1}{3} \sum_{i=1}^3 p_i, \quad \Delta \bar{p}_{>d} = \sqrt{\frac{1}{2} \sum_{i=1}^3 (p_i - \bar{p}_{>d})^2}. \quad (3.16)$$

We obtain such a probability for each set of three epochs. Since we also have three different realizations of each magnification pattern, we combine the three  $\bar{p}_{>,m}$  to determine the statistical uncertainties involved in the choice of the magnification pattern:

$$\tilde{p}_{>} = \frac{1}{3} \sum_{m=1}^3 \bar{p}_{>,m}, \quad \Delta \tilde{p}_{>} = \frac{1}{3} \sqrt{\sum_{m=1}^3 (\Delta \bar{p}_{>,m})^2}. \quad (3.17)$$

Finally, we find for the joint probability  $\tilde{p}_{AB}$  that at least one quasar image has a total variation greater than the  $d_i$  in at least one epoch  $i$

$$\tilde{p}_{>,AB} = 1 - (1 - \tilde{p}_{>,A}) (1 - \tilde{p}_{>,B}), \quad (3.18)$$

with an uncertainty

$$\Delta \tilde{p}_{>,AB}^2 = [\Delta \tilde{p}_{>,B} (1 - \tilde{p}_{>,A})]^2 + [\Delta \tilde{p}_{>,A} (1 - \tilde{p}_{>,B})]^2. \quad (3.19)$$

In the following,  $p_{>}$  will simply refer only to the joint probability calculated in eq. (3.18). If we apply the limit on the total magnitude variation  $d$  of the three observing epochs from Fig. 3.3 in Sect.3.5.1,  $p_{>}$  can be viewed as the confidence level at which we can exclude a particular parameter pair as not consistent with the observations.

## 3.6 Results

The values for the exclusion probability  $p_{>}$  for various parameter pairs of MACHO mass  $m$  and quasar size  $\sigma_Q$  are given in Tables 3.1 (for an assumed halo fraction of the MACHOs of 100%), 3.2 (for a halo fraction of 50%), and 3.3 (for a halo fraction of 25%). The table entries for parameter pairs that are ruled out at a confidence level of 99% and above are highlighted in grey. The parts without entries are regions in the parameter space which we were not able to access because they were beyond the dynamical range of our simulations.

The results from Table 3.1 are illustrated in Fig. 3.6. In this Figure the confidence levels are represented by the height and the colour of the plotted bars. The numbers from this plot and Tables 3.1, 3.2 and 3.3 show that MACHO masses in the region from  $10^{-3} M_\odot$  down to  $10^{-5} M_\odot$  can be ruled out to make up a sizeable fraction of the halo mass in the lensing galaxy

Table 3.1: Probabilities  $p_>$  (in percent) for measuring a total microlensing variation greater than observed in the Apache Point Observatory difference light curve of Q0957+561 (Fig. 3.3). In this table, it is assumed that MACHOs constitute 100% of the halo mass. The probabilities were calculated using magnification patterns with three different side lengths (the three main columns on the right) for several combinations of MACHO mass and quasar size (indicated in the two columns on the left). No values are given where the parameters were beyond the dynamical range of the simulations. The statistical uncertainties are given in brackets (0.0 is given where the uncertainty was below the rounding precision). Probabilities above 99% are highlighted in grey – the respective parameter pairs are ruled out by the observations at the 99% level. The table is continued on page 37.

Macho mass ( $M_\odot$ )	Quasar size (cm)	pattern side length (Einstein radii)		
		16	160	1600
1	$10^{14}$			
	$3 \times 10^{14}$	53.0(2.1)		
	$10^{15}$	57.6(2.1)		
	$3 \times 10^{15}$	45.5(4.6)		
$10^{-1}$	$10^{14}$	85.2(2.4)		
	$3 \times 10^{14}$	86.5(2.1)		
	$10^{15}$	87.2(2.3)		
	$3 \times 10^{15}$	72.5(5.9)		
$10^{-2}$	$10^{14}$	99.9(0.1)		
	$3 \times 10^{14}$	99.9(0.0)	99.9(0.1)	
	$10^{15}$	99.9(0.1)	99.8(0.1)	
	$3 \times 10^{15}$	81.7(6.1)	79.0(7.0)	
$10^{-3}$	$10^{14}$	100.0(0.0)	100.0(0.0)	
	$3 \times 10^{14}$	100.0(0.0)	100.0(0.0)	
	$10^{15}$	100.0(0.0)	100.0(0.0)	
	$3 \times 10^{15}$		55.9(10.6)	
$10^{-4}$	$10^{14}$		100.0(0.0)	
	$3 \times 10^{14}$		100.0(0.0)	100.0(0.0)
	$10^{15}$		99.9(0.1)	99.9(0.0)
	$3 \times 10^{15}$		0.5(0.5)	0.8(0.9)

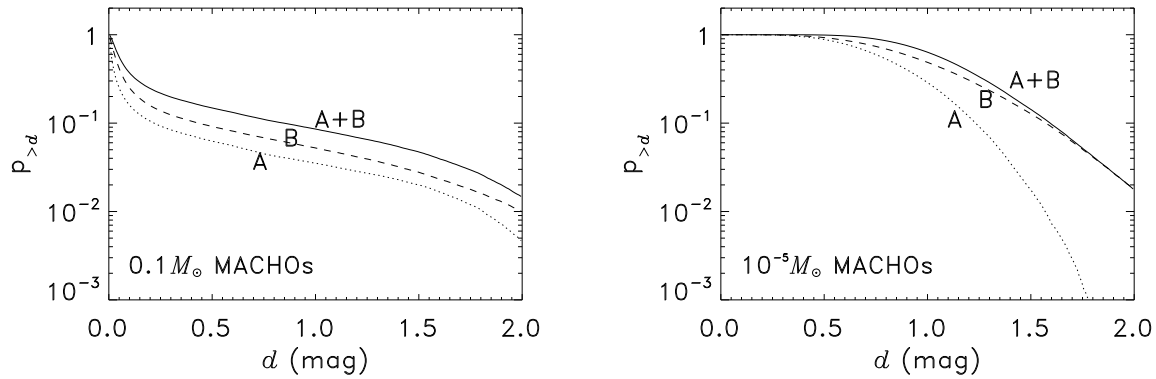


Figure 3.5: The probability  $p_{>d}$  of observing a microlensing variation greater than  $d$  in the quasar Q0957+561 in the epoch 1995 either in image A (dotted line), image B (dashed line) or in at least one of the two images (solid line). In the panel on the left the MACHO mass is  $0.1 M_{\odot}$ , whereas in the panel on the right it is  $10^{-5} M_{\odot}$ . In both panels the quasar size is  $2 \times 10^{14}$  cm and it is assumed that the halo is completely made up of MACHOs.

Table 3.1: (continued from page 36)

Macho mass ( $M_{\odot}$ )	Quasar size (cm)	pattern side length (Einstein radii)		
		16	160	1600
$10^{-5}$	$10^{14}$		100.0(0.0)	100.0(0.0)
	$3 \times 10^{14}$		100.0(0.0)	100.0(0.0)
	$10^{15}$		71.2(9.4)	69.0(9.8)
	$3 \times 10^{15}$			0.0(0.0)
$10^{-6}$	$10^{14}$			100.0(0.0)
	$3 \times 10^{14}$			100.0(0.0)
	$10^{15}$			2.1(2.0)
	$3 \times 10^{15}$			0.0(0.0)
$10^{-7}$	$10^{14}$			100.0(0.0)
	$3 \times 10^{14}$			71.9(11.8)
	$10^{15}$			0.0(0.0)
	$3 \times 10^{15}$			0.6(0.7)

Table 3.2: Same as Table 3.1 for the case where 50% of the halo mass is contained in MACHOs.

Macho mass ( $M_{\odot}$ )	Quasar size (cm)	pattern side length (Einstein radii)		
		16	160	1600
1	$10^{14}$			
	$3 \times 10^{14}$	36.3(3.1)		
	$10^{15}$	37.6(2.5)		
	$3 \times 10^{15}$	34.5(3.5)		
$10^{-1}$	$10^{14}$	76.7(4.4)		
	$3 \times 10^{14}$	74.9(3.7)		
	$10^{15}$	75.6(3.7)		
	$3 \times 10^{15}$	65.2(6.3)		
$10^{-2}$	$10^{14}$	99.4(0.2)		
	$3 \times 10^{14}$	99.5(0.2)	99.2(0.3)	
	$10^{15}$	99.5(0.2)	99.3(0.3)	
	$3 \times 10^{15}$	80.3(6.2)	77.6(7.1)	
$10^{-3}$	$10^{14}$	100.0(0.0)	100.0(0.0)	
	$3 \times 10^{14}$	100.0(0.0)	100.0(0.0)	
	$10^{15}$	100.0(0.0)	99.9(0.0)	
	$3 \times 10^{15}$		35.7(11.1)	
$10^{-4}$	$10^{14}$		100.0(0.0)	
	$3 \times 10^{14}$		100.0(0.0)	100.0(0.0)
	$10^{15}$		99.5(0.3)	99.7(0.2)
	$3 \times 10^{15}$		0.0(0.0)	0.1(0.1)
$10^{-5}$	$10^{14}$		100.0(0.0)	100.0(0.0)
	$3 \times 10^{14}$		100.0(0.0)	100.0(0.0)
	$10^{15}$		37.2(11.3)	38.0(11.8)
	$3 \times 10^{15}$			0.0(0.0)
$10^{-6}$	$10^{14}$			100.0(0.0)
	$3 \times 10^{14}$			99.5(0.4)
	$10^{15}$			0.1(0.2)
	$3 \times 10^{15}$			0.0(0.0)
$10^{-7}$	$10^{14}$			100.0(0.0)
	$3 \times 10^{14}$			31.4(12.7)
	$10^{15}$			0.0(0.0)
	$3 \times 10^{15}$			0.0(0.0)

Table 3.3: Same as Table 3.1 for the case where 25% of the halo mass is contained in MACHOs.

Macho mass ( $M_{\odot}$ )	Quasar size (cm)	pattern side length (Einstein radii)		
		16	160	1600
1	$10^{14}$			
	$3 \times 10^{14}$	18.8(1.9)		
	$10^{15}$	19.8(1.9)		
	$3 \times 10^{15}$	19.7(2.2)		
$10^{-1}$	$10^{14}$	52.8(5.1)		
	$3 \times 10^{14}$	52.9(5.0)		
	$10^{15}$	54.1(4.9)		
	$3 \times 10^{15}$	49.0(6.3)		
$10^{-2}$	$10^{14}$	96.3(1.3)		
	$3 \times 10^{14}$	96.5(1.2)	96.0(1.2)	
	$10^{15}$	96.7(1.1)	96.3(1.1)	
	$3 \times 10^{15}$	70.0(7.7)	65.4(9.0)	
$10^{-3}$	$10^{14}$	100.0(0.0)	100.0(0.0)	
	$3 \times 10^{14}$	100.0(0.0)	100.0(0.0)	
	$10^{15}$	99.9(0.1)	99.7(0.2)	
	$3 \times 10^{15}$		16.0(7.8)	
$10^{-4}$	$10^{14}$		100.0(0.0)	
	$3 \times 10^{14}$		100.0(0.0)	100.0(0.0)
	$10^{15}$		97.1(1.6)	98.1(1.1)
	$3 \times 10^{15}$		0.0(0.0)	0.0(0.0)
$10^{-5}$	$10^{14}$		100.0(0.0)	100.0(0.0)
	$3 \times 10^{14}$		100.0(0.0)	100.0(0.0)
	$10^{15}$		14.5(6.2)	11.8(7.1)
	$3 \times 10^{15}$			0.0(0.0)
$10^{-6}$	$10^{14}$			100.0(0.0)
	$3 \times 10^{14}$			94.0(3.9)
	$10^{15}$			0.0(0.0)
	$3 \times 10^{15}$			0.0(0.0)
$10^{-7}$	$10^{14}$			100.0(0.0)
	$3 \times 10^{14}$			6.2(4.7)
	$10^{15}$			0.0(0.0)
	$3 \times 10^{15}$			0.0(0.0)

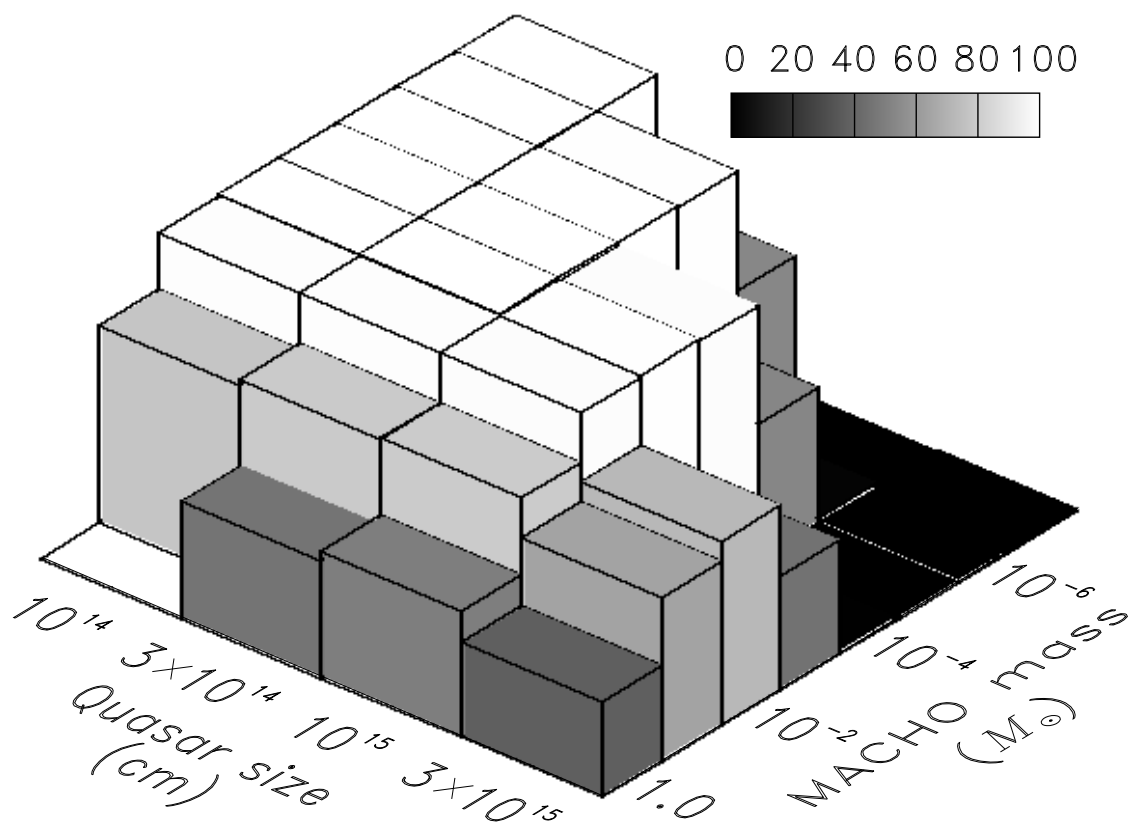


Figure 3.6: “Exclusion” probability (in percent) for certain MACHO masses. Three-dimensional visualization of the probabilities  $p_{>}$  (in percent) measuring a total microlensing variation greater than observed in the 1995-97 Apache Point Observatory difference light curve of Q0957+561 (Fig. 3.3) for a particular parameter pair of MACHO mass and quasar size. The probabilities are indicated by the grey-shade of the bars (see the key), the relative scale is visualized by the bar height. The parameters of the blank field were beyond the dynamical range of our simulations. These probabilities are those from Table 3.1 for the largest available magnification pattern for each parameter pair. It is assumed that MACHOs make up 100% of the halo mass.



of Q0957+561 for quasar sizes smaller than  $3.2 \times 10^{14} h_{60}^{-1/2}$  cm. For quasar sizes smaller than  $10^{14} h_{60}^{-1/2}$  cm, we can even exclude MACHO masses down to  $10^{-7} M_{\odot}$ .

When looking at the uncertainties of the given probabilities in Tables 3.1, 3.2 and 3.3 we find relatively good agreement between the results from the three independent realizations. Note that the error bars are usually not smaller for the larger magnification patterns. This indicates that the error bars are dominated by the uncertainty of 0.01 mag of the total magnitude variation, rather than by the field to field variations.

### 3.7 Discussion and conclusion

In four years of observational data on the gravitationally lensed double quasar Q0957+561 by Colley et al. [34] no microlensing variation of the quasar larger than 0.05 magnitudes was observed. From microlensing simulations we find that this rules out a dominant population of compact objects in the halo of the lensing galaxy from  $10^{-2} M_{\odot}$  down to  $10^{-5} M_{\odot}$  for quasar sizes below  $3.2 \times 10^{14} h_{60}^{-1/2}$  cm. These limits hold for fractions of the halo mass contained in compact objects down to 50%.

These results are consistent with the 5 year results from the MACHO microlensing search towards the Magellanic clouds (Alcock et al. [5]). Probable masses of MACHOs in the Milky Way that emerge from their study lie around a few tenths of a solar mass, which is consistent with our results. In fact, such large masses are not yet probed by the observational data set we used [34] because microlensing effects by objects with masses of a few tenths of a solar mass are only becoming observable on time-scales of several years. In the 17 year Q0957+561 data set used by Pelt et al. [135], a dip with an amplitude of about 0.3 mag was seen in the difference light curve  $m_A - m_B$ , with a minimum at the end of 1982. It is very plausible that this dip corresponds to a several year long microlensing event in image B [149]. Such events, however, warrant a more detailed analysis than the total magnitude variation technique discussed in this chapter. Possible avenues for such analyses will be discussed in the next chapter.

The limits on compact objects in the halo of the lensing galaxy of Q0957+561 improve with time since the monitoring of Q0957+561 at the Apache Point Observatory (and also at other observatories) is an ongoing project. The limits derived in this chapter, for example, became more stringent by an order of magnitude when we used three epochs instead of only one epoch because the Einstein radius scales with the square root of the MACHO masses.

In quasar microlensing, not only the mass of MACHOs, but also the size of the quasar enters the calculations. With the current data, however, we cannot constrain the quasar size very much. To do this, one would need to find characteristic events in the difference light curve of the two quasar images. If the marginal variations detected in Fig. 3.3, the “trends” in the difference light curve, or the reported “peak” in the difference light curve [105, 164] in Fig. 3.3 around day 750 were real, they could be valuable constraints for both the masses of MACHOs and the quasar size. Low-magnitude variations with sudden changes of about 0.05 mag in less than 10 days would indicate small masses of the MACHOs of much less than a solar mass. Precise values, however, depend on the assumptions about the halo fraction of these objects and the quasar size.

# Chapter 4

## Independent evidence for Microlensing in Q2237+0305

### 4.1 Microlensing in Q2237+0305

It was shown in the last chapter that one needs long light curves of multiply imaged quasars in order to get reliable results and good limits from the microlensing effect. In this chapter, we present the reduction of a set of data that was obtained at the Apache Point Observatory between June 1995 and January 1998, the same period during which the Q0957+561 data we discussed in the last chapter were obtained.

The quadruple quasar Q2237+0305 was discovered during the Center for Astrophysics (CfA) redshift survey, which was announced by Huchra et al. [78] in 1985. In high-resolution images of the system, four quasar images are seen in a cruciform geometry around the core of a spiral galaxy. Due to its geometry this system is known as the Einstein cross. In Fig. 2.3, an Hubble Space Telescope (HST)  $V$ -band image of the lensing galaxy and the quasar is shown. In Fig. 4.1 a close-up of the central region with the 4 quasar images, denoted A, B, C and D, is shown. The central brightness peak is the galaxy core. All quasar images have a separation of about 0.9 arcsec from the galaxy centre. The spiral galaxy has a redshift  $z = 0.0394$ . The quadruple nature of the lens was actually recognized a bit later by Schneider et al. [169] and Yee [220]; at first only one source [78], and later 3 images were known [182].

Very quickly after its discovery, it was realised that this system is an ideal case for microlensing studies (for example Kayser & Refsdal [93]). And indeed, in 1989 the discovery of microlensing in this system was announced by Irwin et al. [81]. There are several reasons why this galaxies is extremely well suited to microlensing studies: the surface mass density is high, so that microlensing is to be expected, and the spiral galaxy is a factor of ten closer than the quasar, which lets us probe the mass distribution at about half a kpc from the galaxy centre.

Moreover, microlensing variations should be happening more frequently since the projected transverse velocity of the galaxy in the source plane should be large ( $> 1000 \text{ km s}^{-1}$  [207]) because the proximity of the galaxy implies a large leverage. As noted by Wes Colley (1999, priv. comm.), one should notice, however, that this would not be true for a fixed scale in the

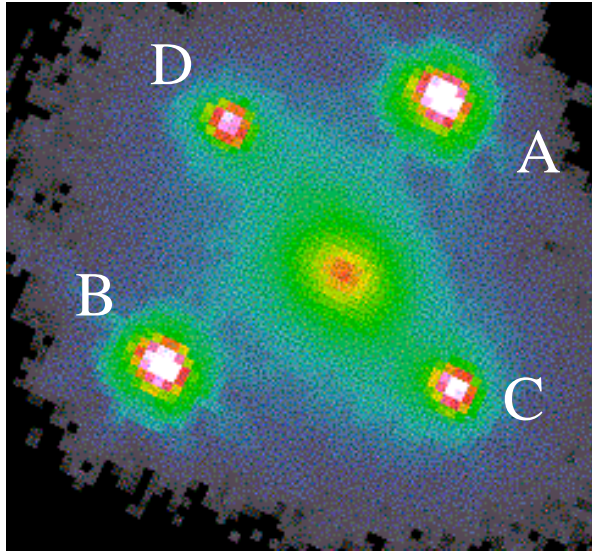


Figure 4.1: The gravitational lens system Q2237+0305 observed with the Hubble Space Telescope in the  $V$ -band. The separation of the quasar images from the galaxy centre is about 0.9 arcsec. This image is a close-up of the galaxy centre of Fig. 2.3 that was rotated.

galaxy  $\Delta l$  since both the galaxy velocity and the scale  $\Delta l$  are projected into the source plane with the same factor. The microlensing variations will nevertheless be more frequent because, due to the relative distances involved, the physical length of an Einstein radius

$$r_E = \sqrt{\frac{4GM}{c^2} \frac{D_{ds}D_d}{D_s}} = 1.8 \times 10^{16} \sqrt{\frac{M}{M_\odot}} h_{60}^{-1/2} \text{ cm}, \quad (4.1)$$

(with the definitions from eq. (2.25)) in the lens plane of Q2237+0305 is only about half as large as in the case of Q0957+561 ( $r_E = 3.4 \times 10^{16} \sqrt{M/M_\odot} h_{60}^{-1/2} \text{ cm}$ ), for example. The quasar moves more rapidly through magnification patterns with a fixed side length in Einstein radii in the case of Q2237+0305 than for lens galaxies at higher redshifts (with the same transverse velocity).

The challenge with Q2237+0305 is to measure the brightness of the four images individually with high accuracy. In observations with seeing above an arcsecond, it is very difficult to disentangle the four quasar images, the galaxy core, and other features of the galaxy (such as the bar-like structure that is situated across the galaxy centre [220, 167]). With the announcement of the first microlensing event in 1989 by Irwin et al. [81], the record of semi-regular observations of Q2237+0305 began. Corrigan et al. [39] published the “initial light curve”, that was later augmented by other individual and systematical observations [136, 76]. Wambsganss [195] emphasized that without regular sampling, it would be difficult to extract useful information from the microlensing observations. Moreover, the sample of early observations with good seeing is rather heterogeneous regarding the filters chosen, so that the interpretation is made more difficult since the filter differences have to be calibrated out.

In 1996, Østensen et al. [125] presented five years of observations of the system from the Nordic Optical Telescope (NOT). In all four images, variations had then been detected. Of the particularly interesting “events” until 1997 we should mention the Irwin et al. peak in 1989 of  $\gtrsim 0.2$  mag amplitude and less than 100 days duration, which according to Racine [141] may be the first half of a double peak of which only the following slope down, but not the second peak, was observed. Rather striking was the drop of about a magnitude in 1992 (with a large uncertainty) within  $\approx 20$  days found by Pen et al. [136] on the basis of observations made at the Apache Point Observatory. Although it is not an “event”, we should also mention here that Lewis et al. [109] found spectroscopic evidence for microlensing of the broad line region of the quasar.

Recently, the OGLE team has presented a light curve [209] covering about 600 days in 1997 and 1998. The most recent light curve contains data from 1999 and can be looked at at [www.astro.princeton.edu/~ogle/ogle2/huchra.html](http://www.astro.princeton.edu/~ogle/ogle2/huchra.html). The OGLE light curve is very well sampled and shows amazing brightness variations in all four quasar images with high amplitudes of the order of a magnitude. Especially, image C showed a dramatic brightness peak of about 1.2 magnitudes in 1999 that was resolved by the OGLE data in beautiful detail. The interpretation of these data, however, is still in the beginning. The Melbourne/Princeton group around Stuart Wyithe, Rachel Webster and Ed Turner, has recently started to analyze the available 15 year brightness record of the Einstein cross from various points of view in a series of papers [211, 212, 213, 214, 215, 216, 217, 218, 219]. Using a new microlensing code that generalizes methods by Witt [206] and Lewis et al. [108] to large sources, they compared the observed distribution of light curve derivatives with theoretical predictions and constrained the most likely projected transverse velocity of the lensing galaxy to be less than  $500 \text{ km s}^{-1}$ . This is a relatively small value for this system, well below the lower estimate of  $1000 \text{ km s}^{-1}$  by Witt & Mao [207] quoted above. In the following papers, Wyithe et al. proceeded to analyze the observed light curve record with special emphasis on the likely source size of the quasar, finding evidence for a small size of the continuum emitting region of less than two percent of the Einstein radius of the microlenses. For  $0.3 M_{\odot}$  stars, this corresponds to  $1.1 \times 10^{15} \text{ cm}$ , which is about the same limit that was obtained earlier by Wambsganss et al. [194] and Webster et al. [198] on the basis of the Irwin et al. peak (Sect. 3.3.1). The most recent papers [218, 219] study the actual shape of the OGLE light curves in comparison with microlensing models and actually predict a future microlensing peak in image C. They also discuss a method to identify brightness variations in observed light curves that promise to become high-magnification microlensing events.

## 4.2 Pushing the limits: Q2237+0305 at Apache Point Observatory

We describe here the analysis of data that were taken with the 3.5 m telescope at Apache Point Observatory (APO) from June 1995 to January 1998 as part of the Princeton-APO lens monitoring program. We restrict ourselves to the  $r$ -band data. The corresponding CCD has a pixel size of  $0.6''$ , whereas the pixel size in the  $g$ -band is only  $1''$ . In Table 4.1, the observation log is given.

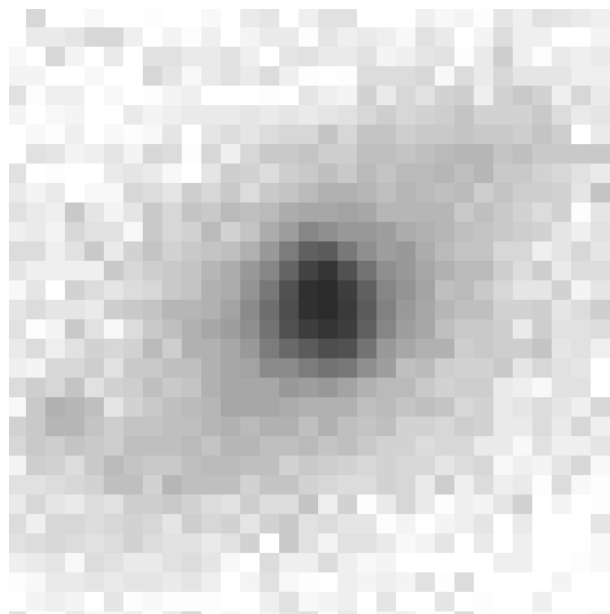


Figure 4.2: Image of the central  $18.6 \times 18.6$  arcsec of the lensing galaxy 2237+0305 in the  $r$ -band. The image was taken at APO on 20 November 1996 under  $1.2''$  seeing. This figure is a closeup of Fig. 4.3.

The images were taken under variable, often poor seeing conditions between  $1.2$  and several arcseconds. We have neglected frames with seeing worse than  $2.4''$  (4 pixels).<sup>1</sup> The distance between two quasar images is only three pixels. In these frames, the four quasar images, the galaxy core, and the remaining light from the galaxy are contained within only a dozen or so pixels, which is fairly coarse compared to the number of sources in this area. In Fig 4.2, a plot is shown of the centre of a frame obtained on 20 November 1996 under  $1.2''$  seeing. At face value, nothing of the detailed quasar image and galaxy structure of Fig. 4.1 can be seen except for a generic central light concentration.

Fortunately, we know the exact quasar image positions relative to the galaxy centre from HST observation in the UV [22] with an accuracy of a few milli-arcseconds. Moreover, a detailed model of the galaxy light distribution is available [166] that was obtained from the analysis of HST images as well. With the help of these strong constraints, we are able to do photometry for the two brighter quasar images A and B. First, we describe our reduction technique and fitting procedure in Sect. 4.3. Then we present the light curve we obtain for images A and B in Sect. 4.4.

---

<sup>1</sup>The seeing values in Table 4.1 were determined with a different routine than the ones with which we rejected the frames, so that in a couple of cases larger seeing values can occur. This was necessary because we needed different software to detect the reference star pattern than to do the photometry. Also, the seeing values in this table were determined from stacked frames. Small stacking errors can increase the seeing values slightly.

Table 4.1: Observation log of the  $r$ -band observations of Q2237+0305 at Apache Point Observatory from 1995 to 1998. The table contains the date in yymmdd format, the Julian date (-2449000), the total exposure time of all exposures in a given night, the seeing as determined from reference star 3 in the stacked images of Scheme A, and the magnitude estimates for two reduction schemes A and B (see Sect. 4.3) with  $1\sigma$  errors in brackets (first two digits after the decimal point). The magnitudes are given with respect to the measured magnitude for image A on 20 November 1996.

date	Julian date	total exposure time per night (seconds)    seeing (pixel)		<i>Scheme A</i>		<i>Scheme B</i>	
				image A (mag)	image B (mag)	image A (mag)	image B (mag)
950602	871	45	3.4	0.57 (0.15)	0.66 (0.17)	0.34 (-)	0.62 (07)
950604	873	840	3.1			0.23 (-)	0.48 (04)
950606	875	300	3.6	0.42 (0.20)	0.80 (0.13)		
950616	885	225	2.8	0.30 (0.10)	0.50 (0.10)		
950620	889	195	3.5	0.37 (0.12)	0.29 (0.11)	0.25 (06)	0.54 (08)
950622	891	310	3.3			0.32 (04)	0.63 (06)
950624	893	300	2.8	0.20 (0.14)	0.31 (0.13)	0.19 (05)	0.58 (04)
950625	894	150	3.2	0.33 (0.16)	0.52 (0.14)		
950628	897	150	2.3	0.32 (0.13)	0.37 (0.10)		
950702	901	195	3.3	0.29 (0.15)	0.47 (0.14)	0.20 (09)	0.61 (13)
950704	903	420	2.9	0.32 (0.10)	0.74 (0.12)	0.08 (06)	0.93 (13)
950710	909	390	2.8	0.19 (0.13)	0.53 (0.14)		
950712	911	175	3.0	-0.08 (0.12)	0.62 (0.16)		
950722	921	525	2.6	0.25 (0.12)	0.68 (0.13)		
950724	923	150	3.0			0.32 (07)	0.61 (09)
950805	935	390	4.0	0.30 (0.21)	0.72 (0.17)		
950819	949	60	3.3	0.28 (0.17)	0.45 (0.14)		
950821	951	255	3.5	0.19 (0.17)	0.51 (0.16)		
950823	953	180	3.6	0.24 (0.15)	0.75 (0.12)		
950825	955	330	3.6	0.36 (0.16)	0.55 (0.15)	0.18 (06)	0.77 (09)
950827	957	375	3.7	0.34 (0.19)	0.44 (0.16)		
950911	972	270	2.6	0.24 (0.12)	0.54 (0.13)	0.24 (07)	0.63 (09)
950923	984	270	3.2	0.07 (0.12)	0.73 (0.16)	0.03 (06)	0.89 (13)
950925	986	150	3.0	0.02 (0.10)	0.77 (0.16)		
950929	990	510	3.0	0.16 (0.12)	0.53 (0.14)		
951001	992	570	2.9	0.25 (0.13)	0.71 (0.14)	0.27 (07)	0.79 (10)
951003	994	540	3.2	0.17 (0.12)	0.51 (0.13)	0.18 (05)	0.63 (08)
951007	998	200	3.6			0.49 (12)	0.53 (24)
951015	1006	300	2.9	0.08 (0.10)	0.67 (0.13)		
951017	1008	120	2.6	0.13 (0.09)	0.88 (0.14)		

Table 4.1: (continued from page 46)

date	Julian date	total exposure time per night (seconds)	seeing (pixel)	<i>Scheme A</i>		<i>Scheme B</i>	
				image A (mag)	image B (mag)	image A (mag)	image B (mag)
960717	1282	180	2.4	0.19 (0.10)	0.94 (0.12)		
960719	1284	210	2.3	0.19 (0.12)	0.66 (0.12)		
960721	1286	270	2.2	0.23 (0.08)	0.93 (0.11)		
960723	1288	210	2.3	0.00 (0.10)	0.79 (0.12)		
960728	1293	150	2.1	0.08 (0.10)	0.76 (0.10)		
960804	1300	240	2.6	0.33 (0.10)	0.71 (0.12)	0.20 (09)	0.82 (14)
960806	1302	330	2.7	-0.03 (0.09)	0.71 (0.13)		
960810	1306	270	2.3	0.19 (0.09)	0.80 (0.11)		
960812	1308	270	2.3	-0.01 (0.09)	0.86 (0.13)		
960814	1310	360	3.0	-0.21 (0.13)	0.64 (0.16)	-0.17 (05)	0.80 (12)
960818	1314	270	2.3	-0.01 (0.11)	0.72 (0.13)		
960903	1330	180	2.3	0.13 (0.09)	0.66 (0.10)		
960907	1334	90	2.5	-0.04 (0.09)	0.75 (0.13)	-0.03 (07)	0.96 (15)
960909	1336	90	3.0	-0.45 (0.11)	1.04 (0.20)		
960915	1342	180	4.1	-0.23 (0.19)	0.94 (0.22)	-0.32 (08)	1.25 (19)
960917	1344	180	3.1	-0.30 (0.14)	0.72 (0.18)	-0.22 (06)	0.92 (14)
960921	1348	90	2.4	-0.14 (0.10)	0.63 (0.13)		
960927	1354	270	3.1	-0.22 (0.12)	0.82 (0.16)	-0.21 (06)	0.98 (16)
960929	1356	120	3.3	-0.18 (0.15)	0.85 (0.20)		
961003	1360	90	4.6	-0.20(0.20)	1.12(0.22)	-0.33(06)	1.29(25)
961007	1364	180	3.8	-0.24 (0.23)	0.89 (0.21)		
961011	1368	120	2.2	-0.01 (0.09)	0.72 (0.12)		
961013	1370	285	2.2	0.14 (0.07)	0.84 (0.10)		
961018	1375	60	3.2	-0.14 (0.14)	0.47 (0.15)		
961024	1381	780	3.1			-0.26 (04)	0.88 (11)
961030	1387	120	3.3	-0.33 (0.12)	0.81 (0.20)		
961101	1389	240	2.5	-0.14 (0.08)	0.72 (0.14)		
961103	1391	120	3.9	-0.08 (0.13)	1.04 (0.21)		
961107	1395	150	2.1	-0.02 (0.07)	0.87 (0.11)		
961109	1397	90	2.2	0.14 (0.08)	0.97 (0.13)		
961111	1399	90	2.2	-0.06 (0.07)	1.02 (0.14)		
961116	1404	360	2.5			-0.14 (08)	1.01 (18)
961120	1408	510	2.3	0.00 (0.07)	1.03 (0.13)	0.00 (-)	1.07 (10)
961124	1412	210	2.8	0.17 (0.10)	0.69 (0.10)	0.12 (10)	0.75 (15)
961126	1414	630	2.9	-0.07 (0.10)	0.93 (0.15)	0.03 (06)	0.93 (11)

Table 4.1: (continued from page 47)

date	Julian date	total exposure time per night (seconds)	seeing (pixel)	<i>Scheme A</i>		<i>Scheme B</i>	
				image A (mag)	image B (mag)	image A (mag)	image B (mag)
970715	1645	140	2.3	0.05 (0.12)	0.80 (0.15)		
971003	1725	140	3.0			0.19 (06)	1.09 (14)
971018	1740	180	3.0	0.21 (0.14)	0.86 (0.16)		
971026	1748	390	2.2	0.27 (0.06)	1.23 (0.10)		
971030	1752	240	2.4	0.34 (0.13)	0.74 (0.13)	0.27 (–)	0.80 (08)
971101	1754	210	2.7	0.45 (0.14)	0.55 (0.12)	0.22 (04)	1.00 (06)
971103	1756	270	2.9	0.24 (0.15)	0.85 (0.16)	0.27 (05)	1.00 (09)
971105	1758	630	3.7	0.52 (0.16)	0.88 (0.14)	0.43 (03)	0.98 (03)
971107	1760	120	1.5	1.73 (0.47)	4.78 (1.22)		
971121	1774	220	2.8	0.15 (0.11)	0.96 (0.16)	0.12 (06)	1.12 (10)
971125	1778	630	3.1	0.27 (0.20)	0.74 (0.18)	0.17 (05)	0.74 (04)
971129	1782	450	2.2	0.34 (0.09)	0.88 (0.12)		
980101	1815	30	2.9	0.21 (0.10)	0.85 (0.14)		
980111	1825	60	3.3	0.04 (0.15)	0.64 (0.14)		

### 4.3 Data reduction pipeline

A total of 530 frames of Q2237+0305 were obtained at Apache Point Observatory in the  $r$ -filter in 73 nights from 1995 to 1998 (27 in 1995, 33 in 1996, 11 in 1997 and 2 in early 1998). The frames are processed with the following pipeline. We have pursued two reduction schemes (*A* and *B*), which will be described separately where necessary. The whole reduction is automated with scripts and can easily be repeated for parameter changes<sup>2</sup>. The scripts are either written in `awk` or contain chains of IRAF<sup>3</sup> commands. The reduction pipeline is controlled by several layers of scripts that (1) determine which frames are available, (2) feed this information to scripts that produce reduction scripts, and (3) run IRAF, as well as some self-written procedures to do the actual image reduction. The five steps of the data reduction pipeline are described in detail here.

1. Four reference stars in the vicinity of the galaxy were chosen as reference points (see

<sup>2</sup>The input/output of FITS files and FITS keywords into the analysis program was possible thanks to Rainer Köhler's Hellware "fitsio" library of C-routines.

<sup>3</sup>IRAF is the Image Reduction and Analysis Facility, a general purpose software system for the reduction and analysis of astronomical data. IRAF is written and supported by the IRAF programming group at the National Optical Astronomy Observatories (NOAO) in Tucson, Arizona. NOAO is operated by the Association of Universities for Research in Astronomy (AURA), Inc. under cooperative agreement with the National Science Foundation. Internet: `iraf.noao.edu`



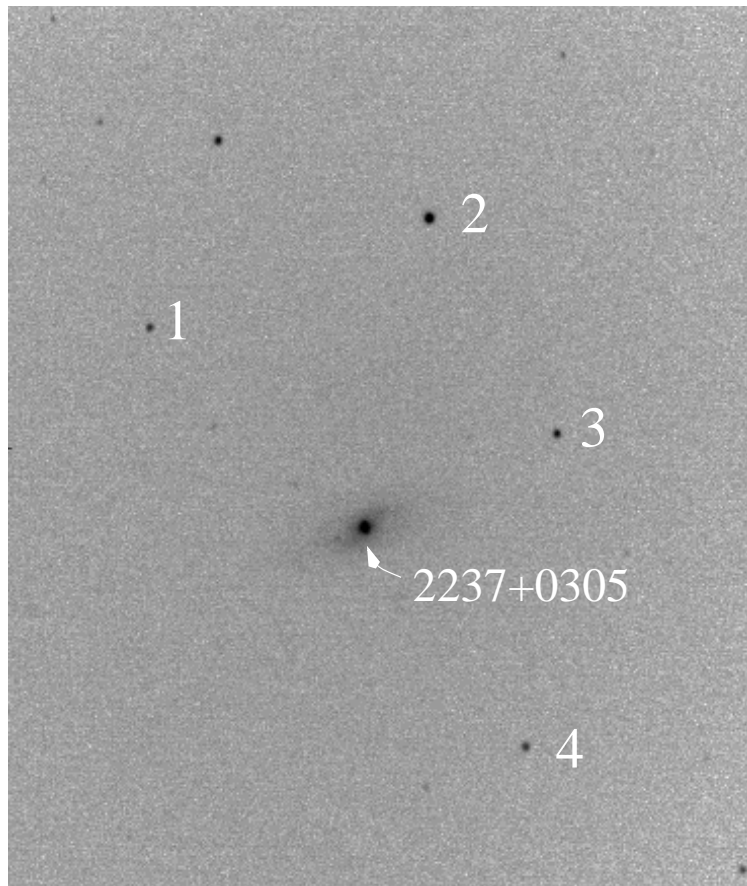


Figure 4.3: Image of the environs of the lensing galaxy 2237+0305 in the  $r$ -band. The image was taken at APO on 20 November 1996 under  $1.2''$  seeing. The four reference stars are marked 1 to 4. The four quasar images are situated in the core of the galaxy.

Fig. 4.3). Three of these are visible on every frame (stars 1, 3, 4), whereas the fourth (star 2), which is the brightest of the four, is visible on most frames.

*Scheme A:* The reference stars are automatically registered on each frame using a self-written C-routine that searches for the exact position pattern of the three (four) stars in each frame. The routine subtracts a four-star template with a default seeing of  $1.8''$  (3 pixels) from the frames, defines a quality of fit value  $\chi^2$  from the difference of the pixel fluxes  $i$  between the template and the observations,

$$\chi^2 = \frac{1}{N^2 - 1} \sum_{\text{all } N^2 \text{ pixels}} \frac{(i_{\text{template}} - i_{\text{observed}})^2}{i_{\text{observed}}}, \quad (4.2)$$

(assuming Poisson statistics  $\sigma_i \sim \sqrt{i}$  for the pixel counts) and searches for the best fitting solution with a minimum  $\chi^2$  by moving the star pattern through the whole frame.

*Scheme B:* All frames were run through the IRAF task “`findstar`”. This routine searches for four statistically significant peaks with user-defined significance above the noise level. For our purpose it was enough to just use the default settings since frames where the stars are not clearly detected are also not suitable for quasar photometry. The program generates a list of a number of such detections. We then wrote another script that calculates the distances between all `findstar` detections and selects our four targets by choosing pairs that have distances closest to the correct values, which were measured from one frame before. This procedure sometimes selects the wrong candidates if `findstar` does not detect all reference stars. In scheme B, we neglected frames where not all four stars were visible or detected.

2. Once the four reference stars are localized, the seeing is determined by fitting a circular Gaussian brightness profile to the brightness profiles of the reference stars with the IRAF task “`imexamine`”. This leads to results that are often different by up to ten percent. We use the seeing from the two brighter stars: in scheme A we use star 3, in scheme B we always use star 2. We also measure the distance of stars 2, 3 and 4 from the centre of the galaxy. These distances will be refined in step 5, but we need an approximate input to start the quasar and galaxy fitting procedure in step 4.

The reference stars are used to calibrate the frames of different nights relative to each other. We only selected frames where all four reference stars were observed. In Scheme A, we used star 3 as a reference star, whereas in Scheme B we used star 2. In Fig. 4.4 the magnitude difference between these two reference stars is depicted as a function of time. The differences plotted in this figure scatter around a median difference of 1.63 mag, which is indicated by the dashed line. The error bars are simply determined by Poisson statistics from the flux counts. Except for a few notable outliers, the data are consistent with our assumption that the two stars are not variable. If one or both of the reference stars were variable, our photometry would still be accurate to less than 0.02 mag in 65% of the cases, and 0.04 mag in 95% of the cases. The flux calibration relative to these stars is not only important because of varying transmission and seeing of the atmosphere at Apache Point Observatory, but also because the reflectivity of the mirror itself has changed substantially over the two-year time-span (Ed Turner 2000, priv. comm.). In Fig. 4.5, the fluxes of the two calibration stars are shown. The magnitudes are defined relative to a standard flux of 20 000 received counts during 60 seconds exposure time. We will use this relative measure also for the quasar photometry because we do not have absolute photometry of standard stars. It can be seen in this figure that especially the realluminization of the mirror at the end of 1996 (middle panel) has led to a significant increase of the mirror reflectivity in 1997 (right panel).

*Scheme A:* All frames from one night are coadded into a single image. The offsets between different frames are calculated from the reference stars. The frames are then aligned using the IRAF task “`imalign`”. In this process, all frames are bilinearly interpolated to the positions of one reference frame.

*Scheme B:* The rotation of each frame with respect to the orientation of the frames from

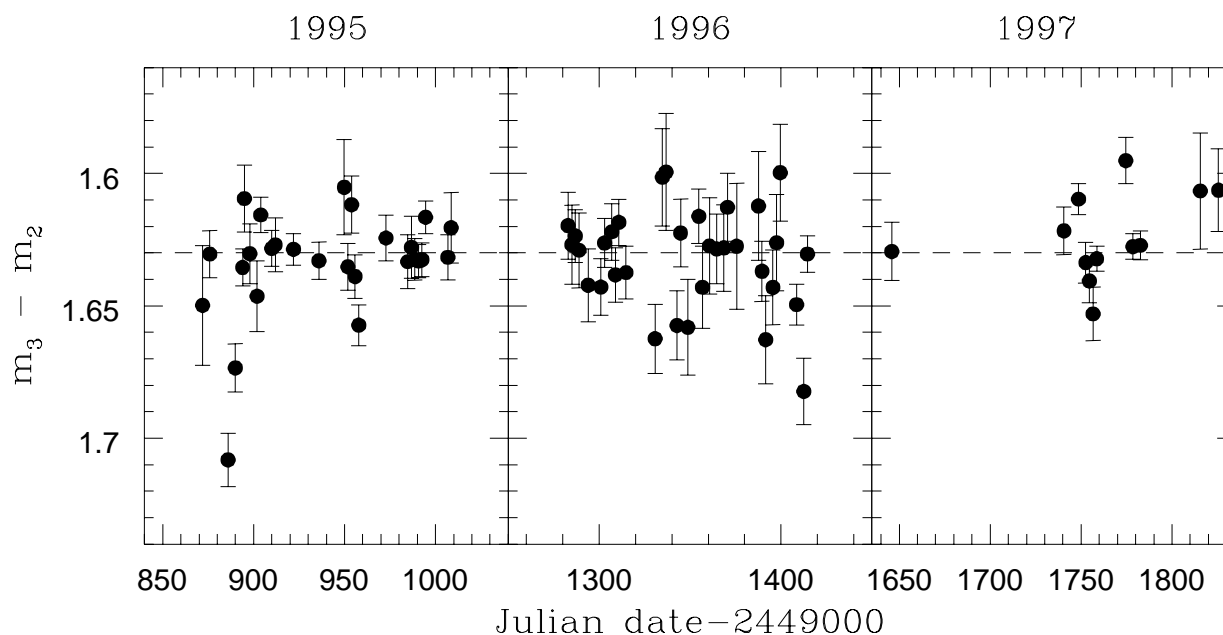


Figure 4.4: Magnitude difference  $m_3 - m_2$  between reference stars 3 and 2 in the 73 combined frames from Scheme A. The Poisson errors of the star fluxes were added in quadrature. The median magnitude difference 1.63 mag is shown with a dashed line.

September 23, 1995 is determined. This day was chosen because in the frames obtained on this day north is almost exactly up (with an accuracy of about 6 arcminutes). The frames observed on other days are sometimes rotated with respect to this day, probably due to technical problems with the alignment of the detector at the telescope. Besides a few large rotation values in about ten frames, we found that the frames have small rotations between a few tenths of a degree up to three degrees. If not treated properly, this rotation introduces an uncertainty in the photometry which we want to keep out in this scheme.

In scheme A we do not correct for the field rotations since we would also have to rotate the frames in addition to the bilinear interpolation `imalign` performs when it shifts the frames to one reference position. This procedure is very prone to errors because we sample a highly complicated structure (Fig. 4.1) with a rather coarse pixel sampling ( $0.6''$ ) and a seeing that is greater than an arcsec. This means we have to restrict ourselves to the frames with the small relative field rotations with up to three degrees.

In the current version of scheme B, we also have excluded the frames with large field rotations. We plan to extend the code so that current (from year 1998 and ongoing) Apache Point observations can also be analyzed by the program, and we will analyze all rotation angles then. In scheme B all frames are treated individually, and are not coadded.

3. The galaxy is modelled numerically using a model that was obtained by us [166] from the analysis of an HST V-band image of the galaxy [200]. The model consists of a De

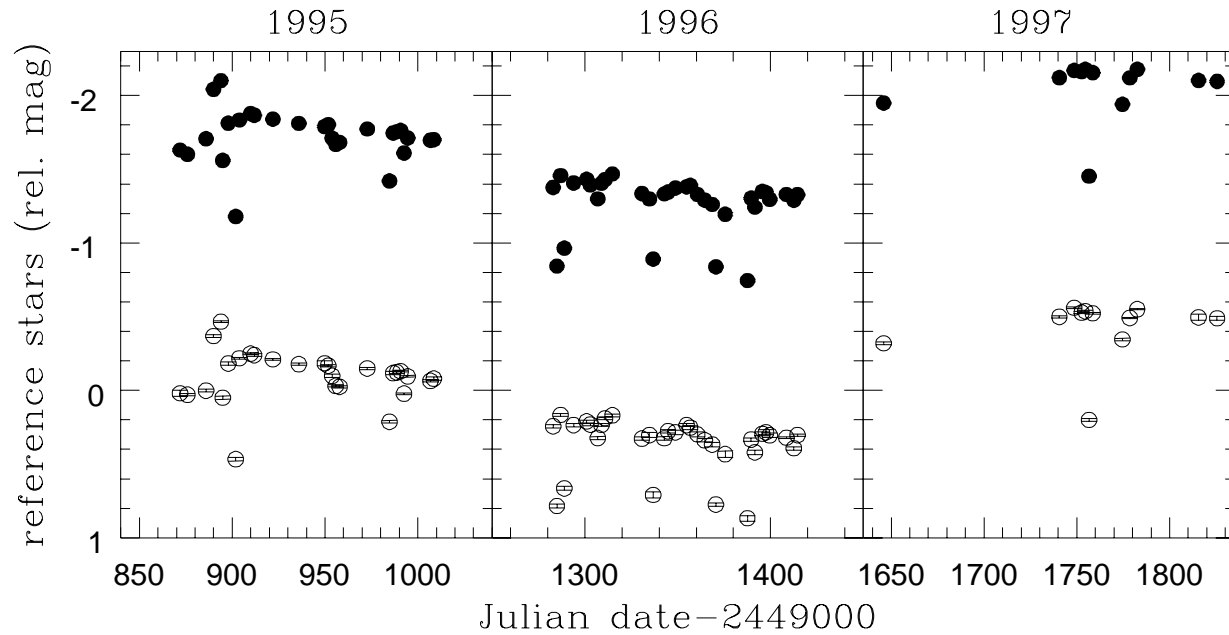


Figure 4.5: Transmission at Apache Point Observatory 1995-1997 as determined from the 73 combined frames from Scheme A. The raw apparent brightnesses of reference stars 2 (filled circles) and 3 (open circles) are depicted in the years 1995 (left panel), 1996 (middle panel), and 1997 (right panel). The fluxes are converted to magnitudes relative to a standard flux of 20 000 received counts during 60 seconds exposure time. It can be seen that at the end of 1996, the transmission become much better when the mirror was realluminized. The brightness variations are mostly seen in both stars, the difference is plotted in Fig. 4.4. The error bars are determined from Poisson statistics and are smaller than the circles, which can be seen in the case of star 3 (open circles) where they are not overplotted by the point filling.

Vaucouleurs [42] bulge and an exponential disk. The De Vaucouleurs brightness profile  $b(r)$  (in magnitudes per pixel) is given by

$$b(r) = 2.5 \log i_0 - 3.33 \left[ \left( \frac{r}{r_{\text{bulge}}} \right)^{1/4} - 1 \right], \quad (4.3)$$

where  $i_0$  is the central intensity (in counts per pixel) and  $r_{\text{bulge}} = 4.1 \pm 0.4$  arcsec is the half-light radius. Since the galaxy is inclined with respect to the line of sight, we use an elliptical surface brightness distribution for the bulge with a constant axis ratio of 0.69 and a position angle, indicating the galaxy inclination axis, of  $77^\circ$  (measured from north through east). The exponential disk brightness profile in magnitudes per pixel is given by

$$b(r) = 2.5 \log i_0 - \Delta b_0 - \frac{r}{r_{\text{disk}}} \quad (4.4)$$

with  $r_{\text{disk}} = 11.3 \pm 1.2$  arcsec and  $\Delta b_0 = 1.0 \pm 0.1$  mag arcsec<sup>-2</sup>. Due to the galaxy inclination, the surface brightness distribution of the disk is seen with an axis ratio of 0.5.  $\Delta b_0$  was determined in the HST I-band. Although the Apache Point data were taken in the  $r$ -band, we only left the amplitude  $b_0$  a free parameter and kept the  $\Delta b_0$  from the HST image for simplicity. The decomposition of the galaxy brightness profile into different components is not unique. It is, for example, also possible to use two exponential profiles, which could in general even be a more preferable solution [6]. However, any well-fitting description of the light distribution in the inner 3 arcseconds of the lensing galaxy will be good enough for us because the differences are washed out by the coarse sampling of the data, the seeing at Apache Point of more than an arcsecond, and noise.

In Fig.4.6 the central pixels of Fig. 4.2 are shown after the galaxy model has been subtracted. The remaining quasar images A and B (marked in the figure) are seen shining through the galaxy. Images C and D cannot be detected with any significance. Faintly, remaining structure is seen around the quasar images that is due to the bar-like spiral arm structure that extends into the galaxy centre [220, 166, 167] and was not included in the galaxy surface brightness model.

4. The positions of the four quasar images relative to the galaxy centre are known to an accuracy of 5 mas from HST observations in the UV [22]. Given our seeing, we consider the HST coordinates as “exact”. In the first fitting run, the galaxy position and amplitude, as well as the four quasar images are now fitted with the nonlinear minimization routine AMOEBA [140, page 408]. The quasar images are represented by four circular Gaussian brightness profiles with a full width at half maximum as determined from the seeing of the reference stars. The analytical galaxy model is also convolved with this Gaussian seeing model. AMOEBA evaluates a quality of fit estimator at 8 “corners” in the parameter space of galaxy position, galaxy amplitude, and quasar fluxes (as determined by the amplitudes of the Gaussians), at the vertices of an  $N$ -simplex. Only the counts  $i_{\text{model}}$  in the central

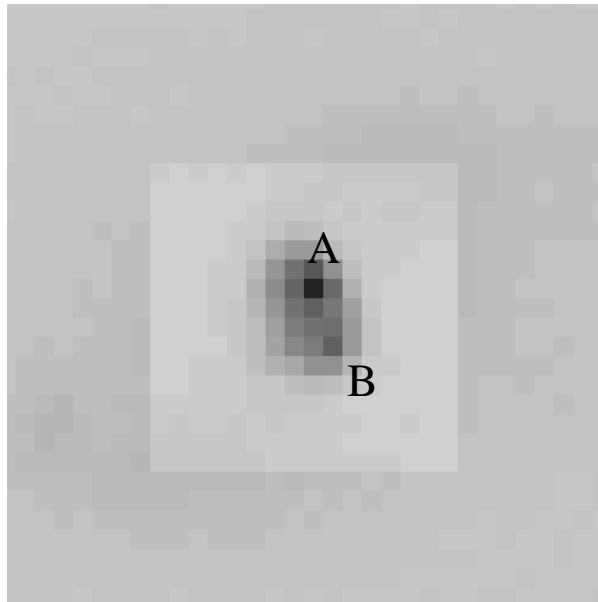


Figure 4.6: Image of the central  $18.6 \times 18.6$  arcsec of the lensing galaxy 2237+0305 in the  $r$ -band. The light from the galaxy has been subtracted in the inner square with 16 pixel, or 9.6 arcsec, side length. The image was taken at APO on 20 November 1996 under  $1.2''$  seeing and was shown unchanged in Fig. 4.2. The two point sources in the middle are the quasar images A and B (as marked). Images C and D are not detected with any significance because their amplitudes are not larger than the noise. This frame is rotated with respect to the HST image shown in Fig. 4.1.

$9 \times 9$  pixel are then subtracted from the observed pixel counts  $i_{\text{observed}}$ , and a  $\chi^2$  value as in eq. (4.2) is computed at the corners:

$$\chi^2 = \frac{1}{80} \sum_{9 \times 9 \text{ inner pixels}} \frac{(i_{\text{model}} - i_{\text{observed}})^2}{i_{\text{observed}}}. \quad (4.5)$$

AMOEBa then continues to compute the  $\chi^2$  values at the vertices of the simplex, and determines from this where to move the simplex through expansion and subsequent contraction in the parameter space. This way, the simplex “wobbles” into the dips and valleys of the  $\chi^2$ -surface. AMOEBA also tests the depth of detected valleys and tries to find deeper ones.

In order to constrain the parameter search to relevant parts of the parameter space, we introduced additional constraints such that trespassings across certain limit values were added quadratically to eq. (4.5). Such “parabolic walls” cause AMOEBA to proceed into a different direction on its parameter space search. This way, we enforced the physical constraints that all fluxes are positive, and that the fluxes of image C and D are smaller than the fluxes of A and B. One of these assumptions seems to be wrong in 1998 and 1999 where image C has “overtaken” image B during a brightness peak beautifully resolved by OGLE. However, our data record stops in 1997, and until then we did not notice even a significant rise of either image C or D towards the fluxes of A or B. As will be reported in Sect. 4.4, our flux estimates have also been quantitatively confirmed at a few points by independent observations.

5. In step 4 we have already produced a light curve with flux estimates for all quasar images. In this step we use the results determined in step 4 for all 73 nights (scheme A)/192 frames (scheme B) and determine the median galaxy amplitude and the median distances of the reference stars 2, 3, and 4 from the centre of the galaxy.

The fitting procedure is then repeated with a fixed value for the galaxy amplitude. The galaxy position is also fixed by the distances to the three reference stars 2, 3, and 4. Thus, only the four quasar fluxes are still free parameters. The distances of stars 2, 3, and 4 from the galaxy centre are

$$r_2 = 95.09 \pm 0.19 \text{ arcsec},$$

$$r_3 = 64.55 \pm 0.12 \text{ arcsec},$$

$$r_4 = 81.59 \pm 0.12 \text{ arcsec}$$

( $1\sigma$  error bars). The result of this process is a best-fit model with parameters and uncertainties that can be estimated from the depth and steepness of the  $\chi^2$ -surface dip [140, page 689].

*Scheme A:* We estimate additional uncertainties of the fluxes by varying the galaxy position within the range allowed by the separations of galaxy centre and reference stars. This is done by using 10 random positions for the galaxy allowed by the  $1\sigma$ -error bars of  $r_2$ ,  $r_3$

and  $r_4$  and by carrying through the whole analysis procedure. The error bars for Scheme A given in Table 4.1 and Fig. 4.7 (upper panel) are determined with this method.

*Scheme B:* The median of all magnitude estimates for each quasar image is taken and used for the final light curve. The observational error is determined from the sum of the squared individual errors. In scheme B a number of frames had dropped out of the analysis at various stages due to large seeing. Frames were also disregarded if the four reference stars were not all detected at the right places, or if the transmission was too low so that the fitting procedure for the quasar fluxes did not converge. After all this, a sample of 34 magnitude estimates remains in Scheme B.

## 4.4 Results, interpretation and prospects

We obtain light curves for images A and B as shown in Fig. 4.7, and detailed in Table 4.1. The fluxes of images C and D are not measurable with our data since the images are lost in the noise. Both reduction schemes A and B yield a similar light curve. In this figure we give the magnitudes with respect to the magnitude measurement of image A on 20 November 1996 because the absolute photometry between the two schemes is different by about 0.3 magnitudes. This uncertainty is caused by the insecure contribution of the galaxy flux to the quasar fluxes. It can be taken from this figure and Table 4.1 that the error bars are probably underestimated by the  $\chi^2$  technique [140, page 689] we employed, which assumed Gaussian statistics for the parameter measurements.

Despite the large error bars of the order of  $\approx 0.15$  mag for the individual data points in Fig. 4.7, there is evidence for a significant brightness peak in image A in 1996 with an amplitude of about 0.4 to 0.5 mag (relative to 1995) in the light curves, seen in both schemes. We already noted in Sect. 3.3.1 that theoretical models predict time-delays of intrinsic fluctuations of the quasar between images A and B of a few hours [169]. Since image B does not vary much, or perhaps shows a slight decrease, the uncorrelated flux variation in image A can be interpreted as microlensing in the lensing galaxy.

Since we had to carry out an involved data reduction process to do photometry on these data, it would be good to have independent evidence for the magnitude rise of image A in 1996, and perhaps some estimate of the brightnesses of the images in 1995 or 1997. Observations by Burud et al. [24] at the Nordic Optical Telescope (NOT) on La Palma on 10/11 October 1995 (Julian Date - 2449000 = 1001 / 1002) measured in the  $R$ -band a magnitude difference of images A and B of  $\approx 0.19$  mag. In 1996, both the NOT (web pages of the Oslo 1998 workshop on gravitational lensing) and Maidanak Observatory in the Ukraine observed that image A had become much brighter than the other images. At Maidanak Observatory, no quantitative measurement was made because of technical problems (Shalyapin 1999, priv. comm.). In 1997 on day 1800 (Julian Date - 2449000), the OGLE group finds  $m_A = 17.35$  mag and  $m_B = 17.83$  mag, which amounts to a magnitude difference of  $\Delta m = 0.48$  mag (with an error of 0.03 mag). Within the error bars we thus have quantitative evidence for our measurements in 1995 and 1997. In 1996 we have qualitative evidence for a brightness rise of image A.



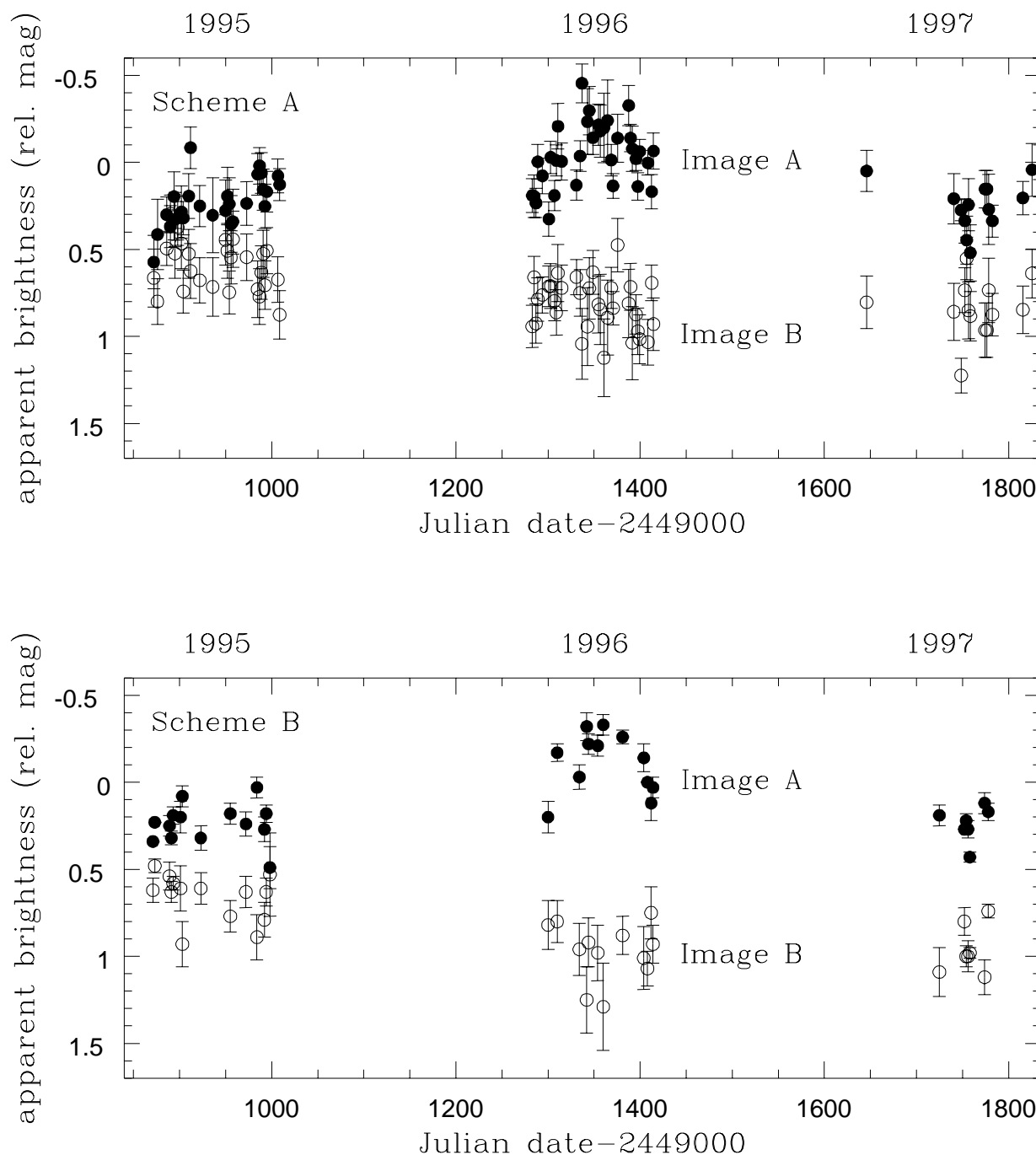


Figure 4.7: Light curve for images A (filled circles) and B (open circles) of Q2237+0305 from June 1995 to January 1998 as determined using two different reductions Schemes A (top panel) and B (bottom panel) that are described in Sect. 4.3. In the text, the epochs are referred to as 1995 (left), 1996 (middle), and 1997 (right). The magnitudes are given with respect to the measured magnitude of image A on 20 November 1996.

In agreement with the results from the OGLE group [209] (Sect. 3.3.1), we find that Q2237+0305 shows large magnitude variations of several tenths of a magnitude on timescales of less than hundred days. It is becoming evident that the microlensing variations in Q2237+0305 can happen rather smoothly over time spans of several months to years. The Irwin et al. [81] event or even Racine's [141] interpretation of it seem to have been examples of short-duration variations. The Pen et al. [136] drop perhaps was an example of a high-magnitude short-term process, but with very low signal-to-noise at that time. All in all, it is fair to say that the observations of Q2237+0305 have started over the last two years to resolve microlensing variations in great detail, and they look very much like the variations that were predicted already in early 80s for the microlensing effect.

It is possible to produce such variations in scenarios as described in the papers by Wambsganss et al. [194], Webster et al. [198] or Witt & Mao [207] with some "normal" stellar population (see footnote 4 on page 30) and an optical continuum region of the quasar that is smaller than about a light day. However, in order to exclude certain regions of the space of possible masses, one now needs to analyze the exact variation properties. Similar to our study in chapter 3, Wyithe et al. [216] studied the microlensing variations seen in the recent OGLE data [209] of Q2237+0305 and find that the data only exclude source sizes greater than 0.1 Einstein radii, which is a factor of 10 less stringent than the light-day limit mentioned above. In order to make progress, more involved statistical measures can be studied.

The total magnitude variation basically is the zeroth-order correlation function for Q2237+0305. It is now possible to look at 1-point, 2-point, 3-point, and possible even higher-order correlation functions of the difference light curves. Moreover, peak-finding algorithms such as described in Witt & Mao [207] or Wyithe et al. [216] that automatically detect peaks and quiescence periods in simulated light curves will be helpful to classify the variation properties of the observed and the simulated microlensing light curves.

The other ingredient that is needed, of course, is the continuous monitoring. The OGLE light curve started where the data discussed in this chapter stopped and thus shows the continuation of the light curve. At Apache Point data are also still being taken. Several other observatories (Maidanak Observatory, NOT) also monitor Q2237+0305.

The four quasar images in Q2237+0305 shine through the centre of a spiral galaxy, within less than a kpc of the core. In this region it is clear that there are stars close to the light path. The mass-to-light ratio within the circle of the four quasar images can be determined from mass models of the system to be  $M/L_I \approx 4 h_{60}$  in the  $I$ -band [166], as well as  $M/L_R = 5.3 h_{60}$  and  $M/L_B = 7.4 h_{60}$  in the  $R$ - and  $B$ -bands [153]. Such mass-to-light ratios can be explained by normal stellar populations without any additional dark matter (Simon White 1999, priv. comm.), but the issue is not entirely solved since it can also be interpreted that the mass-to-light ratios do still allow for baryonic dark matter in the galaxy centre (Trentham 2000, priv. comm.). Although in Q0957+561 we did not find any  $10^{-2} M_{\odot}$  MACHOs (for the small quasar sizes) in chapter 3, in Q2237+0305 they have not been excluded yet.

During a microlensing variation with an amplitude of 0.4 mag, part of the quasar is magnified by a factor of 1.45. The microlensing effect offers the opportunity not only to learn about the microlensing masses, but also about the size of the optical continuum emitting region and structure therein. Lewis et al. [110], for example, could show that a broad emission line of the quasar

was changed by microlensing. In fact, a number of studies [1, 221, 223, 116] have shown that microlensing events may be very sensitive to the details of quasar structure. There is a project underway by Rachel Webster, Ed Turner and collaborators that aims at studying Q2237+0305 during a caustic crossing event in parallel with HST and NASA's new Chandra X-ray observatory launched last year. By combining ground-based photometry, HST UV or optical spectra and photometric data, and Chandra X-ray data, it could be possible to limit the quasar structure in great detail.

The current theory of quasars interprets the source of the quasar radiation as a very hot accretion disk that consists of matter in rotation around a supermassive black hole of some  $10^8 M_{\odot}$  or more at the centre of a galaxy [145, 21]. X-ray radiation is thought to emerge from a smaller region in the accretion disk than the optical continuum. The different regions will be magnified differently, corresponding to their size. The specific microlensing properties of elliptical annular regions have been studied by Fluke & Webster[53], so that possible microlensing effects from such regions are already known in detail. We should add here that although Q2237+0305 is very X-ray weak, Wambsganss et al. [196] detected it at  $2.2 \times 10^{45}$  erg s<sup>-1</sup> in the ROSAT energy band 0.1-2.4 keV. It will thus be possible to study the quasar with Chandra.

Brightness peaks such the 1996 maximum of image A reported in this chapter or the beautiful peak of image C in 1999 observed by OGLE [209], or perhaps even the Irwin et al. [81] event or the Pen et al. drop [136], might have been caustic crossing events. For the much smaller X-ray source, the light curve would have been much more peaked if indeed a caustic crossing was observed. Photometry and spectroscopy of such events could reveal information about the quasar itself that is otherwise inaccessible and would put limits on the structures in quasar accretion disks and their relative sizes. This sounds especially promising in view of the fact that it is currently not known what a quasar brightness profile really looks like.

Monitoring programs such as conducted by the OGLE group, the Apache Point Observatory and also other observatories (for example, Maidanak, NOT), have to play key roles for such studies because they will help to decide when the space telescopes should start observing. The monitoring data have to be reduced "online", so that developments in the source are recognized quickly. OGLE is already doing this, and we are about to apply the method described in this chapter to the more recent and new Apache Point monitoring data as well. Since the detector at APO has been improved, it should be possible to obtain much more accurate magnitude measurements for the quasar images with the newer data (see, for example, the images at [www.astro.princeton.edu/~elt/2237.html](http://www.astro.princeton.edu/~elt/2237.html)).

# Chapter 5

## Limits on universal rotation from weak gravitational lensing

In this chapter, we use a formalism that allows us to calculate the gravitational lensing effect of a rotating universe on the distortion of faint background galaxies to show that current weak lensing observations can put limits on a possible cosmic rotation.<sup>1</sup>

### 5.1 Birefringence of the polarization of radio sources

In April 1997 a number of papers appeared on the Los Alamos preprint server on the rotation of the plane of polarization of the light from extragalactic sources in excess of Faraday rotation. This effect is called “birefringence”. The debate was started up by a paper by Nodland & Ralston [122] who claimed to have detected birefringence in the radiation from radio galaxies at cosmological distances. In many respects the debate was reminiscent of an earlier debate that was initiated in 1982 by a paper by Birch [18], so we will start with this paper. Birch claimed to have detected a proportionality

$$\Delta \sim \cos \theta \tag{5.1}$$

between the difference  $\Delta$  of the major elongation axis and the direction of the average polarization of a sample of radio sources and the cosine of the angular separation  $\theta$  from the position of a celestial pole that he determined. Similar claims were made by other researchers later, a complete list is given in [100]. In their 1997 paper, Nodland & Ralston [122] used redshift information on their sample and found relation of the form

$$\Delta = \frac{1}{2 \Lambda} r \cos \varphi, \tag{5.2}$$

---

<sup>1</sup>Due to the mathematics of general relativity, it is necessary in this chapter to use tensors, related index conventions, tensor analysis and parallel transport as described, for example, by Weinberg [199, chapter 4]. For the full definitions of fundamental tensors of general relativity, such as the metric tensor, the Ricci tensor and the Weyl tensor, the reader is also referred to this book [199]. For the study of this chapter, however, the line element or the metric tensor are mainly needed. Other quantities are then explained in the context.

where  $r$  is the comoving distance, and  $\Lambda = 13.2 \pm 1.0 \frac{c}{H_0}$  is the so-called birefringence scale. Unfortunately, the poles of these two studies do not agree. In fact, an analysis by Obukhov [123] finds  $\Lambda = 3.6 \pm 1.6 \frac{c}{H_0}$  when fitting the relation (5.2) to Birch's data<sup>2</sup>. The results by Birch and by Nodland & Ralston were quickly questioned, however, by other researchers who found them not to be statistically significant (for example [28], [48],[139]). We do not enter this discussion, but rather try to tackle this problem with a different method.

While Nodland & Ralston tried to explain their finding with a modification of electrodynamics, several authors (for example [103], [112], [124]) immediately proposed to explain the effect with the rotation of the universe. This notion refers to homogeneous, but anisotropic cosmologies, where observers at any point see the universe rotating around them. This class of cosmologies will be discussed in the next section. The earlier results by Birch [18, 19] had also been interpreted by him as an indication of cosmic rotation, but he favored a scenario where the whole universe is rotating with a single axis. In this scenario, Birch obtains a limit on the rotation by considering the angular momentum transfer from the universe to the galaxies.

## 5.2 Cosmic rotation

In 1946 George Gamov [55] wrote a small note about the possibility of a rotating cosmos. He wondered why galaxies are rotating and put forward the idea that this could be due to a general rotation of the whole universe around some centre "located far beyond the reach of our telescopes". He even proposed to detect this effect by the equivalent of Oort's effect in the radial velocities of galaxies. In our galaxy, the Oort effect is used to prove that the sun is rotating around the galactic centre by exploiting the effects of the differential rotation on the velocity of nearby stars. Gamov's idea is similar to a scenario that had been studied by Lanczos in 1924 [107], who solved Einstein's field equations for an infinite, rotating dust cylinder.

It seems like a quantum leap from these ideas to the Gödel [58] solution from 1949 that represents a homogeneous, but rotating universe (with a cosmological constant  $\Lambda$ ). In this solution, matter rotates everywhere with a constant angular velocity relative to an observer in an inertial system (a very good illustration is given by Hawking & Ellis [69, page 168]). Test particles and light rays are deflected from a straight path and start to oscillate along rosetta tracks [106].

In Newtonian language, this rotation is described by the rotation matrix of a velocity field  $\vec{v}$  [101]

$$\omega_{\eta\tau} = v_{[\eta,\tau]}, \quad (5.3)$$

where the comma denotes partial differentiation with respect to  $x^\tau$ , and the brackets indicate that only the antisymmetric part is used. The non-zero components of this matrix are the components of the angular velocity

$$\vec{\omega} = \frac{1}{2} \nabla \times \vec{v}. \quad (5.4)$$

---

<sup>2</sup>Birch did not find any correlation with redshift in his data.

Each element of this vector appears twice in the rotation matrix, once positive and once negative (for example [23]). We obtain the magnitude of the angular velocity by computing the expression

$$\omega = \frac{1}{2} \sqrt{\frac{1}{2} v_{[\eta,\tau]} v_{[\eta,\tau]}}, \quad (5.5)$$

where the sum convention was employed. The expression (5.3) can be generalized for general relativity by using the 4-velocity of an observer and covariant derivatives, see Misner et al. [117, page 566] for a definition. We will only need the magnitude of the rotation here, which is given by the contraction

$$\omega = \sqrt{\frac{1}{2} \omega_{\mu\nu} \omega^{\mu\nu}} \quad (5.6)$$

( $\mu$  and  $\nu$  now denote coordinates in space-time). In a homogeneous universe, every observer sees the universe rotating around him. We will call the observer's axis of rotation the "cosmic rotation axis", although this axis only has a meaning for this particular observer. Compared to eq. (5.5), we leave out the factor of  $\frac{1}{2}$  since it was left out by the authors of the cosmological models tested in this chapter. Whenever we talk about the angular velocity, however, this factor needs to be kept in mind.

### 5.3 Limits on cosmic rotation

The Gödel model was an important step in the study of general relativity because it showed that homogeneous, rotating cosmologies exist in general relativity<sup>3</sup>. As a model of the universe, however, it has its flaws. Gödel himself already showed that closed timelike curves exist at a certain distance from the observer (beyond the light cone), so that the model violates a causal structure of space-time and could be regarded as unphysical. It should be noted that in a philosophical paper from 1949, Gödel defends his model against the objection of "unphysicality" since although timelike curves exist in the model, it is not possible to use them as time machines ([51, page 199]). To be conservative, however, we limit our study to rotating cosmologies that have no closed timelike curves. The Gödel model also is a static model in the sense that it does not contain cosmic expansion. This is a further strong flaw of the Gödel model because, as outlined in Sect. 1.2, the hot early universe, the microwave background radiation and the cosmic expansion are such important foundations of modern cosmology that they should be part of every cosmological model.

Nevertheless, theorists took up the task to thoroughly analyze the Gödel model (for example [106]), and to find more general solutions that have no closed timelike curves and cosmic expansion (for example [59], [130]). Starting in the late 60s, a new strong constraint on cosmic rotation appeared when it was realised that the cosmic microwave background (CMB) radiation showed only very little anisotropy [11, 35, 68]. If one assumes that the CMB radiation was emitted at the

---

<sup>3</sup>The Gödel cosmos is a strong example against the belief that Mach's principle has to result from the theory of general relativity (for example [70], [130], [134, page 15], [143])

time of last scattering when the universe became optically thin, these photons arrive at the detectors from a well defined surface around us, so that the photon trajectories should be influenced by any large scale anisotropy of the universe. The three basic contributions to the anisotropy of the microwave background radiation were first described in 1969 by Hawking [68]:

- (1,2) red- or blueshift of the CMB photons by the velocities of the matter flow at emission and detection of the CMB photons (these contributions are zero in models with comoving matter flow)
- (3) anisotropic expansion of the universe (which is calculated as an integral over the whole light path)

In such universes, cosmic rotation introduces velocity structure into a homogeneous surface of photons coming from a narrow range of redshifts. The patterns range from hot spots over dipole and spiral patterns to even more complicated structures (plots can be found in [11]).

## 5.4 Weak lensing and cosmic shear

In 1966, Kristian & Sachs [101] introduced an independent test for the anisotropy of the universe. They found that in anisotropic models, distant objects appear distorted. They show that circular objects at an angular diameter distance  $r$  are deformed into ellipses with an axis ratio  $p$  of major and minor axis

$$p = 1 + C r^2 + O(r^3) \quad (5.7)$$

where  $C$  is a function of the position on the sky and the Weyl tensor  $C_{\alpha\beta\gamma\delta}$ .

In the 80s, it was realised that an inhomogeneous matter distribution of the universe would magnify and distort background objects [197]. The term “*weak lensing*” was later introduced in 1992 [89] to refer to this distortion of the shapes of distant galaxies by the intervening matter. The centre of interest at the beginning of the 90s was to use this effect to infer the mass that is the source of the gravitational potential, especially to detect and map the dark matter distribution in clusters of galaxies. So-called “*weak lensing inversion*” of distortion maps can be performed using the pioneering Kaiser & Squires [90] inversion technique, or one of its many descendants, that reconstructs the surface mass density from the shear that is measured from the distortion of background sources.

In order to do this, however, one needs a clean estimate of the distortion of the galaxies. For the purpose of illustration, consider background galaxies with perfectly elliptical isophotes with an axis ratio of minor and major axis  $0 < q < 1$  and a position angle  $\theta$  of the major axis (measured counterclockwise from north, for example). Since there are two of such position angles, the galaxy shape can be represented by a complex quantity  $\epsilon$  with [13]

$$\epsilon = \frac{1 - q^2}{1 + q^2} e^{2i\theta}. \quad (5.8)$$

For a population of such galaxies with identical  $q$ , but random  $\theta_i$ , where  $i$  is the number of a particular galaxy, the average of all  $\epsilon_i$  is zero. Also, if the galaxies have  $q_i$  according to some distribution function, the average of all  $\epsilon_i$  is zero.

The next step is to assume a varying gravitational potential between us and the distant galaxies. Due to this potential the galaxy shapes are distorted so that the average of the  $\epsilon_i$  is shifted away from the origin of the complex plane. The magnitude and direction of the shift are a measure of the cosmic shear. A detailed account on how an  $\epsilon$  can be defined for real galaxy shapes, and how the average  $\epsilon$  can then be turned into shear measure as defined in eq. (2.22) is explained in detail in the reviews by Mellier [115] and Bartelmann & Schneider [13].

For our purpose it is important to note that it is possible to obtain an estimate of the cosmic shear by averaging the “shapes” of several (depending on the accuracy needed, of order thousands) background galaxies in spite of the intrinsic galaxy shapes. We are only concerned with the shear estimates here because they can be used to place limits on rotating Gödel-type cosmologies. We thus do not delve any further into the technicalities of obtaining mass maps from weak lensing inversion.

## 5.5 Lensing limits on cosmic shear

In the 1966 Kristian & Sachs paper [101], and in two following papers by Kristian in 1967 [102] and Valdes et al. in 1983 [186], the lack of observed strong deformations of distant galaxies was used to put limits on the factor  $C$  in eq. (5.7). The latest limit [186] is  $0.2 H_0^2/c^2 = 8 \times 10^{-3} h_{60}^2 \text{Gpc}^{-2}$ , where  $c$  is the speed of light and  $h_{60} = H_0/60 \text{ km s}^{-1} \text{ Mpc}^{-1}$ .<sup>4</sup> These papers do, however, not give limits on cosmic vorticity derived from limits on  $C$ .

Rather, Valdes et al. show that eq. (5.7) can be motivated by considering the distortion acting on a light bundle that is deflected by a spherical region of radius  $b$ , distance  $D$  and overdensity  $\Delta\rho$ . At the impact parameter  $b$ , the whole bundle is deflected by an angle  $\alpha = 4 G M/b c^2$ . In addition, the light from a circular background object at the distance  $r > D$  will be distorted into an ellipse. Using the angular separation of the bundle from the overdensity region as seen by the observer  $\psi = b/D$ , the axis ratio  $p$  of major and minor axis in the weak distortion limit is given by

$$p = \frac{a}{b} = \frac{1 + \frac{\partial\alpha}{\partial\psi}}{1 - \frac{\alpha}{\psi}} \approx 1 + \frac{\partial\alpha}{\partial\psi} + \frac{\alpha}{\psi} = 1 + 16 \pi G \Delta\rho b D/c^2. \quad (5.9)$$

If the object is at the distance  $r = 2D$ , this becomes

$$p = 1 + C r^2 \quad (5.10)$$

for  $C = 4 \pi G \Delta\rho \psi/c^2$ . Using this relation and the null-distortion results from the statistical analysis of the shapes of 44462 galaxies, Valdes et al. obtain limits on mass inhomogeneities ( $\Delta\rho/\rho < 0.1 \Omega$ ) and cosmic microwave background anisotropies ( $\Delta T/T \lesssim 6 \times 10^{-4}$ ).

---

<sup>4</sup>The Valdes et al. paper appeared shortly after Birch’s [18] Nature article. Although Birch’s article is listed in the references, there does not seem to be a citation of it in the text.



A few estimates of the cosmic shear can be found in the literature. Schneider et al. [174] looked at the fields around four quasars and only in the case of PKS1508-05 detect a cosmic shear signal of  $\gamma \approx 0.03$  (with an accuracy  $\approx 0.1$ ) on a scale of about one arcminute from an analysis of a  $2 \times 2$  arcsec field around the quasar. Wilson, Kaiser & Luppino have looked at six  $29' \times 29'$  fields as part of the UH8k Weak lensing survey [203, 204] and detect no cosmic shear, with an upper limit of  $\gamma < 0.009$  in the *I*-band and  $\gamma < 0.017$  in the *V*-band at three  $\sigma$ . These results were presented at the 1999 Boston gravitational lensing meeting, the Wilson et al. [204] results are not published yet. Wilson [203] noted that in the analysis of her frames  $\gamma_1$  is usually larger than  $\gamma_2$ , which indicates systematic effects. It is uncertain whether this could change the results significantly. We currently only have the average values given above at hand since their final analysis does not seem finished yet.

For the purpose of this chapter, we will use  $\gamma_{\text{limit}} = 0.04$  as an upper limit on the cosmic shear. Although for the Schneider et al. [174] data, it is only the  $\approx 1\sigma$  upper limit, this is compatible with the other estimates and also far beyond what is compatible with the Wilson et al. data. There is one caveat, however. We cannot be sure from these values that they are representative of the whole sky. Kristian & Sachs [101] noted that the distortion effect depends on the position on the sky, and we will show in the next sections that this is the case for the models studied in this chapter as well. Nevertheless, since the cosmic shear was tested independently on several spots on the sky, northern and southern hemisphere, we will make the assumption here that there is no cosmic shear seen on the sky with  $\gamma > 0.04$ . We keep in mind, however, that the observations could have missed high-distortion spots.

A further ingredient that is needed is the redshift of the sources from these studies. If the universe had a uniform space density of galaxies, the number density of galaxies per square degree would monotonically increase with redshift. However, observations always have a magnitude limit, corresponding to the faintest sources that can be detected. This introduces a cut-off in the number of high-redshift galaxies that can be detected so that the observed number density of galaxies drops towards high redshift again. Observations are also carried out in specific filters, so that the dominant part of the spectrum of the galaxy can be moved in or out of the used filter range by the cosmological redshift. This introduces a further variation of the number density as a function of redshift. Finally, galaxy evolution and the fact that galaxies form at some high redshift further modify this picture.

The bottom line of this consideration is that background galaxies in observed images have a number density that peaks at a certain redshift (Mellier [115] shows measured distributions of background galaxies). Mean values that are often assumed in studies are  $z = 0.7$  or  $z = 1$ , but the values depend on the filter used and the magnitude limit. Results from high-redshift cluster inversions [33] show that in deep exposures even at a redshift of  $z = 0.8$  there are still enough background galaxies to detect a weak lensing signal. The cosmic shear estimates mentioned above were obtained with very deep images, so that we study mostly background sources at a redshift of 1. In a few cases we illustrate the dependence of the distortion effect on redshift (Fig. 5.2).

A shear value of  $\gamma \approx 0.04$  is at the limit of what the technique described in this chapter is able to probe: in the standard cosmological paradigm of structure formation most of the mass of the universe is thought to be dark matter that is distributed in multiply connected filaments.

In this picture, galaxy clusters are located at the connection points of the filaments. From both analytical and numerical studies it is expected that the average shear of background sources due to this matter distribution alone is at the two to five percent level [86, 87]. Schneider et al. [174] noted that their detection compares well with these theoretical estimates. In this respect, the Wilson et al. result is puzzlingly low.

## 5.6 Rotating universes without CMB anisotropy

The outcome of the studies by Hawking and others [68, 69, 11] discussed in Sect. 5.3 was that the isotropy of the CMB radiation indicates a very low rate of rotation of the universe<sup>5</sup>. The precise limits depend on the cosmology itself, the most complete list of limits is given by Barrow et al. [11]. Birch [18], for example, found that  $\omega = 10^{-13}$  rad year<sup>-1</sup> or  $1.5 H_0$  for  $H_0 = 60 \text{ km s}^{-1} \text{ Mpc}^{-1}$  (with  $\omega$  defined in eq. (5.6)) is allowed by the CMB observations. Starting in the 80s, however, shortly after Birch’s paper, a new class of rotating cosmologies was invented [82, 83, 84] that promises to evade this strong constraint.

The main results from these studies were compiled in a paper by Korotky & Obukhov in 1996 [100]. In essence the new class of metrics consists of generalized versions of Gödel’s metric [58] that share one important property with Gödel’s original metric: the shear tensor vanishes everywhere. The authors of this new class of metrics point out that the anisotropy studied by Hawking and others is caused by the shear of the matter flow. We can illustrate this quantity by again looking at the Newtonian analogue, the trace-free shear matrix  $\sigma_{\eta\tau}$  for a velocity field  $\mathbf{v}$  [101]

$$\sigma_{\eta\tau} = v_{(\eta,\tau)} - \frac{1}{3} \delta_{\eta\tau} \nabla \cdot \mathbf{v}, \quad (5.11)$$

which contains all derivatives of the velocity field<sup>6</sup>. The brackets indicate the symmetrization (which removes rotation). The shear matrix is zero, if all “mixed” derivatives vanish and  $v_{1,1} = v_{2,2} = v_{3,3}$ . The new metrics also have a comoving matter flow, so that all three contributions identified by Hawking are zero, and the new metrics cannot be excluded by the CMB data.

We concentrate here on the so-called “Gödel-type” metrics that are a special case of the rather general class of metrics that is discussed in Korotky & Obukhov’s paper, and in several papers referenced therein. The Gödel-type metric is given in the following form:

$$ds^2 = c^2 dt^2 - 2c\sqrt{\sigma}R(t)e^{mx} dt dy - R^2(t) (dx^2 + k e^{2mx} dy^2 + dz^2), \quad (5.12)$$

where  $t, x, y, z$  are cosmic time and local Cartesian coordinates.  $c$  is the speed of light. The metric has several free parameters  $k > 0$ ,  $\sigma > 0$  and  $m > 0$  ( $k$  and  $\sigma$  are dimensionless,  $m$  has the dimension of length). The cosmic scale factor  $R(t)$  is determined by the field equations. The original Gödel metric would be recovered for  $k = -\frac{1}{2}$ ,  $\sigma = 1$ ,  $m = 1/c t_0$  (where  $t_0$  is the age of the universe defined in eq. (5.29)) and  $R(t) = \text{const}$ . We follow Korotky & Obukhov and consider only models with  $k > 0$  in order to ensure that the space time is causal [100, 111].

<sup>5</sup>See also Hawking’s introductory note to Gödel’s work on rotating cosmologies [70].

<sup>6</sup>The general relativistic expression for the shear tensor can be found in [117, page 566].

As we noted before, the angular velocity of the universe around observers at rest is described by the scalar  $\omega$  as defined in eq. (5.6). For the metric (5.12), one obtains [133, 99]

$$\omega = \frac{m c}{2} \sqrt{\frac{\sigma}{k + \sigma}}, \quad (5.13)$$

where  $c$  is again the speed of light. In principle, universal rotations is thus possible at substantial rates: for  $m \approx H_0/c$  in the limit  $k \ll \sigma$ , the rotation is of the order of microarcseconds per year and over a Hubble time, the universe may rotate by half a radian.

Korotky & Obukhov [100] present several observational consequences of such cosmological models and conclude that they are still consistent with the observations. Since the Weyl tensor is not zero for this class of metrics, it is to be expected from the Kristian-Sachs formula (5.7) that image distortions of faint background galaxies should occur. It is the aim of this chapter to continue the work of Kristian & Sachs [101, 102], as well as Valdes et al. [186], and apply it to this class of metrics.

In the references [123, 99, 100, 124] it is noted that it is possible that the observations of cosmological birefringence by Birch [18, 19] and later by Nodland & Ralston [122] are explained by the Gödel-type metrics. They find that universal rotation can indeed explain the rotation of the galaxy shape with respect to the polarization vector found in the relation (5.2). Under this assumption, the authors arrive at very large estimates for the magnitude of the universal rotation. We already mentioned in Sect. 5.1 that from the Birch data Obukhov [123] obtained a birefringence scale of  $\Lambda = 3.6 \pm 1.6 \frac{c}{H_0}$ , from which he deduced an angular velocity of  $\omega = 1.8 H_0$ . The Nodland & Ralston scale of  $\Lambda = 13.2 \pm 1.0 \frac{c}{H_0}$  would even correspond to  $\omega = 6.8 H_0$  [124].

However, Panov & Sbytov [133] also calculated this problem for the Gödel-type metric and arrive at a different relation for the birefringence effect for the Gödel-type metric: they obtain a  $\sin^2 \theta$  dependance instead of the  $\cos \theta$  in eqs. (5.1) and (5.2). We obtain results identical with Panov & Sbytov using the method by Seitz, Schneider & Ehlers [176]. Independently, Perlick (1999, priv. comm.) also arrives at this conclusion. In this light, it seems that the published rotation values cannot be compared with our approach. We will thus not test specific models, but rather scan the parameter space of  $k$ ,  $\sigma$  and  $m$  and determine shear values for background sources to probe this parameter space with the distortion effect.

In order to calculate the distortion effect, however, we do not want to rely on the Kristian-Sachs approximation “that the universe is described by a Riemannian space time with slowly varying metric tensor” [101]. Rather, we will calculate the distortion of light rays for the Gödel-type metric by direct integration along the light path. This integration was carried out by Panov & Sbytov [133] and Korotkii & Obukhov [99] (who arrived at a different conclusion as mentioned in the last paragraph) in the Kristian-Sachs regime of low redshift or small angular frequency  $\omega \ll H_0$ . We perform this integration numerically for arbitrary angular frequencies  $\omega$  and source redshifts  $z$ . We obtain a net shear effect that can be used to obtain limits on these rotating cosmologies by comparing the predicted shear with observed shear values from studies of the weak gravitational lensing effect.

## 5.7 Method

Our aim is to calculate the shear effect on a light bundle from a distant source on its way to the observer in a cosmological model described by the metric (5.12). We do this using the optical transport equations by Sachs [158] and the formalism developed by Seitz et al. [176].

The geodesic of a light ray  $x^\alpha(\lambda)$  can be parametrized by the affine parameter  $\lambda$ . The components of a 4-vector are  $x^0 = ct$ ,  $x^1 = x$ ,  $x^2 = y$ ,  $x^3 = z$ . The wave vector<sup>7</sup>  $\hat{k}^\alpha(\lambda) = \frac{d}{d\lambda} x^\alpha(\lambda)$  obeys  $\hat{k}_\alpha \hat{k}^\alpha = 0$ , and solves the geodesic equation  $\hat{k}_{\alpha;\beta} \hat{k}^\beta = 0$ . In eq. (2.34) we already wrote down the relation that governs the transport of the connection vector

$$\vec{\xi} = D \vec{\theta}, \quad (5.14)$$

where  $D$  is the angular-diameter distance and  $\vec{\theta}$  the angular separation, between two near light rays [13, 176]:

$$\frac{d^2 \vec{\xi}}{d\lambda^2} = \mathcal{T}(\lambda) \vec{\xi}. \quad (5.15)$$

It is important that the light rays are closeby since the expression (5.14) is only valid for small angles. (5.15) follows from the Sachs optical transport equations [158], as shown by Seitz et al.  $\mathcal{T}$  is the tidal matrix

$$\mathcal{T}(\lambda) = \begin{pmatrix} \mathcal{R}(\lambda) - \text{Re } \mathcal{F}(\lambda) & \text{Im } \mathcal{F}(\lambda) \\ \text{Im } \mathcal{F}(\lambda) & \mathcal{R}(\lambda) + \text{Re } \mathcal{F}(\lambda) \end{pmatrix}, \quad (5.16)$$

with

$$\mathcal{R}(\lambda) = -\frac{1}{2} R_{\beta\gamma}(\lambda) \hat{k}^\beta(\lambda) \hat{k}^\gamma(\lambda) \quad (5.17)$$

and

$$\mathcal{F}(\lambda) = -\frac{1}{2} C_{\alpha\beta\gamma\delta} \epsilon^{\alpha*}(\lambda) \hat{k}^\beta(\lambda) \epsilon^{\gamma*}(\lambda) \hat{k}^\delta(\lambda). \quad (5.18)$$

$R_{\beta\gamma}$  and  $C_{\alpha\beta\gamma\delta}$  are the Ricci and Weyl tensors, respectively.  $\epsilon^\alpha(\lambda) = E_1^\alpha(\lambda) + i E_2^\alpha(\lambda)$  is the complex representation of orthonormal bases  $(E_1^\alpha, E_2^\alpha)$  that lie in screens that are spanned by the connection vectors between neighbouring rays  $Y^\alpha$ . The  $Y^\alpha$  are adapted to an observer with a 4-velocity  $U^\alpha$  at an event on the central light ray such that  $k_\alpha Y^\alpha = 0$  and also  $U_\alpha Y^\alpha$ . The asterisk denotes complex conjugation. Once we have chosen such basis vectors at an event, and adapted to an observer with 4-velocity  $U_0^\alpha$ , the basis vectors for all  $\lambda$  can be obtained by transporting them parallelly along the light ray. This was done for a metric related to the Gödel-type metric for observers at rest by Panov & Sbytov [133]. Panov & Sbytov show that distortions of background sources are identical in these two metrics, so that we do not have to construct basis vectors here.

---

<sup>7</sup>Following Seitz et al. [176] we write this wave vector with a hat.

A solution for eq. (5.15) is

$$\vec{\xi}(\lambda) = \mathcal{D}(\lambda)\vec{\theta}_0 \quad (5.19)$$

where  $\vec{\xi}$  is determined from the initial separation  $\vec{\theta}_0$  of the two light rays with the distortion matrix  $\mathcal{D}$ . For a light bundle composed of several such rays, Seitz et al. [176] insert (5.19) in (5.15) and find that the distortion matrix  $\mathcal{D}$  that acts on the light bundle at  $x^\alpha(\lambda)$  can be found by solving the Jacobi differential equation

$$\frac{d^2}{d\lambda^2}\mathcal{D}(\lambda) = \mathcal{T}(\lambda)\mathcal{D}(\lambda). \quad (5.20)$$

By solving this equation with the boundary conditions,

$$\mathcal{D}(0) = 0, \quad \frac{d\mathcal{D}}{d\lambda}(0) = \begin{pmatrix} 1 & 0 \\ 0 & 1 \end{pmatrix}, \quad (5.21)$$

we can calculate the distortion effect of the universe on a light bundle propagating from the observer at  $\lambda = 0$ . The first boundary condition states that  $\vec{\xi}(0) = 0$ . The second condition states that at the observer angular-diameter distance and affine parameter distance are identical, or that  $\frac{d}{d\lambda}\vec{\xi}(t_0) = \vec{\theta}_0$ .

## 5.8 Affine parameter-redshift relation

In their analytical study of the Gödel-type metric, Panov & Sbytov [133] did not use the metric (5.12), but transformed it into the stationary metric

$$d\tilde{s}^2 = c^2 d\tau^2 - 2c\sqrt{\sigma}e^{mx} d\tau dy - (dx^2 + ke^{2mx} dy^2 + dz^2). \quad (5.22)$$

They show that the connection vectors  $\vec{\xi}$  of a light bundle in this space are related to the connection vectors  $\vec{\xi}$  in the Gödel-type metric by

$$\vec{\xi}(\lambda') = \frac{1}{R(t(\lambda))}\vec{\xi}(\lambda). \quad (5.23)$$

We use the same angle  $\vec{\theta}_0$  between neighbouring rays in both metrics, so that eq. (5.19) gives

$$\tilde{\mathcal{D}}(\lambda) = \frac{1}{R(t(\lambda))}\mathcal{D}(\lambda). \quad (5.24)$$

We can recover the distortion matrix of the Gödel-type metric by multiplying  $\tilde{\mathcal{D}}$  with  $R(t(\lambda))$ .

In order to get an intuition for these metrics, it is instructive to study how sources appear redshifted if they are situated at certain positions on a light path, as parametrized by the affine parameter. In the metric (5.22), Panov & Sbytov parametrize light rays by a primed affine parameter  $\lambda'$ . If the light ray was parametrized by the parameter  $\lambda$  in the Gödel-type model, we have

$$\frac{d\lambda'}{d\lambda} = \frac{1}{R^2(t(\lambda))}, \quad (5.25)$$

where  $t(\lambda)$  is the age of the universe in the Gödel-type metric at the time when the light ray reaches the point parametrized by  $\lambda$ . The cosmological redshift  $z(\lambda)$  as measured by an observer with 4-velocity  $U^\alpha$  at an event  $\lambda$  is defined by (for example [176])

$$z(\lambda) = -\hat{k}^\alpha(\lambda) U_\alpha(\lambda) - 1. \quad (5.26)$$

For an observer at rest,

$$U^\alpha = (1, 0, 0, 0), \quad (5.27)$$

in the Gödel-type model this is identical to the result for the Robertson-Walker metric,

$$z = \frac{R_0}{R} - 1, \quad (5.28)$$

where  $R_0 = R(t_0)$  is the cosmic scale factor at the present epoch ( $t_0$  is the age of the universe, see eq. (5.29)). We choose  $R_0 = 1$  for all our calculations [13]. The redshift depends on the dynamical realization we choose for the universe. The Gödel-type models have a cosmological constant, and exotic cosmological “fluids” have been proposed for the “matter” content. Korotky & Obukhov [100] describe a plethora of beautiful dynamical realizations for these models that are known not only in Einstein’s general relativity theory, but also in other gravity theories. For our calculations, we only need a parametrization for the scale factor  $R(t)$  from these theories.

The dynamical evolution of the models we consider here can be described by

$$R(t) = R_0 \left( \frac{t}{t_0} \right)^b, \quad (5.29)$$

where  $t_0$  is the age of the universe. The Hubble constant  $H_0$  is thus given by

$$H_0 = \left. \frac{\dot{R}}{R} \right|_{t=t_0} = \frac{b}{t_0}. \quad (5.30)$$

Using (5.25), we proceed to write down the differential equation for the affine parameter as a function of  $z$ :

$$\frac{d\lambda'}{dz} = \frac{d\lambda'}{d\lambda} \left( \frac{dz}{d\lambda} \right)^{-1} = \frac{1}{R^2} \left( \frac{dz}{d\lambda} \right)^{-1}. \quad (5.31)$$

The latter derivative can be found with the help of eqs. (5.28) and (5.29),

$$\frac{dz}{d\lambda} = \dot{z} \frac{dt}{d\lambda} = -\frac{1}{c} \hat{k}^0 \frac{R_0}{R^2} \dot{R} = -\frac{1}{c} \hat{k}^0 H_0 \left( \frac{R_0}{R} \right)^{1+\frac{1}{b}}. \quad (5.32)$$

The wave vector  $\hat{k}^\alpha$  was computed by [133] and [99]. The second paper describes it in terms of spherical coordinates, which we give here for the purpose of illustrating the quantities that describe the geodesics:

$$\hat{k}^\alpha(\lambda) = -\frac{R_0}{R} \left( 1 + \sqrt{\frac{\sigma}{k + \sigma}} \sin \theta \sin \Phi, \frac{1}{R} \sin \theta \cos \Phi, \frac{e^{-mx}}{R \sqrt{k + \sigma}} \sin \theta \sin \Phi, \frac{1}{R} \cos \theta \right). \quad (5.33)$$

$\theta$  and  $\phi$  (used later) are the usual spherical polar coordinates describing the direction of the light ray at the observer. The cosmic rotation axis (of the observer) corresponds to  $\theta = 0$ . These coordinates are not adapted to the rotational symmetry of the metric, however, so that the expressions and solutions we derive depend on  $\theta$  and  $\phi$ . A suitable transformation for the Gödel metric that reveals the symmetry about the rotation axis was given by Gödel [58]. For the Gödel-type metric, this transformation needs to be generalized.

The function  $\Phi$  satisfies the differential equation

$$\frac{d}{dt}\Phi = -\frac{m c}{R} \left( \frac{\sqrt{\frac{\sigma}{k+\sigma}} + \sin \theta \sin \Phi}{1 + \sqrt{\frac{\sigma}{k+\sigma}} \sin \theta \sin \Phi} \right). \quad (5.34)$$

Eqs. (5.31) and (5.34) (the latter multiplied by  $\hat{k}^0$ ) form a set of differential equations than can be solved analytically up to linear order in  $z$  [133],

$$\lambda' = \frac{cz/H_0}{1 + \sqrt{\frac{\sigma}{k+\sigma}} \sin \theta \sin \phi}. \quad (5.35)$$

$\lambda'$  depends both on  $\theta$  and  $\phi$  (see [100]). In this coordinate system, the smallest values for  $\lambda'(z)$  in the plane perpendicular to the cosmic rotation axis, the so-called equatorial plane where  $\theta = \frac{\pi}{2}$ , are expected in the direction of  $\phi = \frac{\pi}{2}$ .

In order to obtain  $\lambda'$  for all  $z$ , it is possible to solve the equations numerically. The boundary conditions are  $\lambda'(0) = 0$  and  $\Phi(0) = \phi$ . In Fig. 5.1, we used Mathematica [208] to calculate  $\lambda'(z)$  for the Robertson-Walker model and several rotating Gödel-type cosmological models. It can be taken from this figure that light paths in rotating metrics can be longer than in the Robertson-Walker universe. The parameter combination  $\frac{\sigma}{k+\sigma}$  drops in these curves from 0.91 (blue, red), over 0.5 (green) and 0.09 (cyan) to 0 (magenta). It is interesting to note that it seems that increasing this parameter leads to larger affine parameters for a given redshift. Since the universal rotation value  $\omega$  is proportional to  $\sqrt{\frac{\sigma}{k+\sigma}}$ , it can be interpreted that it is possible to increase the light paths to a given redshift by “spinning up” the universe. However, for low redshifts and  $\theta, \phi \neq 0$ , this is not true as can be seen from eq. (5.35). In this case, the corresponding graphs would have crossed before  $z \approx 1$ .

## 5.9 Parameter space

Before we set foot on the terrain of abstract parameters of the Gödel-type metrics, it is helpful to understand what properties of a given model are governed by the three parameters  $k$ ,  $\sigma$  and  $m$  that determine the Gödel-type metrics. In eq. (5.13) we gave the expression for the parameter  $\omega = \frac{m c}{2} \sqrt{\frac{\sigma}{k+\sigma}}$  that is a measure for the rotation of the universe around observers at rest. It can be seen from this equation that there is no rotation if  $m$  or  $\sigma$  vanish.

Panov & Sbytov [133] give the components of the tidal matrix  $\tilde{\mathcal{T}}$  (eq. (5.16)) (the tilde denotes that we work here with the metric (5.22) rather than the Gödel-type metric) for the metric (5.22) for circular sources:

$$\tilde{\mathcal{R}} = \frac{m^2}{4} |\cos \theta| \frac{\sigma + 2k(1 - \cos^2 \theta)}{k + \sigma} \quad (5.36)$$

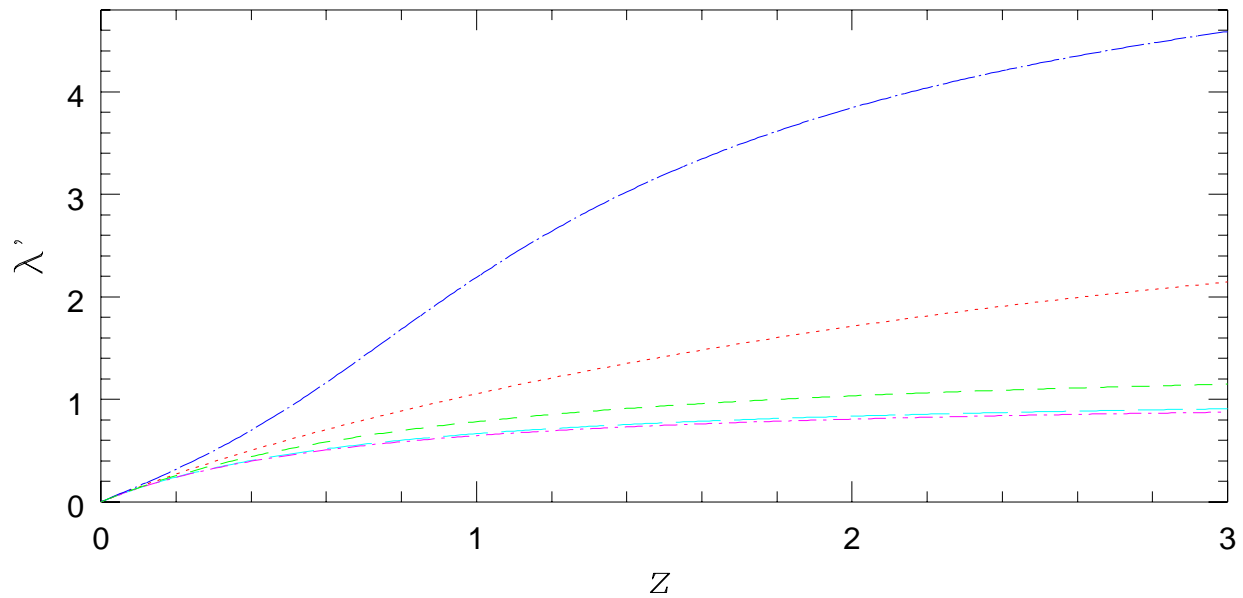


Figure 5.1: Affine parameter-redshift relation in a rotating universe. All rays propagate in the equatorial plane,  $\theta = \frac{\pi}{2}$ ,  $\phi = 0$ . The models differ in the parameter tripels  $(k, \sigma, m)$ : (from top to bottom) long dash-dotted curve  $(0.1, 1, 2)$ , dotted curve  $(0.1, 1, 1)$ , short dashed curve  $(1, 1, 1)$ , long dashed curve  $(1, 0.1, 1)$  and short dash-dotted curve  $(1, 0, 0)$ .  $m$  is given in units of  $(ct_0)^{-1}$ . From top to bottom the parameter combination  $\frac{\sigma}{k+\sigma}$  drops from 0.91 (long dash-dotted,dotted), over 0.5 (short dashed) and 0.09 (long dashed) to 0 (short dash-dotted). The short dash-dotted curve corresponds to an  $\Omega_\Lambda = 0$  Robertson-Walker universe.



and

$$\tilde{\mathcal{F}} = \frac{k m^2}{k + \sigma} \sin^2 \theta e^{\pm i m \sqrt{\frac{\sigma}{k+\sigma}} |\cos \theta| \lambda'} \quad (5.37)$$

where the upper sign corresponds to  $|\cos \theta| > 0$  and the lower to  $|\cos \theta| < 0$ .

As can be seen from eq. (5.16), the distortion effect on a light bundle is zero when  $\tilde{\mathcal{F}} = 0$  since in this case  $\tilde{\mathcal{T}}$  becomes proportional to the unit matrix. However, from eq. (5.37), we can see that there can still be light bundle distortion even if  $\sigma = 0$ . If  $k = 0$ , however, this implies a symmetric tidal matrix  $\tilde{\mathcal{T}}$ , so that there is no light bundle distortion although the universe is rotating. As was mentioned before, however, in order to only look at causal space-times we only consider models with  $k > 0$  [100].

In the expressions relevant for our study, namely (5.36), (5.37), (5.34) and  $\tilde{k}^0$  in (5.33),  $k$  and  $\sigma$  always appear in company in the form of the ratios  $\frac{\sigma}{k+\sigma}$  and  $1 - \frac{\sigma}{k+\sigma} = \frac{k}{k+\sigma}$ , so that they have a combined effect. For a parameter search, it is thus sufficient to study the parameter space of  $m$  and

$$f = \frac{\sigma}{k + \sigma}. \quad (5.38)$$

## 5.10 Model zoo and results

Now we solve eq. (5.20) for the distortion matrix  $\tilde{\mathcal{D}}$ ,

$$\frac{d^2}{d\lambda'^2} \tilde{\mathcal{D}}(\lambda') = \tilde{\mathcal{T}}(\lambda') \tilde{\mathcal{D}}(\lambda') \quad (5.39)$$

with the boundary conditions

$$\tilde{\mathcal{D}}(0) = 0, \quad \frac{d\tilde{\mathcal{D}}}{d\lambda'}(0) = \begin{pmatrix} 1 & 0 \\ 0 & 1 \end{pmatrix}, \quad (5.40)$$

in order to estimate the distortion of sources at several redshifts for comparison with observations. The tilde denotes again that we work here with the metric (5.22) and have to transform it later back to recover the distortion matrix  $\mathcal{D}$  for the Gödel-type metric (5.12). The solution of (5.39) can be done numerically in a straightforward manner using the differential equation solver in Mathematica [208], so that we will not pursue analytical solutions of this problem.

Our aim is to illustrate how weak lensing can be used as a test of rotating cosmologies. We will pick two directions in the equatorial plane where the largest distortion is expected according to eq. (5.37). In Sect. 5.8, we found an additional dependence on the azimuthal angle  $\phi$ , such that the smallest affine parameters  $\lambda'$  as a function of redshift were reached by light rays in the direction  $\phi = \frac{\pi}{2}$  for small  $z$ . We experimented with this value in the case of large  $z$  and found this result still to hold at least for parameters  $m \leq 3$ . Since (5.36) and (5.37) do not depend on  $\phi$ , we can find the lowest distortion in the equatorial plane in the direction  $\phi = \frac{\pi}{2}$ . In addition, we study the directions  $\phi = 0$  and  $\phi = \frac{3}{2}\pi$ , which give us somewhat higher distortions. These directions give an impression of the magnitude of distortions in these cosmologies. The direction  $\phi = \frac{3}{2}\pi$

has the highest distortion on the sky. Since our limits from the weak lensing studies (Sect. 5.5) do not cover the whole sky, we cannot be sure that we really have a limit on this direction.

The distortion matrix  $\mathcal{D}(\lambda)$  (eq. (5.19)) describes the deformation of a light bundle as it passes through the universe. We can take out the physical scale of the light bundle by normalizing  $\mathcal{D}$  with the determinant

$$\sqrt{\det \tilde{\mathcal{D}}} = \sqrt{\tilde{D}_1 \tilde{D}_4 - \tilde{D}_2 \tilde{D}_3}, \quad (5.41)$$

which is the angular diameter distance along the beam considered [176]. The shear  $\gamma$  can be obtained from  $\tilde{\mathcal{D}}/\sqrt{\det \tilde{\mathcal{D}}}$  according to eq (2.22). Although we worked in the transformed metric (5.22), the normalization with  $\sqrt{\det \tilde{\mathcal{D}}}$  allows us to use

$$\tilde{\mathcal{D}} = \begin{pmatrix} \tilde{D}_1 & \tilde{D}_2 \\ \tilde{D}_3 & \tilde{D}_4 \end{pmatrix}, \quad (5.42)$$

to calculate the shear

$$\gamma = \frac{1}{2} \sqrt{\frac{(\tilde{D}_1 - \tilde{D}_4)^2 + (\tilde{D}_2 + \tilde{D}_3)^2}{\tilde{D}_1 \tilde{D}_4 - \tilde{D}_2 \tilde{D}_3}}. \quad (5.43)$$

As an example, we have plotted in Fig. 5.2 the shear  $\gamma$  as a function of the redshift  $z$  for the models from Fig. 5.1. We find that for small redshifts  $z$  the numerical results can be well represented by the analytical relation

$$\gamma(z) = \frac{1}{1 + \frac{9}{\sqrt{2}} \frac{k+\sigma}{k} \left(\frac{b}{mz}\right)^2}. \quad (5.44)$$

For  $\gamma < 1$  we may calculate the axis ratio  $p = (1 + \gamma)/(1 - \gamma)$  (see eq. (2.22) and the following paragraphs):

$$p(z) = 1 + \frac{2\sqrt{2}}{9} \frac{k}{k + \sigma} \left(\frac{mz}{b}\right)^2. \quad (5.45)$$

The existence of a relation like this for an arbitrary space-time was shown by Kristian and Sachs [101] (eq. (5.7)).

We calculate the shear values by converting the redshifts into affine parameters by the method outlined in Sect. 5.8, and then using the solutions of eq. (5.20) to find the corresponding shear values. Eq. (5.20) can also be rewritten as a differential equation in  $z$ ,

$$\frac{d^2 \mathcal{D}}{dz^2} \left(\frac{dz}{d\lambda}\right)^2 + \frac{d\mathcal{D}}{dz} \frac{d^2 z}{d\lambda^2} = \mathcal{T}(z) \mathcal{D}(z). \quad (5.46)$$

This can be implemented by inserting the derivatives according to eqs. (5.31) and (5.32), and by using the geodesic equation for  $d^2 t/d\lambda^2$ . In our case, we wanted to have both  $\lambda'(z)$  and  $\mathcal{D}(z)$ , so that we perform the calculation in two steps. Mathematica allowed to save the  $\lambda'(z)$  for our model grids as tables and work with these in the next step, which made the procedure tractable.

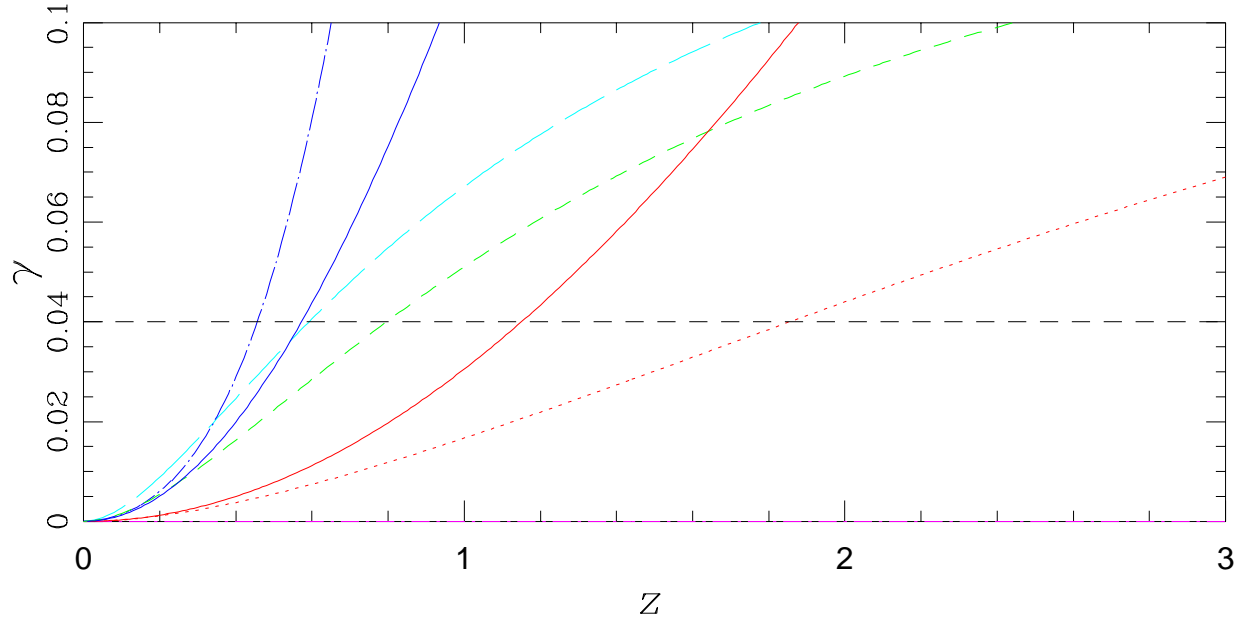


Figure 5.2: Shear  $\gamma$  as a function of the redshift  $z$  for all models from Fig. 5.1: all rays propagate in the equatorial plane,  $\theta = \frac{\pi}{2}$ ,  $\phi = 0$ . The models differ in the parameter pairs  $(\frac{\sigma}{k+\sigma}, m)$ : long dash-dotted curve (0.91, 2), dotted curve (0.91, 1), short dashed curve ( $\frac{1}{2}$ , 1), long dashed curve (0.09, 1) and short dash-dotted curve (0, 0).  $m$  is given in units of  $(ct_0)^{-1}$ . The short dash-dotted line corresponds to an  $\Omega_\Lambda = 0$  Robertson-Walker universe, and is everywhere zero. The long dash-dotted model has such high distortions that it leaves the displayed range of  $\gamma$  space already at  $z \approx 0.65$  and reaches  $\gamma = 2.15$  at  $z = 3$ . For two models (dotted and long dash-dotted) the Kristian-Sachs [101] type analytical approximations  $\gamma = 1 / \left( 1 + \frac{9}{\sqrt{2}} \frac{k+\sigma}{k} \left( \frac{b}{mz} \right)^2 \right)$  are plotted as solid curves. The horizontal dashed line depicts the current limit on cosmic shear  $\gamma_{\text{limit}} \leq 0.04$  as measured from background galaxies with redshifts  $z \gtrsim 0.7$ .

We have calculated observational limits by scanning the parameter space of  $f$  and  $m$ . This is shown in Figs. 5.3 and 5.4. In these figures, we keep  $\theta = \frac{\pi}{2}$  fixed and determine shear values  $\gamma$  for background sources at a redshift of  $z = 1$ . The shear values are greyscale coded into 6 regions, with dividing contours at  $\gamma = 0.04, 0.07, 0.1, 0.3$  and  $0.5$ . We now give some more detailed comments on the figures:

- In Fig. 5.3 we scanned this parameter space for  $\phi = \frac{\pi}{2}$  (upper panel),  $\phi = 0$  (lower left panel) and  $\phi = \frac{3}{2}\pi$  (lower right panel), where all figures are calculated with the Robertson-Walker type expansion parameter  $b = \frac{2}{3}$ . Note that in the upper panel ( $\phi = \frac{\pi}{2}$ ) the excluded region is situated in the upper left corner of small  $f$ . In the lower panels for  $\phi = 0$  and  $\phi = \frac{3}{2}\pi$ , it seems to be more the right region with high  $f$  that is excluded. We investigated this and found that as the distortion effect is tuned up, the exclusion region develops into a convex region that moves to lower  $m$ , becoming more stringent at higher  $f$  as  $\phi$  approaches  $\phi = 0$ . This is an unexpected answer to the prediction by Korotkii & Obukhov [99] that the distortion effect would not be significant for models with  $k \ll \sigma$ . This was a natural prediction since, for example,  $\mathcal{F}(\lambda')$  in eq. (5.37) is proportional to  $\frac{k}{k+\sigma}$ . For certain  $m$ , however, the effect is counteracted by a strong increase of  $\lambda'$  with redshift. The mechanism becomes clear if we solve eq. (5.20) analytically: for  $\theta = \frac{\pi}{2}$   $\mathcal{R}(\lambda')$  is zero and  $\mathcal{F}(\lambda')$  is constant. It is found that  $\mathcal{D}_1 - \mathcal{D}_4$  increases exponentially with  $\lambda'$ ! Note that this also means that  $\gamma(\lambda')$  is analytically solvable for  $\theta = \frac{\pi}{2}$ . With this we were able to cross-check all our results both analytically and numerically.
- In Fig. 5.4 we kept  $\phi = \frac{\pi}{2}$  and changed  $b$  from  $b = \frac{2}{3}$  (upper panel, identical to the upper panel in Fig. 5.3) to  $b = \frac{1}{2}$  (lower left panel) and  $b = 1$  (lower right panel). By comparing these two panels with the upper panel, the effect of the parameter  $b$  can be seen: the distortion becomes weaker and the limits get less stringent in a faster expanding universe.

The regions we can rule out in Figs. 5.3 and 5.4 from weak lensing observations are the regions that are not black. We now restrict ourselves to the models in Fig. 5.3, where we derive limits of

$$m \lesssim 0.9 + 2.1 f \quad (5.47)$$

for  $\phi = \frac{\pi}{2}$  (upper panel), and

$$m \lesssim 0.8 + 0.7 f \quad (5.48)$$

for  $\phi = 0$  (lower left panel), where  $m$  is measured in units of  $(ct_0)^{-1}$ . The limits for  $\phi = \frac{3}{2}\pi$  (lower right panel) are

$$m \lesssim 0.8 - 0.7 f \quad (5.49)$$

For  $\phi = \frac{3}{2}\pi$ , we could get even better limits on  $m$  for  $f > 0.9$  since  $m = 0.1$  is just the lower boundary of the parameter space we scanned. However, we already mentioned that the measured shear values from weak lensing studies are too sparsely sampled to be compared with this direction since has the highest distortion on the sky. We included it here to illustrate the distortion effect in this direction.

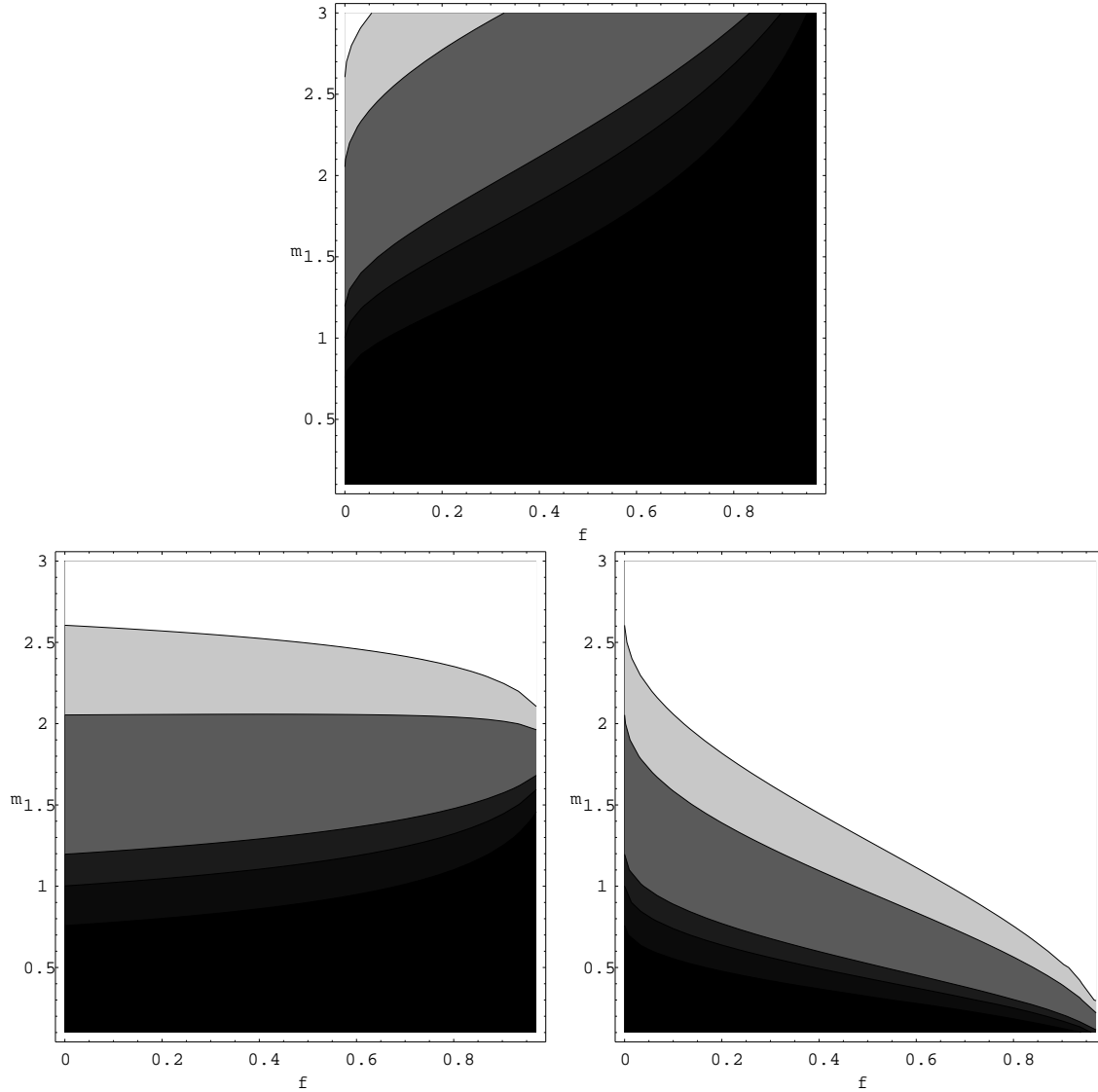


Figure 5.3: Predicted shear values for background sources at a redshift of  $z = 1$  in Gödel-type rotating universes. We have scanned  $30 \times 30$  models in the parameter space of  $0 < f = \frac{\sigma}{k+\sigma} < 0.97$  and  $0.1 < m < 3$  and determined the expected shear  $\gamma$ . The direction of the light bundle at the observer was described by the spherical coordinate  $\theta = \frac{\pi}{2}$  (equatorial plane). We also fix the parameter  $b = \frac{2}{3}$ .  $b$  characterizes the development of the scale factor with time, as defined in eq. (5.29). We tested this parameter space for three angles  $\phi = \frac{\pi}{2}$  (upper panel),  $\phi = 0$  (lower left), and  $\phi = \frac{3}{2}\pi$  (lower right).  $m$  is given in units of  $(ct_0)^{-1}$ . The shear values are colour coded into six regions: the five contours correspond to values of  $\gamma = 0.04, 0.07, 0.1, 0.3$  and  $0.5$ . In some cases not all contours are reached. Models with shear values  $\gamma > 0.04$  are ruled out, the black region contains the allowed models.

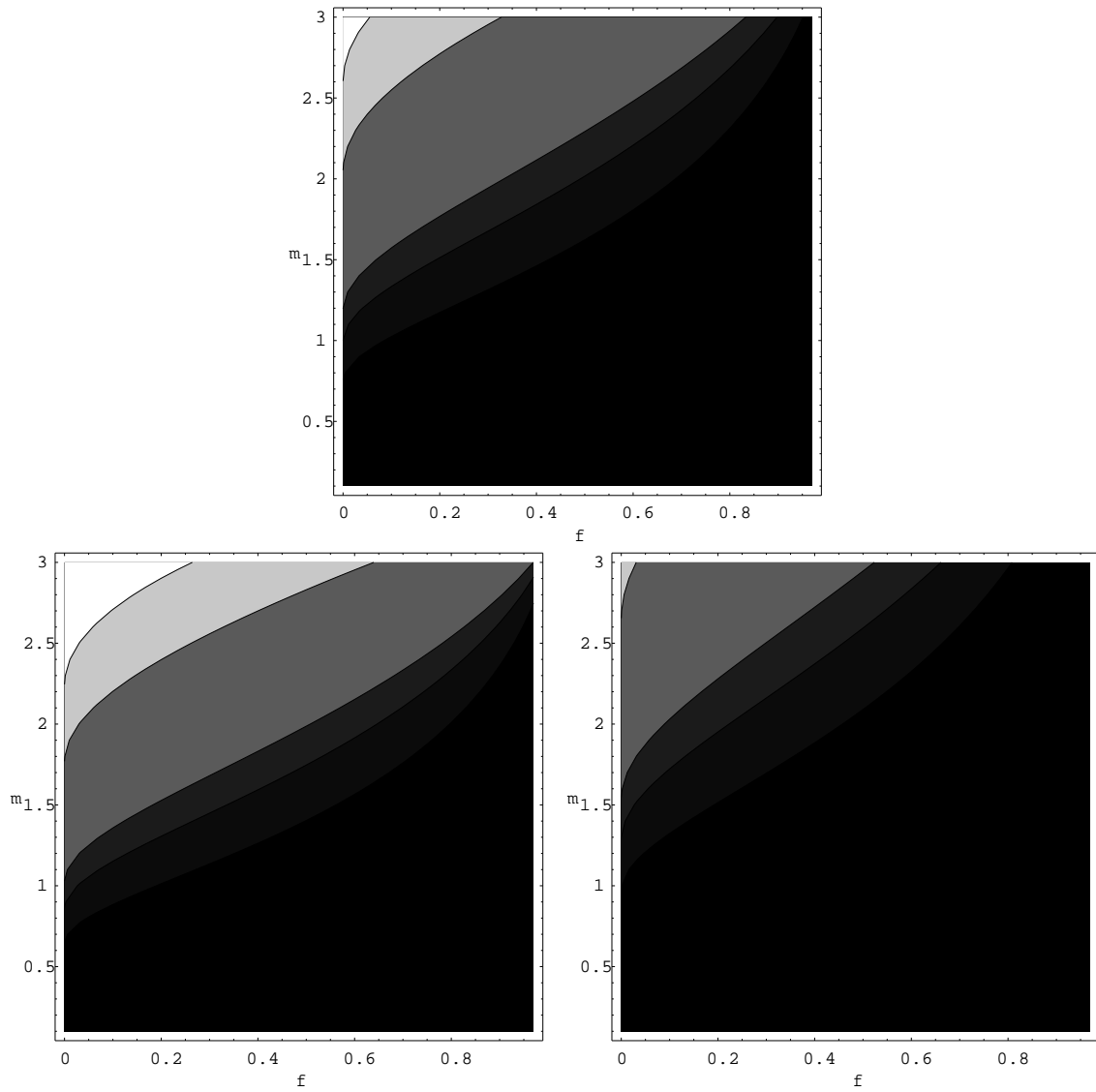


Figure 5.4: Same as Fig. 5.3, except this time we tested three values  $b$  and fixed  $\phi = \frac{\pi}{2}$ . In detail, the models are  $b = \frac{2}{3}$  (upper panel),  $b = \frac{1}{2}$  (lower left), and  $b = 1$  (lower right). The upper panel is identical to the upper panel in Fig. 5.3.  $m$  is given in units of  $(ct_0)^{-1}$ .

## 5.11 Conclusion

In this chapter, we have shown that weak lensing can put constraints on the Gödel-type rotating universes that otherwise seem untouched by current observations [100]. We have used the observational evidence from weak lensing studies that the cosmic shear of background galaxies is less than  $\gamma_{\text{limit}} = 4$  percent. The sampling of the sky is still very sparse. We note that we cannot exclude the existence of high-distortion regions with  $\gamma > \gamma_{\text{limit}}$  on the sky that have so far not been found.

For the Gödel-type metric the cosmic rotation at the observer is given by  $\omega = \frac{m.c}{2} \sqrt{\frac{\sigma}{k+\sigma}}$ . We obtain limits on the square root  $\sqrt{\frac{\sigma}{k+\sigma}}$  and  $m$  from a detailed parameter study. Concentrating on a Robertson-Walker type expansion

$$R(t) = R_0 \left( \frac{t}{t_0} \right)^{\frac{2}{3}}, \quad (5.50)$$

we calculated limits on the cosmic rotation for three directions in the “equatorial plane”. This is the plane that is perpendicular to the cosmic rotation axis. In this plane, the distortion depends on the azimuthal angle  $\phi$  (we use the coordinate system and description of the geodesics by [99]). We chose the azimuthal angles  $\phi = \frac{\pi}{2}$ ,  $\phi = 0$  and  $\phi = \frac{3}{2}\pi$ .

Since  $0 < \sqrt{\frac{\sigma}{k+\sigma}} < 1$ , and by writing  $m$  in units of  $(c t_0)^{-1}$ ,  $\omega$  can be estimated with the help of eq. (5.30) as

$$\omega < \frac{3}{4} m H_0. \quad (5.51)$$

From eqs. (5.47), (5.48) and (5.49), we thus obtain for a Hubble constant of  $60 \text{ km s}^{-1} \text{ Mpc}^{-1}$

$$\omega < 2.3 H_0 = 1.4 \times 10^{-10} \text{ yr}^{-1} \quad (5.52)$$

for  $\phi = \frac{\pi}{2}$ ,

$$\omega < 1.1 H_0 = 6.9 \times 10^{-11} \text{ yr}^{-1} \quad (5.53)$$

for  $\phi = 0$  and

$$\omega < 0.6 H_0 = 3.7 \times 10^{-11} \text{ yr}^{-1} \quad (5.54)$$

for  $\phi = \frac{3}{2}\pi$ . In order to produce simple limits, we always assumed the least favourable value for  $\frac{\sigma}{k+\sigma}$  here. For a given  $\frac{\sigma}{k+\sigma}$ , an exact limit can be calculated from the linear relations in eqs. (5.47), (5.48) and (5.49).

Compared to the limits from the cosmic microwave background (Sect. 5.3), these limits are orders of magnitude less stringent. However, unless we allow for very high cosmic shear values in directions that have not been studied by weak lensing analyses so far, our results suggest that cosmic rotation rates with  $\omega \sim H_0$  are ruled out. For a more rigorous argument, one could combine several observations with their relative positions on the sphere, and determine the expected shear values at all positions for many different orientations of the rotation axis with a Monte-Carlo method. The resulting probability distribution could then be used to decisively probe the

parameter space. Such a combined analysis should be done with a sample that was produced with a uniform analysis technique, such as the six Wilson et al. [204] fields, since this would ensure that all shear values are in fact comparable. For even better constraints, the fields should have a special geometry, such as measurements on two poles, and at four points in the equatorial plane corresponding to  $\phi = 0, \frac{\pi}{2}, \pi$  and  $\frac{3}{2}\pi$ . Since this is not possible to do with a single telescope, one could relax the constraints and use only one pole and a pattern of four positions at  $\theta = \frac{1}{3}\pi$ , or even arrange the pattern in a way that the observations can be done during one observing run.

There is no evidence for cosmic rotation from birefringence measurements that show the dependence

$$\Delta \sim z^2 \sin^2 \theta. \quad (5.55)$$

that Panov & Sbytov [133] obtain for the rotation angle  $\Delta$  between the major elongation axis and the direction of the average polarization for sources at a redshift  $z$  with an angular distance  $\theta$  from the rotation axis  $\theta = 0$ . Birch (5.1) and Nodland & Ralston (5.2) find different relations than (5.55). In particular, the high cosmic rotation values obtained by [123, 124] on the basis of these data (see Sect. 5.6) were obtained with a different formalism and cannot be compared with our values.

Our results show that weak lensing is a strong test for rotating cosmologies that rotate at substantial rates  $\omega \approx H_0$ . The lensing signal from more slowly rotating cosmologies is disturbed, however, by the lensing effect of the large-scale distribution of matter in the universe.



# Chapter 6

## Summary and Outlook

### Gravitational lensing as a tool for cosmology

In the more than twenty years since the gravitational lens effect was first observationally discovered it has become a versatile cosmological tool. Not only has the number of known gravitational lens systems grown large enough to provide a diverse pool of lens laboratories. The published data from large monitoring programs also now make it possible to perform long-term studies of the temporal properties of individual lens systems. Moreover, the field of weak gravitational lensing boomed in the 90s due to theoretical and observational advances, especially regarding theoretical inversion techniques and wide-field imaging detectors, so that we now begin to observe the gravitational lens effect in almost every direction on the sky.

The power of gravitational lensing lies in the geometrical nature of the light deflection. Various cosmological parameters, such as the value of the Hubble constant  $H_0$  or the value of the cosmological constant  $\Omega_\Lambda$  are accessible to lensing because they influence the geometry of the universe, and thus the geometry of every gravitational lens. The large-scale matter distribution of the universe itself betrays its presence by slightly distorting the images of background galaxies.

In chapters 3 and 4 of this thesis we use the geometry of the double quasar Q0957+561 (Fig. 2.2 on page 8) and the quadruple quasar Q2237+0305 (Fig. 2.3 on page 11) to search the lensing galaxies for compact objects close to each light path to the quasars. Due to the relative motion of observer, lens galaxy, and quasar, the compact objects in the lensing galaxy cause flux variations of the background quasar by their microlensing effect on the quasar light bundle. The multiple images then allow us to separate intrinsic fluctuations of the quasars from microlensing fluctuations because intrinsic fluctuations of the quasar are seen in all images, with a certain time-delay due to the difference in the light paths.

In chapter 5 we study the gravitational distortion effect on light bundles in a unique class of cosmological models with universal rotation. These models cannot be ruled out by the isotropy of the cosmic microwave background radiation, and have also currently not been ruled out by other observations [100]. Contrary to the case of Robertson-Walker universes, light bundles are distorted in these models, so that circular sources would appear as ellipses on the sky. With the techniques developed to measure the weak gravitational lensing effect of galaxy clusters and the large-scale structure of the universe, this light bundle distortion can be tested. The gravitational

lensing effect proves to be a useful tool to place limits on the cosmic rotation in these models.

We now summarize our results and outline some lines of future research.

### **Limits on MACHOs from microlensing in Q0957+561**

In chapter 3 we study the difference between the two images of the double quasar Q0957+561 over a three year period using data from the Apache Point Observatory [34] and obtain mass limits on possible compact objects in the galaxy halo (MACHOs) from the remaining variations. Since the light paths of the two quasar images have a time-delay of  $\Delta t = 417$  days [105], one of the light curves was shifted by  $\Delta t$  to match the variations of the other quasar image. From the difference between the two quasar light curves we derive exclusion limits for MACHO masses. The effect of different MACHO masses on the microlensing variability is illustrated in Fig. 3.4 on page 31. In addition the exclusion limits depend on the size of the optical continuum emitting region of the quasar. In Fig. 3.6 on page 40 our limits are compiled for a galaxy halo consisting entirely of MACHOs. In short, we can exclude MACHO masses from  $10^{-6} M_{\odot}$  up to  $10^{-2} M_{\odot}$  for quasar sizes of less than  $3 \times 10^{14}$  cm if the MACHOs make up at least 50% of the dark halo. These mass limits are consistent with the recently published result by Alcock et al. [5]. They find that the most likely mass of MACHOs in the halo of our galaxy responsible for between 13 and 17 microlensing events of stars in the Large Magellanic Cloud is of the order of a few tenths of a solar mass, if the objects are situated in the galaxy halo.

In the 17 year observational record of Q0957+561 used by Pelt et al. [135] no significant microlensing variations were detected over the last ten years. In the first years of the observations of Q0957+561, however, a brightness drop of about 0.3 mag was seen in the Pelt et al. [135] difference light curve. The drop would be consistent with a brightness peak in the quasar image B that is situated at a projected separation of  $5.2 h_{60}^{-1}$  kpc from the galaxy centre. Since the two quasars are seen through the galaxy, we expect in fact to observe a microlensing signal from the stars in the galaxy. The Pelt et al. event had its minimum at the end of 1982 and was sampled rather sparsely. For such events, the analysis used in chapter 3 is not appropriate because the peak height and peak duration will be important parameters. It would be exciting to study such events with the high time resolution currently reached at Apache Point Observatory. In the lens system discussed next, strong microlensing variations are already observed now with high time resolution.

### **Microlensing in the quadruple quasar Q2237+0305**

In chapter 4 we present independent evidence for microlensing in the quadruple quasar Q2237+0305 using three years of Apache Point Observatory (APO) data. We present the reduction of 73 nights of observations of this system. The reduction procedure is difficult because the frames were obtained under seeing between 1.2 and 2.4 arcseconds with a detector pixel size of 0.6 arcsec. The relative separations of the four gravitational images of the quasar are less than 2 arcsec, and they are situated in a cruciform geometry around the peaked core of the lensing galaxy (Fig. 4.1 on page 4.1). Photometry of the two brighter quasar images is possible thanks

to extremely precise astrometry from UV Hubble Space Telescope observations [22] of the four images and the galaxy core.

We employ two different reduction schemes. The results are shown in Fig. 4.7 on page 57. Both schemes yield similar light curves that are consistent within the error bars. In the data from 1996 (middle panel) a brightness peak of image A with an amplitude of 0.4 to 0.5 mag is seen. Images C and D cannot be detected with any significance because the noise is too high.

This result fits well with the strong microlensing variations of more than a magnitude on time scales of 700 days detected in Q2237+0305 by the OGLE team [209] who have monitored the system since 1997. Their most recent data can be looked at at [www.astro.princeton.edu/~ogle/ogle2/huchra.html](http://www.astro.princeton.edu/~ogle/ogle2/huchra.html).

The APO and OGLE monitoring observations since 1995 clearly show that Q2237+0305 is a prime target for measuring the mass function of microlenses in other galaxies by comparing the observations with numerically simulated microlensing light curves such as presented in chapter 3 using the Wambsganss [190] code, or that can be calculated with the techniques by Witt [206], Lewis et al. [108] or Wyithe & Webster [211]. It is also ideally suited to study the quasar during high-magnification events using spectra and photometry in as many wavebands (radio, optical, and X-ray regimes) as possible to put constraints on the structure of the optical continuum emitting region of the quasar accretion disk.

### Limits on universal rotation from weak gravitational lensing

In chapter 5 we study the deformation of light bundles in a class of metrics called Gödel-type metrics (for example [100]). These metrics are generalizations of a metric originally described by Gödel [58]. The metrics describe a homogeneous universe in which the vorticity tensor at the position of each observer is not zero, so that the observer perceives a rotating universe. Although each individual observer has a cosmic rotation axis, no anisotropy is imprinted on the cosmic microwave background radiation in these models. Contrary to the original Gödel model, the Gödel-type models do even not have closed timelike curves. They also have cosmic expansion.

Using the deformation tensor of light bundles calculated by Panov & Sbytov [133] for these models, we calculate the expected distortion (shear) of background sources as a function of redshift with the formalism by Seitz, Schneider & Ehlers [176]. Shear detections as well as limits on the shear of background galaxies are available in the literature of weak gravitational lensing for several fields on the sky [174, 203]. From these studies, we find an upper limit  $\gamma_{\text{limit}} = 0.04$  on the cosmic shear. Since the shear measurements are only available for a few fields on the sky, we cannot exclude high-shear regions due to a rotating universe everywhere on the sky. If we assume that the current values are in fact upper limits on the cosmic shear, we find for the value  $\omega$  of the cosmic rotation  $\omega \lesssim H_0$ .

Although the Gödel-type models do not imprint any anisotropy on an ideal homogeneous cosmic microwave background, we find that the models for some parameter choices predict significant shear values for high redshifts. Since anisotropies at the  $10^{-5}$  level have been detected in the cosmic background radiation [179], cosmic rotation will also have an effect on the observed CMB anisotropies. The satellite missions MAP and Planck will map cosmic microwave background anisotropies and will thus also be able to test Gödel-type rotating cosmologies.

# Bibliography

- [1] Agol E., Krolik J., 1999, “Imaging a Quasar Accretion Disk with Microlensing”, *Ap. J.* **524**, 49
- [2] Alard C., 1995, “First results of the DUO program”, in *Astrophysical Applications of Gravitational Lensing*, ed. by C. S. Kochanek and J. N. Hewitt, Kluwer Academic Publishers, Dordrecht, Boston, London, page 215
- [3] Albrow M. D., et al., 1999, “The Relative Lens-Source Proper Motion in MACHO 98-SMC-1”, *Ap. J.* **512**, 672
- [4] Alcock C., et al., 1993, “Possible gravitational microlensing of a star in the Large Magellanic Cloud”, *Nature* **365**, 621
- [5] Alcock C., et al., “The MACHO Project: Microlensing Results from 5.7 Years of LMC Observations”, preprint astro-ph/0001272
- [6] Andredakis Y. C., Sanders R. H., 1994, “Exponential bulges in late-type spirals: an improved description of the light distribution”, *M.N.R.A.S.* **267**, 283
- [7] Ansari R., et al., 1999, “AgapeZ1: a large amplification microlensing event or an odd variable star towards the inner bulge of M31”, *Astron. Astrophys.* **344**, L49
- [8] Aubourg E., et al., 1993, “Evidence for gravitational microlensing by dark objects in the Galactic halo”, *Nature* **365**, 623
- [9] Bahcall N., 1997, in: “Critical Dialogues in Cosmology”, ed. N. Turok, World Scientific, Singapore, page 221
- [10] Barkana R., et al., 1999, “A Reassessment of the Data and Models of the Gravitational Lens Q0957+561”, *Ap. J.* **520**, 479
- [11] Barrow J. D., Juskiwicz R., Sonoda D. H., 1985, “Universal rotation: how large can it be?”, *M.N.R.A.S.* **213**, 917
- [12] Bartelmann M., et al., 1998, “Arc statistics with realistic cluster potentials. IV. Clusters in different cosmologies”, *Astron. Astrophys.* **330**, 1

- [13] Bartelmann M., Schneider P., 1999, “Weak Gravitational Lensing”, to be submitted to *Physics Reports*, preprint: astro-ph/9912508
- [14] Bernstein G., Fischer P., Tyson J. A., Rhee G., 1997, “Improved Parameters and New Lensed Features for Q0957+561 from WFPC2 Imaging”, *Ap. J.* **483**, L79
- [15] Berry M., 1986, “Cosmology and Gravitation”, Adam Hilger, Bristol
- [16] Bertschinger E., et al., 1990, “Potential, velocity, and density fields from redshift-distance samples: Application – Cosmography within 6000 kilometers per second”, *Ap. J.* **364**, 370
- [17] Binney J., Tremaine S., 1987, “Galactic Dynamics”, Princeton University Press, Princeton
- [18] Birch P., 1982, “Is the universe rotating?”, *Nature* **298**, 451
- [19] Birch P., 1983, reply to [139], *Nature* **301**, 736
- [20] Blandford R., Narayan R., 1986, “Fermat’s principle, caustics, and the classification of gravitational lens images”, *Ap. J.* **310**, 568
- [21] Blandford R. D., 1992, “The Black-Hole Model of Active Galactic Nuclei”, in: “Physics of Active Galactic Nuclei. Proceedings of the International Conference”, eds. W. Duschl, S. J. Wagner, Springer-Verlag, Berlin
- [22] Blanton M., Turner E. L., Wambsganss J., 1998, “Ultraviolet images of the gravitationally lensed quadruple quasar Q2237+0305 with the HST WFPC2”, *M.N.R.A.S* **298**, 1223
- [23] Budó A., 1965, “Theoretische Mechanik”, VEB Deutscher Verlag der Wissenschaften, Berlin, 1965, p. 338
- [24] Burud I., et al., 1998, “Three photometric methods tested on ground-based data of Q 2237+0305”, *Astron. Astrophys.* **339**, 701
- [25] Böhringer H., 1995, “Clusters of Galaxies”, in: “Seventeenth Texas Symposium on Relativistic Astrophysics and Cosmology”, eds. H. Böhringer, G. E. Morfill, J. E. Trümper, The New York Academy of Sciences, New York, page 67
- [26] Burke W. L., 1981, “Multiple gravitational imaging by distributed masses”, *Ap. J.* **244**, L1
- [27] Brainerd T. G., Blandford R. D., Smail I., 1996, “Weak Gravitational Lensing by Galaxies”, *Ap. J.* 466, 623
- [28] Carroll S. M., Field G. B., 1997, “Is there evidence for cosmic anisotropy in the polarization of distant radio sources?”, *Phys. Rev. Lett.* **79**, 2394
- [29] Kochanek C. S., et al., 1999, “CASTLES Survey”, Internet: [cfawww.harvard.edu/castles/](http://cfawww.harvard.edu/castles/)

- [30] Chae K.-H., 1999, “New Modeling of the Lensing Galaxy and Cluster of Q0957+561: Implications for the Global Value of the Hubble Constant”, *Ap. J.* **524**, 582
- [31] Chang K., Refsdal S., 1979, “Flux variations of QSO 0957+561 A, B and image splitting by stars near the light path”, *Nature* **282**, 561
- [32] Chartas G., et al., 1999, “X-Ray Detection of the Primary Lens Galaxy Cluster of the Gravitational Lens System Q0957+561”, *Ap. J.* **504**, 661
- [33] Clowe D., et al., 1998, “Weak Lensing by Two Z approximately 0.8 Clusters of Galaxies”, *Ap. J. Lett.* **497**, 61
- [34] Colley W. N., Turner E. L., Kundić T., 2000, “Refined Apache Point Time Delay for Q0957+561A,B”, preprint
- [35] Collins C. B., Hawking S. W., 1973, “The rotation and distortion of the universe”, *M.N.R.A.S.* **162**, 307
- [36] Cristiani S., et al., 1996, “The optical variability of QSOs”, *Astron. Astrophys.* **306**, 395
- [37] Dalcanton J., et al., 1994, “Observational limits on Omega in stars, brown dwarfs, and stellar remnants from gravitational microlensing”, *Ap. J.* **424**, 550
- [38] Eddington A. S., 1919, “Joint eclipse meeting of the Royal Society and the Royal Astronomical Society”, *Observatory* **42**, 391
- [39] Corrigan R. T., et al., 1991, “Initial light curve of Q2237+0305”, *Astron. J.* **102**, 34
- [40] Crotts A. P. S., Tomaney A. B., 1996, “Results from a Survey of Gravitational Microlensing toward M31”, *Ap. J. Lett.* **473**, 87
- [41] Crotts A. P. S., 1999, talk given in July 1999 at the gravitational lensing conference in Boston, MA
- [42] de Vaucouleurs G., 1948, *Ann. d’Ap.* **11**, 247
- [43] Drabkin I. E., Drake S., 1960, “Galileo Galilei on Motion and on Mechanics”, translations with introductions and notes, University of Wisconsin Press, Madison, Wisc.
- [44] Dyer C. C., Roeder R. C., 1973, “Distance-Redshift Relations for Universes with Some Intergalactic Medium”, *Ap. J. Lett.* **180**, 31
- [45] Einasto J., Kaasik A., Saar E., 1974, “Dynamic evidence on massive coronas of galaxies”, *Nature* **250**, 309; Correction, 1974, *Nature* **250**, 790
- [46] Einstein A., 1911, “Über den Einfluß der Schwerkraft auf die Ausbreitung des Lichtes”, *Annalen der Physik* **35**, 898

- [47] Einstein A., 1915, "Erklärung der Perihelbewegung des Merkur aus der allgemeinen Relativitätstheorie", *Sitzungsber. Preuß. Akad. Wissensch., erster Halbband*, page 831
- [48] Eisenstein D., Bunn E. F., 1997, "Comment on the Appropriate Null Hypothesis for Cosmological Birefringence", *Phys. Rev. Lett.* **79**, 1997
- [49] Falco E.E., Gorenstein M.V., Shapiro I.I., 1991, "New model for the 0957 + 561 gravitational lens system - Bounds on masses of a possible black hole and dark matter and prospects for estimation of  $H_0$ ", *Ap. J.* **372**, 364
- [50] Fan X., Bahcall N. A., Cen R., 1997, "Determining the Amplitude of Mass Fluctuations in the Universe", *Ap. J. Lett.* **490**, 123
- [51] Feferman S., et al. (eds.), 1990, "Kurt Goedel Collected Works, Volume II, Publications 1938-1974", Oxford University Press, Oxford
- [52] Fischer P., Bernstein G., Rhee G., Tyson J. A., 1997, "The Mass Distribution of the Cluster 0957+561 From Gravitational Lensing", *Astron. J.* **113**, 521
- [53] Fluke C. J., Webster R. L., 1999, "Investigating the geometry of quasars with microlensing", *M.N.R.A.S.* **302**, 68
- [54] Galilei G., "De Motu", unpublished work at the University of Pisa, 1589-1592, translation in: [43], page 48
- [55] Gamov G., 1946, "Rotating Universe?", *Nature* **158**, 549
- [56] Garnavich P. W., et al., 1998, "Supernova Limits on the Cosmic Equation of State", *Ap. J.* **509**, 74
- [57] Garrett M. A., et al., 1994, "Global VLBI Observations of the Gravitational Lens System 0957+561A, B", *M.N.R.A.S.* **270**, 457
- [58] Gödel K., 1949, "An example of a new type of cosmological solutions of Einstein's field equations of gravitation", *Rev. Mod. Phys.* **21**, 447
- [59] Gödel K., 1952, "Rotating universes in general relativity theory", Proc. Intern. Cong. Math., Cambridge, Mass, 1, 175
- [60] Gorenstein M. V., et al., 1983, "Detection of a compact radio source near the center of a gravitational lens - Quasar image or galactic core", *Science* **219**, 54
- [61] Gorenstein M. V., et al., 1988, "VLBI observations of the gravitational lens system 0957+561 - Structure and relative magnification of the A and B images", *Ap. J.* **334**, 42
- [62] Gott J. R., 1981, "Are heavy halos made of low mass stars? - A gravitational lens test", *Ap. J.* **243**, 140

- [63] Griest K., 1991, “Galactic microlensing as a method of detecting massive compact halo objects”, *Ap. J.* **366**, 412
- [64] Grogin N. A., Narayan R., 1996, “A New Model of the Gravitational Lens 0957+561 and a Limit on the Hubble Constant”, *Ap. J.* **464**, 92; Erratum, 1996, *Ap. J.* **473**, 570
- [65] Haarsma D. B., Hewitt J. N., Lehár J., Burke B. F., 1999, “The Radio Wavelength Time Delay of Gravitational Lens 0957+561”, *Ap. J.* **510**, 64
- [66] Hancock S., Rocha G., Lasenby A. N., Gutierrez C. M., 1998, “Constraints on cosmological parameters from recent measurements of cosmic microwave background anisotropy”, *M.N.R.A.S.* **294**, 1
- [67] Haugan S. V. H., 1996, “The Microlensing Events In Q2237+0305A: No Case Against Small Masses/Large Sources”, in: “Astrophysical Applications of Gravitational Lensing”, ed. C. S. Kochanek & J. N. Hewitt, Kluwer (Dordrecht), page 255
- [68] Hawking S., 1969, “On the rotation of the universe”, *M.N.R.A.S.* **142**, 129
- [69] Hawking S. W., Ellis G. F. R., 1973, “The large scale structure of space-time”, Cambridge University Press, Cambridge
- [70] Hawking S. W., 1990, “Introductory note to 1949 and 1952”, in: [51], page 189
- [71] Hawkins M. R. S., 1993, “Gravitational Microlensing Quasar Variability and Missing Matter”, *Nature* **366**, 242
- [72] Hawkins M. R. S., 1997, “Dark galaxies – the dominant population?”, *Astron. Astrophys.* **328**, L25
- [73] Hawkins M. R. S., 1998, “Caustic crossing in quasar light curves?”, *Astron. Astrophys.* **340**, L23
- [74] Hewett P. C., Foltz C. B., Chaffee F. H., 1999, “The large bright quasar survey. 6: Quasar catalog and survey parameters”, *Astron. J.* **109**, 1498
- [75] Hohl F., 1971, “Numerical Experiments with a Disk of Stars”, *Ap. J.* **168**, 343
- [76] Houde M., Racine R., 1994, “Image restoration and photometric monitoring of the gravitational lens Q2237+0305”, *Astron. J.* **107**, 466
- [77] Hu W., Sugiyama N., Silk J., 1998, “The physics of microwave background anisotropies”, *Nature* **386**, 37
- [78] Huchra J., et al., 1985, “2237 + 0305 – A new and unusual gravitational lens”, *Astron. J.* **90**, 691



- [79] Hudson M. J., Gwyn S. D. J., Dahle H., Kaiser N., 1998, "Galaxy-Galaxy Lensing in the Hubble Deep Field: The Halo Tully-Fisher Relation at Intermediate Redshift", *Ap. J.* **503**, 531
- [80] Lineweaver C. H., Barbosa D., 1998, "What Can Cosmic Microwave Background Observations Already Say about Cosmological Parameters in Open and Critical-Density Cold Dark Matter Models ?", *Ap. J.* **496**, 624
- [81] Irwin M. J., et al., 1989, "Photometric variations in the Q2237+0305 system: First detection of a microlensing event", *Astron. J.* **98**, 1989
- [82] Ivanenko D. D., Korotky V. A., Obukhov Y. N., 1986, "On the Rotation of the Universe", *Astron. Circ. Acad. Sci. USSR* **1458**, 1
- [83] Ivanenko D. D., Korotky V. A., Obukhov Y. N., 1986, "The cosmological scenario of the rotating universe", *Astron. Circ. Acad. Sci. USSR* **1473**, 2
- [84] Ivanenko D. D., Korotky V. A., Obukhov Y. N., 1987, "The microwave background in the rotating and expanding universe", *Astron. Circ. Acad. Sci. USSR* **1510**, 2
- [85] Jackson N., et al., 1998, "Lensing galaxies: light or dark ?", *Astron. Astrophys.* **334**, L33
- [86] Jain B., Seljak U., 1997, "Cosmological Model Predictions for Weak Lensing: Linear and Nonlinear Regimes", *Ap. J.* **484**, 560
- [87] Jain B., Seljak U., White S., 1999, "Ray Tracing Simulations of Weak Lensing by Large-Scale Structure", preprint astro-ph/9901191
- [88] Jimenez R., Heavens A. F., Hawkins M. R. S., Padoan P., 1997, "Dark galaxies, spin bias and gravitational lenses", *M.N.R.A.S.* **292**, 5
- [89] Kaiser N., 1992, "Weak gravitational lensing of distant galaxies", *Ap. J.* **388**, 272
- [90] Kaiser N., Squires G., 1993, "Mapping the dark matter with weak gravitational lensing", *Ap. J.* **404**, 441
- [91] Kaiser N., 1995, "Nonlinear cluster lens reconstruction", *Ap. J. Lett.* **439**, 1
- [92] Kayser R., Refsdal S., Stabell R., 1986, "Astrophysical applications of gravitational microlensing", *Astron. Astrophys.* **166**, 36
- [93] Kayser R., Refsdal S., 1989, "Detectability of gravitational microlensing in the quasar QSO2237 + 0305", *Nature* **338**, 745
- [94] Kayser R., Helbig P., Schramm T., 1997, "A general and practical method for calculating cosmological distances", *Astron. Astrophys.* **318**, 680

- [95] King I. R., 1966, "The structure of star clusters. III. Some simple dynamical models", *Astron. J.* **71**, 64
- [96] Kneib J.-P., Alloin D., Pello R., 1998, "Unveiling the nature of the Cloverleaf lens-system: HST/NICMOS-2 observations", *Astron. Astrophys.* **339**, 65
- [97] Kochanek C. S., 1996, "Is There a Cosmological Constant ?", *Ap. J.* **466**, 638
- [98] Kogut A., et al., 1993, "Dipole Anisotropy in the COBE Differential Microwave Radiometers First-Year Sky Maps", *Ap. J.* **419**, 1
- [99] Korotkii V. A., Obukhov Yu. N., 1995, "Polarization of radiation in a rotating universe", *Sov. Phys. JETP* **81**, 1031
- [100] Korotky V. A., Obukhov Y. N., 1996, "On cosmic rotation", in: "Gravity, Particles and Space-Time", eds P. Pronin and G. Sardanasvily, World Scientific, Singapore, page 421, preprint: gr-qc/9604049
- [101] Kristian J., Sachs R. K., 1966, "Observations in cosmology", *Ap. J.* **143**, 379
- [102] Kristian J., 1967, "On the cosmological distortion effect", *Ap. J.* **147**, 864
- [103] Kühne R. W., 1997, "On the Cosmic Rotation Axis", *Mod. Phys. Lett.* **A12**, 2473
- [104] Kundić T., Wambsganss J., 1993, "Gravitational microlensing - The effect of random motion of individual stars in the lensing galaxy", *Ap. J.* **404**, 455
- [105] Kundić T., et al., 1997, "A Robust Determination of the Time Delay in 0957+561A, B and a Measurement of the Global Value of Hubble's Constant", *Ap. J.* **482**, 75
- [106] Kundt W., 1956, "Trägheitsbahnen in einem von Gödel angegebenen kosmologischen Modell", *Zeitschr. f. Physik* **145**, 611
- [107] Lanczos C., 1924, *Zeitschr. f. Physik* **21**, 73
- [108] Lewis G. F., Miralda-Escudé J., Richardson D. C., Wambsganss J., 1993, "Microlensing light curves - A new and efficient numerical method", *M.N.R.A.S.* **261**, 647
- [109] Lewis G.F., Irwin M.J., 1996, "The statistics of microlensing light curves. II. Temporal analysis.", *M.N.R.A.S.* **283**, 225
- [110] Lewis G. F., Irwin M. J., Hewett P. C., Foltz C. B., 1998, "Microlensing-induced spectral variability in Q 2237+0305", *M.N.R.A.S.* **295**, 573
- [111] Maitra S., 1966, *J. Math. Phys.* **7**, 1025
- [112] Mansouri R., Nozari K., 1997, "Rotation of Plane of Polarization of an Electromagnetic Wave Propagating over Cosmological Distances in "Finite Rotating Universe" Scenario", preprint: gr-qc/9710028

- [113] Mao S., Schneider P., 1998, "Evidence for substructure in lens galaxies?", *M.N.R.A.S.* **295**, 587
- [114] Maoz D., Rix. H.-W., 1993, "Early-Type Galaxies, Dark Halos, and Gravitational Lensing Statistics", *Ap. J.* **416**, 425
- [115] Mellier Y., 1999, "Probing the Universe with Weak Lensing", *Ann. Rev. Astron. Astrophys.* **37**, 127
- [116] Mineshige S., Yonehara A., 1999, "Gravitational Microlens Mapping of a Quasar Accretion Disk", *Proc. Astron. Soc. J.* **51**, 497
- [117] Misner C. W., Thorne K. S., Wheeler J. A., 1973, "Gravitation", W. H. Freeman and Company, New York, page 566
- [118] Mould J. R., et al., 1993, "The velocity field of clusters of galaxies within 100 megaparsecs. II - Northern clusters", *Ap. J.* **409**, 14
- [119] Mould J. R., et al., 2000, "The HST Key Project on the Extragalactic Distance Scale. XXVIII. Combining the Constraints on the Hubble Constant", preprint astro-ph/9909260
- [120] Narayan R., Bartelmann M., 1997, "Lectures on Gravitational Lensing", in: "Proceedings of the 1995 Jerusalem Winter School", eds. A. Dekel and J. P. Ostriker, preprint astro-ph/9606001
- [121] Nityananda R., Ostriker J. P., 1984, "Gravitational lensing by stars in a galaxy halo - Theory of combined weak and strong scattering", *J. Ap. Astr.* **5**, 235
- [122] Nodland B., Ralston J. P., 1997, "Indication of Anisotropy in Electromagnetic Propagation over Cosmological Distances", *Phys. Rev. Lett.* **78**, 3043
- [123] Obukhov Y. N., 1992, "Rotation in Cosmology", *General Relativity and Gravitation* **24**, 121
- [124] Obukhov Y. N., Korotky V. A., Hehl F. W., 1997, "On the rotation of the universe", preprint astro-ph/9705243
- [125] Østensen R., et al., 1996, "Monitoring of the Einstein Cross with the Nordic Optical Telescope", *Astron. Astrophys.* **309**, 59
- [126] Ohanian H. C., 1983, "The caustics of gravitational 'lenses'", *Ap. J.* **271**, 551
- [127] Oscoz A., et al., 1997, "Time delay of QSO 0957+561 and cosmological implications", *Ap. J.* **479**, L89
- [128] Ostriker J. P., Peebles P. J. E., 1973, "A Numerical Study of the Stability of Flattened Galaxies: or, can Cold Galaxies Survive?", *Ap. J.* **186**, 467

- [129] Ostriker J. P., Peebles P. J. E., Yahil A., 1974, "The size and mass of galaxies, and the mass of the universe", *Ap. J.* **139**, L1
- [130] Ozsváth I., Schücking E., 1962, "Finite Rotating Universe", *Nature* **193**, 1168
- [131] Paczyński B., 1986, "Gravitational microlensing at large optical depth", *Ap. J.* **301**, 503
- [132] Paczyński B., 1986, "Gravitational microlensing by the galactic halo", *Ap. J.* **304**, 1
- [133] Panov V. F., Sbytov, Yu. G., 1992, "Accounting for Birch's observed anisotropy of the universe: cosmological rotation?", *Sov. Phys. JETP* **74**, 411
- [134] Peebles P. J. E., 1993, "Principles of Physical Cosmology", Princeton University Press, Princeton
- [135] Pelt J., Schild R., Refsdal S., Stabell R., 1998, "Microlensing on different timescales in the lightcurves of QSO 0957+561 A,B", *Astron. Astrophys.* **336**, 829
- [136] Pen U.-L., et al., 1993, "A well sampled light curve for Q2237+0305", in: "Gravitational lenses in the universe", ed. J. Surdej et al., Université de Liège
- [137] Perlmutter S., et al., 1999, "Measurements of Omega and Lambda from 42 High-Redshift Supernovae", *Ap. J.* **517**, 565
- [138] Persic M., Salucci P., 1995, "Rotation Curves of 967 Spiral Galaxies", *Ap. J. Suppl.* **99**, 501
- [139] Phinney E. S., Webster R. L., 1983, "Is there evidence for universal rotation?", *Nature* **301**, 735
- [140] Press W. H., Teukolsky S. A., Vetterling W. T., Flannery B. P., 1992, "Numerical Recipes in C", Second edition, Cambridge University Press, Cambridge
- [141] Racine R., 1992, "Continuum and semiforbidden C III microlensing in Q2237 + 0305 and the quasar geometry", *Ap. J.* **395**, L65
- [142] Raffelt G., 1997, in: "The Evolution of the Universe (Dahlem Workshop)", eds. G. Börner & S. Gottlöber, Wiley, Chichester, page 23
- [143] Raine D. J., 1975, "Mach's principle in general relativity", *M.N.R.A.S.* **171**, 507
- [144] Raymond J. C., Smith B. W., 1977, "Soft X-ray spectrum of a hot plasma", *Ap. J. Suppl.* **35**, 419
- [145] Rees M. J., 1984, "Black Hole Models for Active Galactic Nuclei", *Ann. Rev. Astron. Astrophys.* **22**, 471
- [146] Refsdal S., 1964, "On the possibility of determining Hubble's parameter and the masses of galaxies from the gravitational lens effect", *M.N.R.A.S.* **128**, 307

- [147] Refsdal S., Stabell R., 1991, "Gravitational micro-lensing for large sources", *Astron. Astrophys.* **250**, 62
- [148] Refsdal S., Stabell R., 1993, "Gravitational microlensing variability caused by small masses", *Astron. Astrophys.* **278**, L5
- [149] Refsdal S., 1998, talk given at the Gravitational lensing workshop held in the Norwegian Academy of Sciences in Oslo in July 1998
- [150] Remy M., et al., 1996, "The clover leaf quasar H1413+117: New photometric light curves", in "Astrophysical Applications of Gravitational Lensing", ed. C. S. Kochanek and J. N. Hewitt, Kluwer Academic Publishers, Dordrecht, Boston, London, p261
- [151] Retzlaff J., 1999, "Das Leistungsspektrum von Galaxienhaufen und die Diskriminierung zwischen Modellen kosmologischer Strukturbildung mit dunkler Materie", PhD thesis, Universität Potsdam
- [152] Riess A. G., Press W. H., Kirshner R. P., 1996, "A Precise Distance Indicator: Type IA Supernova Multicolor Light-Curve Shapes", *Ap. J.* **473**, 88
- [153] Rix H.-W., Schneider D. P., Bahcall J. N., 1992, "Hubble Space Telescope Wide Field Camera imaging of the gravitational lens 2237 + 0305", *Astron. J.* **104**, 959
- [154] Robertson D. S., Carter W. E., Dillinger W. M., 1991, "New measurement of the solar gravitational deflection of radio signals using VLBI", *Nature* **349**, 28
- [155] Rubin V. C., Ford W. K., 1970, "Rotation of the Andromeda Nebula from a Spectroscopic Survey of Emission Regions", *Ap. J.* **159**, 379
- [156] Rubin V. C., Burstein D., Ford W. K., Thonnard N., 1985, "Rotation velocities of 16 SA galaxies and a comparison of Sa, Sb, and SC rotation properties", *Ap. J.* **289**, 81
- [157] Thompson D. J., Schild R. E., 1996, "The Q0957+561 microlensing", in *Astrophysical Applications of Gravitational Lensing*, ed. C. S. Kochanek and J. N. Hewitt, Kluwer Academic Publishers, Dordrecht, Boston, London, p267
- [158] Sachs R. K., "Gravitational waves in general relativity VI. The outgoing radiation condition", 1961, *Proc. R. Soc. A* **264**, 309
- [159] Sahu K. C., 1993, "Stars Within the Large Magellanic Cloud as Potential Lenses for Observed Microlensing Events", *Nature* **370**, 275
- [160] Salpeter E. E., 1955, "The Luminosity Function and Stellar Evolution", *Ap. J.* **121**, 161
- [161] Scalo J., 1998, "The IMF Revisited: A Case for Variations", in: "The Stellar Initial Mass Function (38th Herstmonceux Conference)", eds. G. Gilmore & D. Howell, *ASP Conference Series* **142**, 201

- [162] Schild R. E., Thomson D. J., 1995, "Twin QSO Q0957+561 Time Delay Dataset", *Astron. J.* **109**, 1970
- [163] Schild R., 1996, "Microlensing Variability of the Gravitationally Lensed Quasar Q0957+561 A,B", *Ap. J.* **464**, 125
- [164] Schild R., 1996, "Rapid Microlensing in Q0957+561", *BAAS* **189**, 2702
- [165] Schild R. E., Thomson D. J., 1997, "The Q0957+561 Time Delay From Optical Data", *Astron. J.* **113**, 130
- [166] Schmidt R. W., 1996, "The effect of the bar in the gravitational lens system 2237+0305", Master's thesis, University of Melbourne
- [167] Schmidt R., Webster R. L., Lewis G. F., "Weighing a galaxy bar in the lens Q2237+0305", *M.N.R.A.S.* **295**, 488
- [168] Schmidt R., Wambsganss J., 1998, "Limits on MACHOs from microlensing in the double quasar Q0957+561", *Astron. Astrophys.* **335**, 379
- [169] Schneider D. P., et al., 1988, "High resolution CCD imaging and derived gravitational lens models of 2237+0305", *Astron. J.* **95**, 1619; Erratum, 1988, *Astron. J.* **96**, 1755
- [170] Schneider P., Ehlers J., Falco E. E., 1991, "Gravitational Lenses", Springer Verlag, Berlin
- [171] Schneider P., 1985, "A new formulation of gravitational lens theory, time-delay, and Fermat's principle", *Astron. Astrophys.* **143**, 413
- [172] Schneider P., 1993, "Upper bounds on the cosmological density of compact objects with sub-solar masses from the variability of QSOs", *Astron. Astrophys.* 279, 1
- [173] Schneider P., Seitz C., 1994, "Steps towards nonlinear cluster inversion through gravitational distortions. 1: Basic considerations and circular clusters", *Astron. Astrophys.* **294**, 411
- [174] Schneider P., van Waerbeke L., Mellier Y., Jain B., Seitz S., Fort B., 1998, "Detection of shear due to weak lensing by large-scale structure", *Astron. Astrophys.* **333**, 767
- [175] Schramm T., Kayser R., 1987, "A simple imaging procedure for gravitational lenses", *Astron. Astrophys.* **174**, 361
- [176] Seitz S., Schneider P., Ehlers J., 1994, "Light propagation in arbitrary spacetimes and the gravitational lens approximation", *Class. Quantum Grav.* **11**, 2345
- [177] Silk J., 1999, "The Fundamental Parameters of Cosmology", *Publ. Astr. Soc. Pac.* **111**, 258
- [178] Smith S., 1936, "The mass of the Virgo cluster", *Ap. J.* **83**, 23

- [179] Smoot G. F., et al., 1992, "Structure in the COBE differential microwave radiometer first-year maps", *Ap. J. Lett.* **396**, 1
- [180] Soldner J., 1804, "Über die Ablenkung eines Lichtstrahls von seiner geradlinigen Bewegung durch die Attraktion eines Weltkörpers, an welchem er nahe vorbeigeht", *Berliner Astron. Jahrb. 1804*, page 161
- [181] Tormen G., Moscardini L., Lucchin F., Matarrese S., 1993, "The galaxy velocity field and cold dark matter models", *Ap. J.* **411**, 16
- [182] Tyson J. A., Gorenstein M. V., 1985, "Resolving the Nearest Gravitational Lens", *Sky & Telescope*, **70**, 319
- [183] Tyson J. A., Wenk R. A., Valdes F., 1990, "Detection of systematic gravitational lens galaxy image alignments - Mapping dark matter in galaxy clusters", *Ap. J. Lett.* **349**, 1
- [184] Turner M. S., 1999, "Cosmology Solved? Quite Possibly!", *Publ. Astr. Soc. Pac.* **111**, 264
- [185] Udalski A., et al., 1992, "The Optical Gravitational Lensing Experiment", *Acta Astron.* **42**, 253
- [186] Valdes F., Tyson J. A., Jarvis J. F., 1983, "Alignment of faint galaxy images: Cosmological distortion and rotation", *Ap. J.* **271**, 431
- [187] Vanderriest C., et al., 1989, "The value of the time delay  $\Delta t(A, B)$  for the 'double' quasar 0957+561 from optical photometric monitoring", *Astron. Astrophys.* **215**, 1
- [188] Vietri M., Ostriker J. P., 1983, "The statistics of gravitational lenses - Apparent changes in the luminosity function of distant sources due to passage of light through a single galaxy", *Ap. J.* **267**, 488
- [189] Walsh D., Carswell R. F., Weymann R. J., 1979, "0957+561 A,B: twin quasistellar objects or gravitational lens?", *Nature* **279**, 381
- [190] Wambsganss J., 1990, "Gravitational Microlensing", PhD thesis, Munich University, available as MPA report 550
- [191] Wambsganss J., Cen R., Ostriker J. P., 1995, "Testing cosmogonic models with gravitational lensing", *Science* **268**, 274
- [192] Wambsganss J., Kundić T., 1995, "Gravitational Microlensing by Random Motion of Stars: Analysis of Light Curves", *Ap. J.* **450**, 19
- [193] Wambsganss J., Paczyński B., 1991, "Expected color variations of the gravitationally microlensed QSO 2237 + 0305", *Astron. J.* **102**, 864
- [194] Wambsganss J., Paczyński B., Schneider P., 1990, "Interpretation of the microlensing event in QSO 2237 + 0305", *Ap. J.* **358**, L33

- [195] Wambsganss J., 1992, “Gravitational microlensing - The effect of a single lens and the impact of sparse sampling”, *Ap. J.* **392**, 424
- [196] Wambsganss J., Brunner H., Schindler S., Falco E., 1999, “The gravitationally lensed quasar Q2237+0305 in X-rays: ROSAT/HRI detection of the “Einstein Cross”, *Astron. Astrophys.* **346**, L5
- [197] Webster R. L., 1985, “Gravitational lensing and galaxy shape”, *M.N.R.A.S.* **213**, 871
- [198] Webster R. L., Ferguson M. N., Corrigan R. T., Irwin M. J., 1991, “Interpreting the light curve of Q2237+0305”, *Astron. J.* **102**, 1939
- [199] Weinberg S., 1972, “Gravitation and cosmology: Principles and applications of the general theory of relativity”, John Wiley & Sons, New York
- [200] Westphal J., 1992, “PC imaging of gravitational lenses, WFPC GTO augmentation, cycle 2”, HST proposal ID 3799
- [201] Westphal J., 1995, “Galactic nuclei, galactic bulges, local group, dust lanes, globular clusters, surface photometry”, HST proposal ID 5236
- [202] Williams R. E., et al., 1996, “The Hubble Deep Field: Observations, Data Reduction, and Galaxy Photometry”, *Astron. J.* **112**, 1335
- [203] Wilson G., talk given in July 1999 at the gravitational lensing conference in Boston, MA
- [204] Wilson G., Kaiser N., Luppino G. A., 2000, in preparation
- [205] Witt H. J., 1991, “Der Mikrogravitationslinseneffekt – Theorie und Anwendungen”, PhD thesis, Universität Hamburg
- [206] Witt H. J., 1993, “An efficient method to compute microlensed light curves for point sources”, *Ap. J.* **403**, 530
- [207] Witt H. J., Mao S., 1994, “Interpretation of microlensing events in Q2237 + 0305”, *Ap. J.* **429**, 66
- [208] Wolfram S., et al., 1998, Mathematica 3.0, internet: [www.mathematica.com](http://www.mathematica.com)
- [209] Wozniak P. R., et al., “The Optical Gravitational Lensing Experiment. Monitoring of QSO 2237+0305”, preprint astro-ph/9904329, the most recent light curve can be looked at at [www.astro.princeton.edu/~ogle/ogle2/huchra.html](http://www.astro.princeton.edu/~ogle/ogle2/huchra.html)
- [210] Wu X.-P., 1994, “Gravitational microlensing by the MACHOs of the Large Magellanic Cloud”, *Astron. J.* **435**, 66
- [211] Wyithe J. S. B., Webster R. L., 1999, “Application of the contouring method to extended microlensed sources”, *M.N.R.A.S.* **306**, 223



- [212] Wyithe J. S. B., Webster R. L., Turner E. L., 1999, “A measurement of the transverse velocity of Q2237+0305”, *M.N.R.A.S.* 309, 261
- [213] Wyithe J. S. B., Webster R. L., Turner E. L., 2000, “The distribution of microlensed light curve derivatives: the relationship between stellar proper motions and transverse velocity”, submitted to *M.N.R.A.S.*, preprint, astro-ph/9901339
- [214] Wyithe J. S. B., Webster R. L., Turner E. L., 2000, “Limits on the microlens mass function of Q2237+0305”, accepted by *M.N.R.A.S.*, preprint, astro-ph/9904359
- [215] Wyithe J. S. B., Webster R. L., Turner E. L., Mortlock D. J., 2000, “A gravitational microlensing determination of continuum source size in Q2237+0305”, accepted by *M.N.R.A.S.*, preprint, astro-ph/9904361
- [216] Wyithe J. S. B., Webster R. L., Turner E. L., 2000, “The rate of caustic crossing microlensing events for Q2237+0305”, submitted to *M.N.R.A.S.*, preprint, astro-ph/9908120
- [217] Wyithe J. S. B., Webster R. L., Turner E. L., 2000, “A small source in Q2237+0305?”, submitted to *M.N.R.A.S.*, preprint, astro-ph/9911245
- [218] Wyithe J. S. B., Turner E. L., Webster R. L., Agol E., 2000, “Predicting caustic crossing high magnification events in Q2237+0305”, submitted to *M.N.R.A.S.*, preprint, astro-ph/0001306
- [219] Wyithe J. S. B., Turner E. L., Webster R. L., 2000, “Interpretation of the OGLE Q2237+0305 microlensing light-curve”, submitted to *M.N.R.A.S.*, preprint, astro-ph/9911245
- [220] Yee H. K. C., 1988, “High-resolution imaging of the gravitational lens system candidate 2237+030”, *Astron. J.* 95, 1331
- [221] Yonehara A., et al., 1998, “An X-Ray Microlensing Test of AU-Scale Accretion Disk Structure in Q2237+0305”, *Ap. J.* **501**, 41; Erratum, 1999, *Ap. J.* **511**, 65
- [222] Yonehara A., 1999, “Source Size Limitation from Variabilities of a Lensed Quasar”, *Ap. J. Lett.* **519**, 31
- [223] Yonehara A., et al., 1999, “Microlens diagnostics of accretion disks in active galactic nuclei”, *Astron. Astrophys.* **343**, 41
- [224] Zwicky F., 1933, “Die Rotverschiebung von extragalaktischen Nebeln”, *Helv. Phys. Acta* **6**, 110

# List of Figures

1.1	Rotation curves of four galaxies . . . . .	4
2.1	Wavefront propagation in a galaxy potential. . . . .	7
2.2	HST <i>I</i> -band image of Q0957+561 . . . . .	8
2.3	HST <i>V</i> -band image of Q2237+0305 . . . . .	11
2.4	Diagram of a gravitational lens system . . . . .	13
2.5	Critical line and caustics . . . . .	19
3.1	Single star microlensing light curve . . . . .	22
3.2	Mass profile for the 0957+561 lensing galaxy . . . . .	26
3.3	Q0957+561 <i>g</i> -band light curve & difference light curve 1995 to 1997 . . . . .	28
3.4	Magnification patterns and light curves for different MACHO masses . . . . .	31
3.5	Probability distribution for microlensing variations . . . . .	37
3.6	MACHO mass exclusion probabilities . . . . .	40
4.1	HST close-up of the central region of Q2237+0305 . . . . .	43
4.2	Image of the central region of the lensing galaxy 2237+0305. . . . .	45
4.3	Image of the lensing galaxy 2237+0305 . . . . .	49
4.4	Magnitude difference $m_3 - m_2$ between reference stars 3 and 2 . . . . .	51
4.5	Transmission at Apache Point Observatory 1995-1997 . . . . .	52
4.6	Image of the two quasar images A and B of Q2237+0305 . . . . .	54
4.7	Q2237+0305 light curve . . . . .	57
5.1	Affine parameter-redshift relation in a rotating universe . . . . .	72
5.2	Shear $\gamma$ as a function of redshift $z$ . . . . .	75
5.3	Shear values for background sources at three azimuthal angles $\phi$ . . . . .	77
5.4	Shear values for background sources for three universal expansion parameters $b$ . . . . .	78

# List of Tables

3.1	Exclusion probabilities for MACHO masses, 100% mass fraction, part I . . . . .	36
3.1	Exclusion probabilities for MACHO masses, 100% mass fraction, part II . . . . .	37
3.2	Exclusion probabilities for MACHO masses, 50% mass fraction . . . . .	38
3.3	Exclusion probabilities for MACHO masses, 25% mass fraction . . . . .	39
4.1	Observation log: Q2237+0305 at APO, part I . . . . .	46
4.1	Observation log: Q2237+0305 at APO, part II . . . . .	47
4.1	Observation log: Q2237+0305 at APO, part III . . . . .	48

# Danksagung/Acknowledgements

Zuerst einen ganz lieben Dank an meine Elke, dafür daß sie da ist. Vielen Dank an Mama, Papa, Gerald, Julia und Tony für die Unterstützung und die vielen Telefonate. Bärchen und Uwe ein großes Dankeschön für die Zeit in Trebitz während der Fertigstellung dieser Arbeit.

Ich möchte mich ganz herzlich bei Joachim Wambsganß für die persönliche Betreuung während der letzten dreieinhalb Jahre am AIP und an der Universität Potsdam bedanken.

Für interessante Diskussionen um die Relativitätstheorie und rotierende Universen möchte ich Volker Müller und Prof. Liebscher danken. Volker Perlick danke ich sehr für die prompten und hilfreichen Tips zur Gödel-type Metrik. Elena Schilbach, Ralf Scholz und Sonja Hirte danke ich für die Hinweise zur Astrometrie im Einstein Kreuz. Ue-Li Pen danke ich für die vielen Diskussionen zur Datenreduktion der APO Daten und den sehr schönen Forschungsaufenthalt in Toronto. Peter Schneider danke ich für Diskussionen zu weak lensing, cosmic shear und Lichtausbreitung in allgemeinen Raumzeiten, sowie seine Gastfreundschaft während meines Aufenthaltes am MPA im März 1999.

Während meiner Zeit am AIP sorgten Sepehr Arbabi-Bidgoli, Cendriya, Mark McCaughrean, Stefan Gottlöber, Tilo Jankowski, Alexander Knebe, Rainer Köhler & Friedrich, Jan Mückel, Jörg Retzlaff, Thomas Stanke (schon im HH212 Office mit Bergblick, dem ich doch immer etwas hinterhertrauerte!), Jesper Storm und Zardoz für eine angenehme Arbeitsatmosphäre im Container. It was great fun to discuss weak lensing observations and much more with David Woods during late-night Krumme Lanke drives and his whole time at the AIP.

It is a pleasure to thank Ed Turner and Tomislav Kundić for providing the Apache Point Observatory monitoring data on Q2237+0305. Ed Turner is also thanked for providing the latest, still unpublished Q0957+561 data [34], for the difference light curve analysis. Vyatcheslav Shalyapin is thanked for letting me know about the other observations at the NOT and at Maidanak observatory of the Q2237+0305 brightness peak in 1996. The work described in Chapter 4 has emerged from a collaboration with Ue-Li Pen that began at the 1998 Astroparticle physics research institute in the Center for Physics in Aspen, CO., and was continued during a stay in Toronto in February 1999 and at the 1999 meeting of the Astroparticle physics research institute in Ringberg, Germany. Support for all travels and both research institutes by the German-American Academic Council is gratefully acknowledged. I thank all observers who observed at Apache Point Observatoy between 1995 and 1997 for the Q2237+0305 monitoring program: T. Kundic, W. N. Colley, S. Malhotra, U. Pen, J. E. Rhoads, K. Z. Stanek, E. L. Turner, J. Wambs-

ganss, L. E. Bergeron, K. A. Gloria, D. C. Long, C. Corson, and C. Hastings.

Meine Stelle am AIP wurde von der Deutschen Forschungsgemeinschaft unter Gz. WA 1047/2-1 finanziert. An der Universität Potsdam wurde ich noch vier weitere Monate aus Mitteln der Professur Astrophysik (Joachim Wambsganß) bezahlt. Der Studienstiftung des deutschen Volkes danke ich sehr herzlich für die finanzielle Unterstützung für den Flug zur Texas in Chicago Konferenz im Dezember 1996.